UNIVERSITÄT PADERBORN

Die Universität der Informationsgesellschaft

Synthesis and characterization of stimuli-degradable polymeric nanoparticles

Dissertation

Submitted to the Department of Chemistry at Paderborn University for the degree of

Doctor rerum naturalium

(Dr. rer. nat.)

By Matthias van der Linde, M. Sc.

Born on June 8th, 1991 in Bocholt

Abstract

In contemporary therapeutic approaches, addressing the dual challenge of maximizing drug efficacy while minimizing side effects for patients remains a primary focus. To tackle this issue, a promising strategy involves the encapsulation of drugs within a degradable polymeric matrix, enabling release at a specific site of action. Particularly noteworthy are light-responsive polymers, known for their ability to achieve tailored on-demand drug release when exposed to light, offering a remarkable spatiotemporal control over the drug release. This study explores the field of photodegradable drug delivery systems based on polyurethane and polyketals with a focus on the particle properties during and after exposure to light. As a result, a particulate system was developed that can be synthesized in a simple, two-step protocol and whose hydrolytic degradation is initiated by irradiation with light. The light-responsive polymers show successful degradation upon exposure to light, as evidenced by SEC and UV-VIS spectroscopy. Particles were formulated from the polymers by nanoprecipitation and characterized by DLS and the degradation behavior was demonstrated and characterized by DLS and NMR experiments.

Zusammenfassung

Die moderne Medizin steht der Herausforderung gegenüber, die therapeutische Effektivität von Wirkstoffen zu maximieren und gleichzeitig die Nebenwirkungen für Patienten zu minimieren. Eine vielversprechende Strategie zur Bewältigung dieser Aufgabe ist der Einschluss von Wirkstoffen in eine abbaubare Polymermatrix, die eine gezielte Freisetzung an einem bestimmten Wirkort ermöglicht. Von besonderem Interesse sind hierbei licht-responsive Polymere, mit denen bei Lichteinwirkung eine Wirkstofffreisetzung erreicht werden kann, da sie eine hohe räumliche und zeitliche Kontrolle über die Wirkstofffreisetzung ermöglichen. In dieser Forschungsarbeit werden Licht-responsive *Drug Delivery Systeme* auf Basis von Polyurethanen und Polyketalen untersucht, wobei der Schwerpunkt auf den Eigenschaften der Partikel während und nach der Lichteinwirkung liegt. Eines der Ergebnisse ist die Entwickelung eines Partikelsystems, welches in einem simplen, zweistufigen Syntheseprozess hergestellt werden kann und dessen hydrolytischer Abbau durch Bestrahlung mit Licht eingeleitet werden kann. Alle vorgestellten Licht-responsiven Polymere zeigen einen erfolgreichen Abbau bei Lichteinwirkung, wie durch GPC-Experimente und UV-VIS-Spektroskopie nachgewiesen werden konnte. Aus den Polymeren wurden durch Nanopräzipitation Partikel formuliert und durch DLS charakterisiert und das Abbauverhalten durch DLS und NMR-Experimente nachgewiesen und charakterisiert.

Table of Contents

1 Introduction

1.1 Motivation

The conventional admission of drugs is often limited by drug stability, solubility, and bioavailability. Systemic delivery may also result in off-target effects, which raises the need for greater doses and the possibility of negative reactions. Researchers have used nanotechnology to create novel drug delivery systems (DDS) that provide fine control over medication release and targeting in an effort to overcome these obstacles. Particles of sizes in the nanometer range, usually about 100 nanometers, are known as nanoparticles and have attracted a lot of attention as potential drug delivery systems. They are suitable for encasing, shielding, and delivering a variety of therapeutic agents, such as proteins, nucleic acids, and small molecules, because of their small size, huge surface area, and customizable characteristics. This recently became apparent in the development of novel COVID-19 mRNA vaccines, which rely on lipid nanoparticles to protect their chemical unstable payload.[1]

The cancer mortality rate continuously declined since 1991, resulting in an overall drop of 33 % and approximately 3.8 million cancer deaths averted. This steady development can be partly contributed to changes in lifestyle and increase of medical checkups but is also in large due to the advancement of medical treatment.[2] These new treatment methods include targeted drug delivery, which has become a vital keystone of modern medicine. Drug delivery systems carry a drug that is covalently bound or trapped in a matrix and released over extended time durations or at specific times or sites of action. They were developed to overcome obstacles in conventional treatment like poor drug biodistribution and selectivity, in vivo breakdown of the drug and the reduce side effects.[3,4] More recent progress is being made in the field of research into smart drug delivery systems. They are chemically pre-programmed to release their payload in response to an external or internal trigger and provide unprecedented control over the drug release.[5] Potential stimuli to trigger the drug release are the pH value, temperature, redox potential, enzymes, light irradiation, ultrasound, and high frequent magnetic fields or combinations of several.[6,7] Of particular interest for this work are the stimuli light and pH value. Drug release triggered by irradiation with light has the highest spatiotemporal control over its application. By adjusting parameters such as time, wavelength and intensity the molecular structure of the delivery system can be manipulated very selectively. The most widely used, best researched and synthetically most easily accessible functional group for the implementation of light-responsiveness is the *ortho*-nitrobenzyl (oNB) group.[8] pH-sensitive drug delivery systems are of interest because the hypoxic microenvironment of carcinogenic tissue leads to drastically reduced pH values, which in turn lead to the release of active substances in the diseased tissue.[9,10] Especially polyketals recently

attracted more attention due to their fast degradation kinetics and biocompatible degradation products.[11] Although much progress has been made in recent years, there are still challenges such as protein absorption, stealth, biodistribution, cellular uptake, incomplete or non-selective release, excretion of degradation products, toxicity and the development of new synthesis platforms and triggering groups.

1.2 Scope and goal

The aim of this work is to study stimuli-responsive drug delivery systems (DDS) with a focus on light and pH as a trigger. Degradation products should be hydrophilic and oligomeric, or in best case small molecules, to allow for easy renal clearance. The influence of hydrophilicity on the degradation of the particles should be investigated and possibilities to control the hydrophilicity and degradation behavior should be considered. Therefore, polyurethanes with different hydrophilic building blocks should be synthesized and characterized. Nanoparticles are to be formulated from them and the influence of the increased hydrophilicity on the degradation should be studied. Furthermore, polyketals with light-responsive tunable hydrophilicity should be synthesized and their degradation behavior after single irradiation event should be investigated. Size exclusion chromatography (SEC), nuclear magnetic resonance (NMR) spectroscopy and UV-VIS spectroscopy will be used to characterize the polymers and their degradation behavior. Nanoparticles will be formulated, and their degradation behavior will be studied using dynamic light scattering (DLS) and NMR spectroscopy.

2 Theoretical background

2.1 Step-growth polymerization

Reactions of monomers that result in the formation of long chains are called polymerizations.[12] Different polymerization techniques can be categorized into chain-growth polymerizations and step-growth polymerizations as fundamental distinct mechanisms.[13]

Chain-growth polymerizations have in common that the mechanism is divided into three steps: the initiation, the propagation, and the termination. During the initiation, reactive centers such as radicals or ions, are formed. Followed by the propagation phase, where e.g. one alkyne containing monomer is added to a growing chain each iteration. The termination step terminates the reactive center and ends the reaction. The chains do not remain active after the termination step. As in Figure 2.1 was visualized, one of the characteristics of chain-growth polymerizations is the rapid increase of the average molecular weight (M_n) at low conversions, which flattens out at longer reaction times and higher conversions.[14]
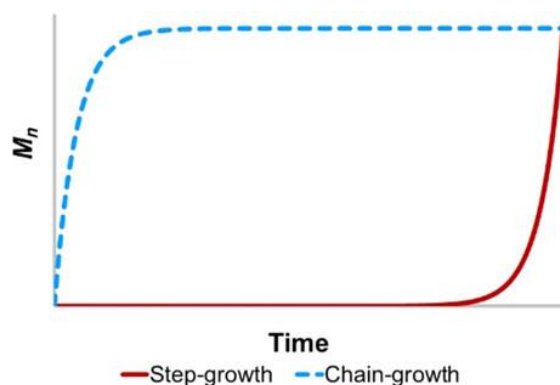
Figure 2.1 Schematic polymer growth kinetic profiles for conventional chain-growth (blue) and step-growth (red) polymerization mechanism.[15]

Contrary to that, the step-growth polymerization has only a low increase of the molecular weight (M_n) during the initial phase of the reaction and only at high conversions, a strong increase of the molecular weight is observed. The reason for this is the underlying reaction mechanism. As shown in Figure 2.2 bifunctional monomers first form dimers and trimers, later oligomers and only at very high conversions long chains are formed and high molecular weight are reached. Since the end-group functionality remains intact after each elongation step, the final polymer is also end-group functionalized.[13,14]
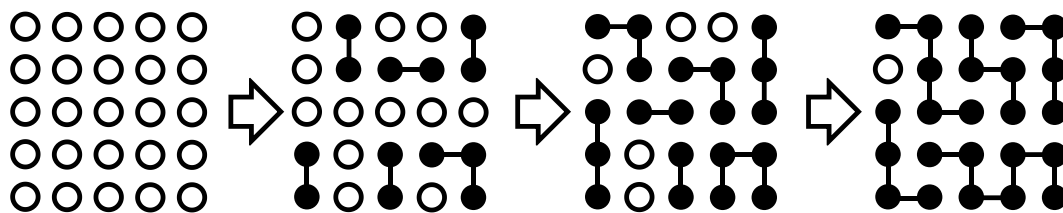
Figure 2.2 Diagram of a step growth reaction with different conversion
rates. Long chains only form at very high conversions.[13]

Step-growth polymerizations require monomers with chemical functions that can form covalent bonds with each other. These functionalities can both be within the same molecule, such as in γ-hydroxybutyric acid, which reacts to polyester *via* a condensation reaction. Such monomers are referred to as an AB monomer, where A and B represent the reactive groups. Accordingly, monomers containing two of the same functional groups are referred to AA or A_2 and BB/B_2 type monomers.[14] A special characteristic of the linear AA/BB systems is the high dependency of the molar weight on the molar radio of the educts. It is necessary to adjust the stoichiometry precisely if high molecular weights are to be achieved. (Figure 2.2) The number-average degree of polymerization (P_n) can be expressed by the CAROTHERS equation, shown in Figure 2.3, which expresses die dependency of the degree of polymerization (P_n) on the conversion rate p and the molar ratio r.[14,16]

CAROTHERS equation:

$$P_n = \frac{r + 1}{r - 2rp + 1}$$
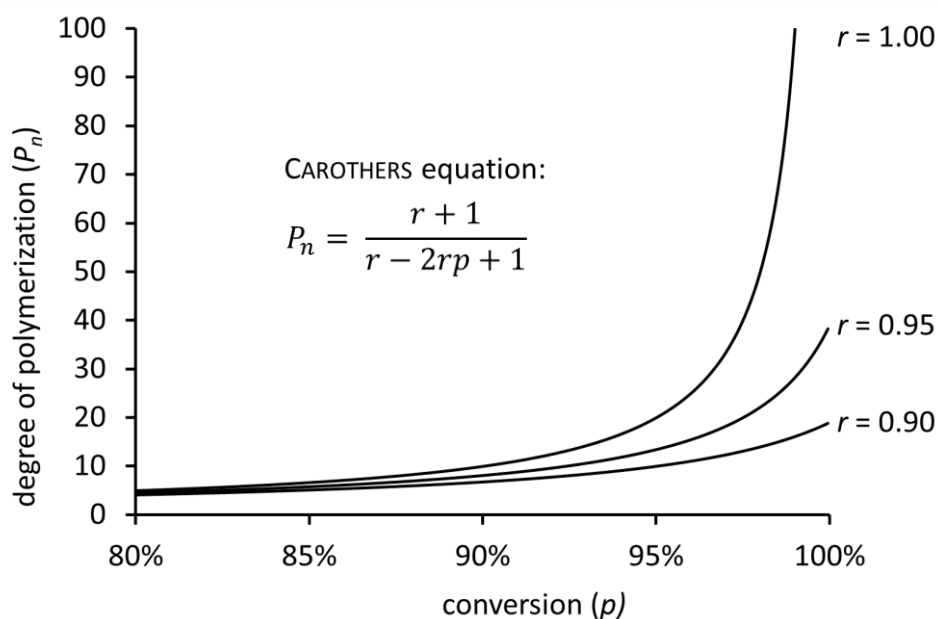
Figure 2.3 Number average degree of polymerization (P_n) in dependence of the conversion rate and the molar ratio r expressed by the CAROTHERS equation. [14,16]

Bifunctional monomers lead to the formation of only linear polymers, whereas higher functional molecules do not follow the CAROTHERS stoichiometry and introduce tree-like structures and eventually surpass the gel point to form cross-linked networks.[17,18] The reaction mechanism of the elongation steps can either be an addition or a condensation reaction, hence the distinction between polyaddition[19] and polycondensations.[20]

$$n\ A\ +\ n\ B\ \longrightarrow\ \left[AB\right]_n$$
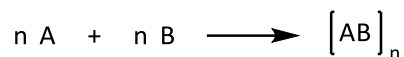
Scheme 2.1 General reaction equation of a polyaddition.

Polyaddition is a fundamental polymerization process that plays a pivotal role in the synthesis of a wide range of polymers with diverse applications in our daily lives. Polyadditions are characterized by their ability to yield polymers with precise chemical structures and do not form side products or small molecules during the synthesis. Typical nucleophilic functional groups of monomers are alcohols and amines, the most prominent electrophilic functional groups for polyadditions are isocyanates and epoxides. Examples for polymers formed by these monomers are poly urea, epoxy resin and polyurethanes (PUR). The latter is the commercially most important one and is used in a variety of everyday applications such as adhesives, coatings, sealings, synthetic fiber, shoe soles, solid foams, paddings.

In industrial-scale production, polyester- or polyether diols are predominantly used, sometimes with addition of small-molecule polyols. However, polyurethanes can be formed from any diol or polyol. As a second component isocyanates, mainly diisocyanates, are used. Despite their large-scale use and economic relevance, the range of commercially available diisocyanates is very limited. Some examples are displayed in Scheme 2.2. Diisocyanates can be categorized into two main groups: aromatic isocyanates (e.g. MDI, TDI), and aliphatic isocyanates (e.g. IPDI, HDI, H12MDI). Aromatic isocyanates hold greater significance in terms of quantity due to the higher reactivity of aromatically bonded isocyanate groups and their economic accessibility. However, products utilizing aromatic isocyanates tend to yellow when exposed to light. Aliphatic isocyanates are employed when specific property requirements, such as lightfastness in coatings and finishes, necessitate their use as they can only be achieved with aliphatic isocyanates.
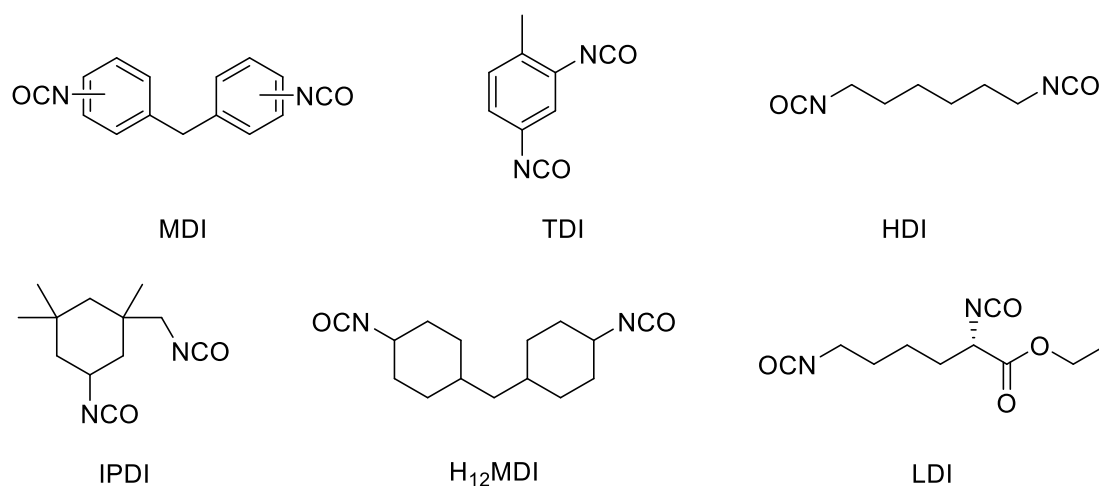
Scheme 2.2 Commercially available diisocyanates used on a large scale in polyurethane chemistry.

The biodegradation of polyurethanes is not studied in detail but is believed to be due to the action of esterase, urethanase, hydrolases and protease enzymes.[21] Due to their size, enzyme activity is limited to the surface and therefore very slow. The degradation of urethane and urea linkages produces free amine and hydroxyl groups.[22] polyurethanes are known for their excellent blood- and biocompatibility. Therefore, they play a major role in the development of medical devices such as catheters, artificial hearts and other implants, tissue engineering as well as drug delivery.[23,24] However, *in vitro* degradation of petrochemical, polymerized diisocyanates, such as MDI or HDI, can release toxic diamines. In the recent decade a new lysin-based diisocyanate has gained growing attention. Fully degraded, *L*-lysine ethylester diisocyanate (LDI) forms the highly biocompatible amino acid lysine and is therefore evaluated in plenty medical applications.[25–28]

Most polyurethane formations are carried out using organic bases like triethylamine or 1,2-diazabicyclo [2.2.2] octane (DABCO) or organometallic compounds like dibutyltin dilaurate (DBTL) as a catalyst.[29] Especially DBTL is widely applied because of the high acceleration of the carbamate formation. The reason for this is the formation of complexes with both, hydroxy species, and the isocyanate function.[30,31] Amine based catalysts are known to accelerate the reaction of isocyanates with water.[32]
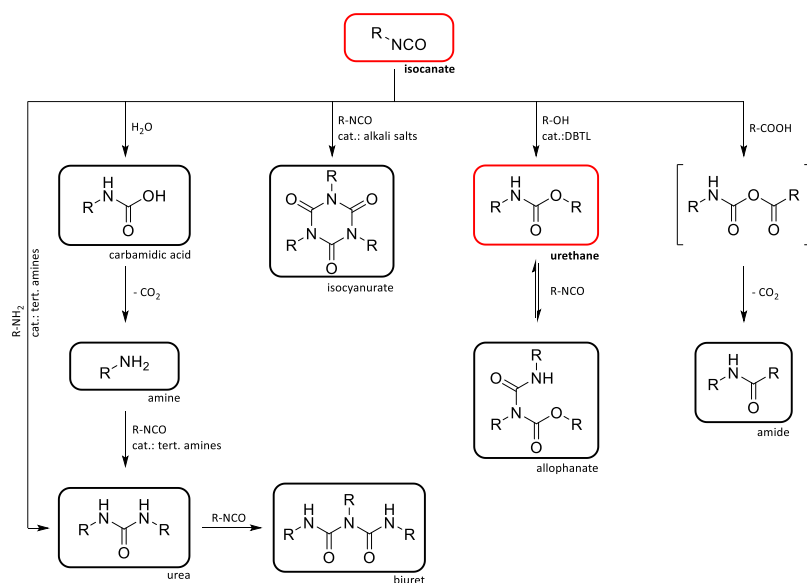
Scheme 2.3 Reaction scheme of isocyanate to various products
that occur within the scope of polyurethane chemistry.

Isocyanates are a very versatile functional group and can undergo a variety of reactions in addition to the widely used formation of polyurethanes. A set of reactions, that commonly occur in the realm of polyurethane chemistry is shown in Scheme 2.3. These include, for example, the phospholine oxide-catalyzed formation of carbodiimides, the phosphine-catalyzed formation of uretdiones or the addition with epoxide to form oxazolidone. Of greater synthetic relevance for polyurethane chemistry, however, is the formation of isocyanurates in the presence of alkali salts, the formation of allophanates from the reaction of isocyanates and urethanes at high temperatures or the formation of urea as an adduct of amines and isocyanates. Also, amides can be formed by the reaction of isocyanates with carboxylic acids. On the one hand, this shows the high versatility of the isocyanate based polyurethane chemistry but shows on the other hand how important it is to choose the correct reaction conditions, substrates and reagents.

$$n\,A \quad + \quad n\,B \quad \rightleftharpoons \quad \left[AB\right]_n \quad + \quad n\,C$$

Scheme 2.4 General reaction equation of a polycondensation.

Polycondensation reactions also underly the mechanism of the step-growth polymerization and therefore share a lot of similarities with polyaddition reactions, however, they also differ in some crucial aspects. Polycondensations are characterized by the formation of small molecules as side products at each chain elongation iteration (Scheme 2.4). These small molecules, such as H_2O, MeOH, CO_2 or HCl, can sometimes be volatile and leave the reaction, be separated by vacuum or scavengers, or can remain in the reaction mixture. Typical reaction mechanisms are transesterifications or -amidations to form polyesters or polyamides or the more complex reaction between formaldehyde and Phenol to form phenoplasts. Characteristics of polycondensations are the possibility to catalyze their mechanism with

Brønsted-acids and the development of equilibriums. Therefore, conversion rates are also governed by the Le Chatelier principle. To achieve high molecular weights, high conversions are required, as has been shown earlier in Figure 2.1. To reach high conversions according to the Carothers-equation, it may be necessary to remove the lower molecular weight side product from the equilibrium. However, this highly depends on the specific synthesis. The polyesterification of pentanediol and adipic acid for example has an equilibrium constant of K = 6.0, making the removal of water out of the equilibrium necessary to reach high molecular weights. The polyesterification of bisphenol A and the chloroformiate derivative of bisphenol A has an equilibrium constant of $K = 4.7 \times 10^3$, reaching high conversions without the removal of side product.[14,33]

2.2 Drug delivery systems

A dosage that is applied to patients for pharmaceutical treatments of diseases consists of the drug itself, also called the active pharmaceutical ingredient (API) and excipients that give the formulation a particulate structure and shape. These excipients allow convenient and accurate dosing, mask a bitter tase or bulk up very potent APIs. They can also take critical functional roles like increasing the stability or influence the absorption and distribution of the API in the body.[34] This technique of delivering medication to a patient in such a manner that specifically increases the drug concentration in some parts of the body is called drug delivery.[35] In a broader sense, drug delivery systems (DDS) also includes techniques and devices such as nasal sprayers or inhalers or microfabricated devices and chambers to release drugs.[36] However, in recent decades the development in the field of drug delivery has undergone a remarkable transformation with the introduction of nano carrier-based drug delivery systems. These nano carriers usually have a size of about 100 nm and have a broad variety of different architectures like micelles, nanoparticles, liposomes, or mesoporous silica particles. They all have in common, that drug molecules like peptides, proteins or small molecules are entrapped and released at a later time.[37] However, for the sake of clarity, this introduction focuses only on organic based drug delivery systems. Numerous compelling advantages arise from the application of nanotechnology in drug delivery, such as precise cell targeting, enhanced drug potency and reduced toxicity.[38,39]

The first colloidal drugs appeared when interdisciplinary research in the 1960s and 1970s led to the development of liposomes,[40] polymer-drug conjugates[41] and dendrimers.[42] The functionalization of poly(lactide-*co*-glycolide) (PLGA) NP surfaces with polyethylene glycol (PEG) prevented non-specific binding to blood components and reduced their clearance *in vivo* by cells of the mononuclear phagocytic system (MPS), leading to prolonged blood circulation times.[43,44] This modification also became known as 'stealth' nanoparticles and was

successfully applied in Doxil®, the first FDA-approved nano-drug in 1995.[45] However, in recent years the observation of anti-PEG antibodies has risen concerns about future perspectives of PEG as a stealthing agent[46] and caused a search for possible alternatives.[47] The efficacy of Doxil® was also based on another therapeutic effect, already described by Matsumura and Maeda in 1987.[48] They unveiled the mechanism of the tumoritropic accumulation of drug-polymer conjugates. This form of passive targeting later also became known as the enhanced permeability and retention (EPR) effect.[49–51]
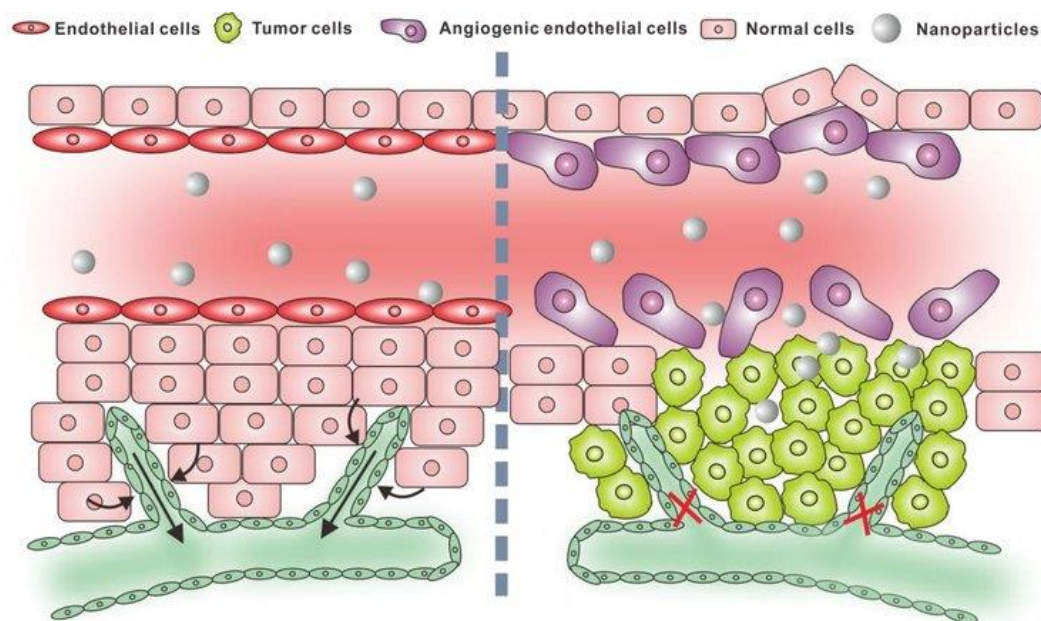
Figure 2.4 Schematic representation of healthy tissue (left) and abnormal tissue development in proximity of tumors (right). Reprinted with permission from ref. [52] © 2019 Bentham Science.

Figure 2.4 shows the altered morphology of tissue in the proximity of tumor cells compared to healthy tissue. Solid tumors that exceed the size of 2 mm begin to form blood vessels (angiogenesis) to cover the increasing demand for oxygen and nutrients.[53] These new blood vessels are very different in architecture from that of normal tissues.[54] They are irregular in shape, leaky or defective and the angiogenic endothelial cells are poorly aligned or disorganized. Also, permeability inhibiting tissue like perivascular cells and basement membrane, or smooth muscle layers can be absent or abnormal in the vessel wall or tumors. Additionally, tumor tissue has poor lymphatic drainage.[48,51,55,56] These pathological cell abnormalities cause considerably increased leakage of blood plasma components, macromolecules or nanoparticles into the cell and also decrease the removal of such components from the tumor tissue. This imbalance can be exploited to enhance drug delivery towards the affected tissue.

The use of nanosized drug carriers has the potential of increasing the concentration of the chemotherapeutic agent within a tumor by about 10 to 100 times compared to the administration of free drugs.[50,57]

Complementary to this passive targeting, early attempts of surface modification led to the introduction of active targeting in drug delivery. As early as 1980, the first nanoparticles with antibodies attached to their surface became known.[58,59] Following this, bioconjugation of affinity ligands, such as antibody fragments, peptides, aptamers, sugars and small molecules to the surface of nanoparticles, that recognize specific receptors or biomarkers on target cells enabled precise drug delivery to disease sites while sparing healthy.[38,60–62] For example apolipoprotein-modified lipid nanoparticles are able to cross the blood-brain barrier, a semipermeable border of endothelial cells that protects the brain and is known to be difficult to overcome by many drugs.[63,64] Occasionally such highly functional drug delivery systems are referred to as smart drug delivery systems.[36] The field of nanomedicine research has widened towards smart drug delivery systems to obtain more precise control of the release by implementation of stimuli responsive functionalities.[65,66] Arguably the first stimuli responsive DDS was published in 1980 with the introduction of pH sensitive liposomes.[67] Since then the field of stimuli responsive DDS has spawned dozens of different concepts and approaches for smart release of the cargo. In general, two main approaches are used to control the release of a drug, by exogeneous stimuli, that require an external applied stimulus such as light, ultrasound, temperature, magnetic or electric fields and endogenous stimuli responsive DDS on the other hand utilize unique biological microenvironments such as pH-, redox- (glutathione (GSH) or reactive oxygen species (ROS)) and enzyme concentration variations in the tissue.[5,66,68,69]

The most prominent field of application for nanoparticle-based drug delivery systems is cancer therapy. Chemotherapy is usually the first treatment of cancer patients to shrink tumor size before removing it surgically. Also, chemotherapy can control metastasis and restrict the growth of diffused tumor masses. However, regression of tumor is difficult to achieve due to dose limiting systemic toxicities and physiological barriers to deliver drugs to the tumor site. The before described EPR effect can be exploited, making cancer treatment the ideal field of application for nanoparticle-based drug delivery.[70] The progress in research is reflected in the cancer statistics of developed countries. In the US the cancer mortality rate has decreased by 33 % since 1991. This steady progress is partially due to reductions in smoking, more frequent screening for breast, colorectal and prostate cancer but also due to adjuvant chemotherapies. The recent advances in the development of targeted treatment and immunotherapy have caused huge progress especially in the mortality rate of lung cancer, leukemia, melanoma, and kidney cancer.[2] Nevertheless, up to this day cancer remains the second largest cause of death, responsible for roughly one in six death globally, still leaving much room for improvement and

progress.[71] Drug delivery systems have also been applied in many therapeutic applications outside the field of cancer therapy, for example in the treatment of inflammation and infectious diseases but also neurological or cardiovascular disorders.[72–78]

Despite decades of research, only a few drug delivery systems have been approved for application to date. Moreover, those that have been approved are not very sophisticated.[79,80] Examples for approved lipid-based drug delivery systems are phosphatidylcholine lipids like HSPC, DOPC and DOPE or PEG conjugates like DSPE-PEG.[45,81–85] The polymeric drug delivery systems, that have been approved can be categorized into nanoparticle suspensions, which are based on PLGA, proteins, ortho esters or nanocrystals, and into microsphere injections for sustained release, which predominantly are based on PLGA.[86–91] It becomes apparent, that those synthetic platforms, that have clinic success, have low molecular complexity, and rely on well-known technology, that has been around for many decades. ZHONG *et al.* published a comprehensive map of FDA approved drug delivery systems, showing that novel nanoparticle-based DDS scored worst in the ratio of clinical trials relative to the publications worldwide and very low in the ratio of marketed products relative to clinical trials. Despite their great attention in academic research and literature, only the fewest had success in medical application. Conventional DDS were numerically more promising because of their lower technology barrier.[83,92] Examples for DDSs that are currently in clinical trials are nano carriers with active targeting such as the liposome based C225-ILS-DOX[93] and SGT-94[94], the protein based nano drug AR-160[95] or CALAA01[96], the first polymer based material to enter clinical trials with siRNA for cancer therapy.[97]

Part of the absent success could be the long admission procedure and high entry barriers for new molecular entities in pharmaceutical applications. As pointed out in Figure 2.5, only one in 10 000 drugs pass the high standards of quality, efficacy and safety laid down by legislation and makes it from basic research to market readiness. Furthermore, the whole process from initial research and development through all phases of clinical trials, takes about 10 to 15 years.[98] Comparable merits can be observed for the approval procedure of DDS.[97]
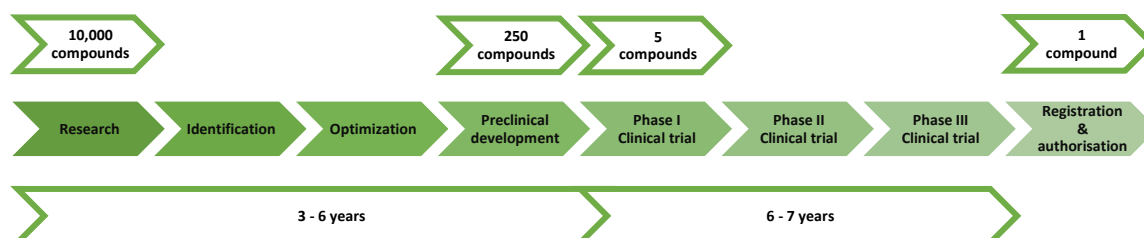

Figure 2.5 Phases, relative amount of potential candidates and required time during the typical research and development process of a drug that meets the standards of quality, efficacy and safety laid down by legislation.[98,99]

Advanced DDSs are complex in nature, with multiple components and heterogenous structures. The more complex a system is, the more components can affect the pharmacological behavior of the API and thus complex systems face more obstacles and are more likely to prone to error.[100] Especially endogenous triggers are difficult to control because of the vast variation between patients or instability of the material. Although exogenous stimuli responsive systems are easier to be controlled, major improvements would be required to solve problems related to normal tissue damage and tissue-penetration depth.[101] Also, the sophisticated structures and formulations for smart DDSs are difficult to scale up for industrial productions and therefore unattractive for the product development of pharmaceutical corporations.[102] However, it should be noted, that goals of researchers and pharmaceutical product development usually differ. The main driving force for researchers is curiosity and the knowledge generated can offer a deeper understanding about underlying principles and mechanisms.[103,104] From simple liposomal vehicles to multifunctional, stimuli responsive nanomaterials, that are at the frontier of current academic research, the development of drug delivery systems has come a long way. In search for ways to cure the world´s diseases, the interest and need for progress in this field of research continues to grow despite the decades of research that have already been done.[105]

2.3 Stimuli degradable polymeric nanoparticles

The field of smart nanoparticle-based drug delivery systems comprises a wide variety of drug release mechanisms and different particle architectures. Examples include liposomes, which are ruptured by gas expansion within their lumen, and mesoporous silica nanoparticles (MSN) that have gatekeepers obstructing their pores.[66] However, the work presented here addresses only stimuli-degradable linear polymer-based nanoparticles. As such, this chapter will only introduce this particular class of NPs and exclude liposomes, nanogels, inorganic nanoparticles, and micelles. Solid polymer nanoparticles can be synthesized by emulsion or microemulsion polymerization. The catalyst, stabilizer, and residual initiator, however, may still be present in a particle and could pose a safety risk when applied for medical use. For biomedical applications, precipitation and coacervation techniques are therefore more frequently employed. In these procedures, the dissolved polymer coacervates (usually by neutralization of complexation with electrolytes) or precipitates (usually by addition of a non-solvent) to form solid polymeric nanoparticles.[106]

Polymeric nanoparticles have historically been employed in applications addressing prolonged drug release.[107] The release of a biodegradable polymer can persist for more than a month while it hydrolyses or undergoes enzymatic degradation.[108] Use of stimuli-responsive groups can result in noticeably faster payload release. Such stimuli can either be targeted from

outside (exogenous) or exploit the chemical properties of the pathogenic microenvironment (endogenous). Exogenous stimuli degradable functional groups require some external source of energy to be applied and transferred into the inner tissue. Potential energy sources for this task are light (UV and NIR), ultrasound and locally induced hyperthermia.[109–114] However, penetration depth is an issue these methods may have to face. As laid out in Chapter 2.2, pathological tissue often has unique chemical conditions. Because of their fast cell proliferation, poor blood perfusion and altered cellular metabolism, tumors lack oxygen supply and have hypoxic conditions.[9,10] As a result, lower pH values, increased ROS- and GSH-concentrations prevail there. Similar outcomes can also be observed in inflamed tissue, where high levels of oxidative stress are also prevalent.[115–117] These conditions can be utilized for cleavage of covalent bonds to cause nanoparticle break down and drug release. Similarly, several enzymes, including hydrolases, proteases and oxidoreductases are overexpressed in tumors.[118,119] All of these unique properties are endogenous stimuli that have been used to induce the release of therapeutic agents form DDSs. [5,66,120–122] The underlying mechanism often originates from protective group chemistry. For instance, photodegradable polymeric nanoparticles are based on the photo redox chemistry of *ortho*-nitrobenzyl groups, which are the most common photocleavable group in organic synthesis. [123–125] Similarly, cyclic ortho esters have a long record of being protecting groups for diols and triols before they got introduced into drug delivery systems.[123,126,127]

Architectural wise there are three different mechanisms of stimuli degradable polymers, which are illustrated in Figure 2.6. The backbone degradable polymers (a), the end-capped self-immolative polymers (SIPs, b) and side-chain SIPs (c).[128,129] SIPs are polymers, which destroy their own molecular structure by intermolecular reactions. Known mechanisms are for example depolymerizing elimination-rearomatization reactions, cyclization reactions or elimination of the polyketals poly(methylglyoxylate).[130–133] The spontaneous depolymerization of SIPs is prevented by protecting groups which are the stimuli-responsive unit to trigger the degradation of the polymer. There is relatively little literature about end-capped SIPs (b) or head-to-tail degradable SIPs. This might be due to their demanding synthesis and sensitivity to spontaneous depolymerization.[133–135] Although being thermodynamically favorable, depolymerization might take hours to days, depending on factors such as the nature of the triggering moiety and the degree of polymerization. Furthermore, since the polymer backbone is predetermined by the required degradation mechanism, the polymer and its physical and toxicological properties cannot be modified, and the degradation kinetics can only be modified very limited.
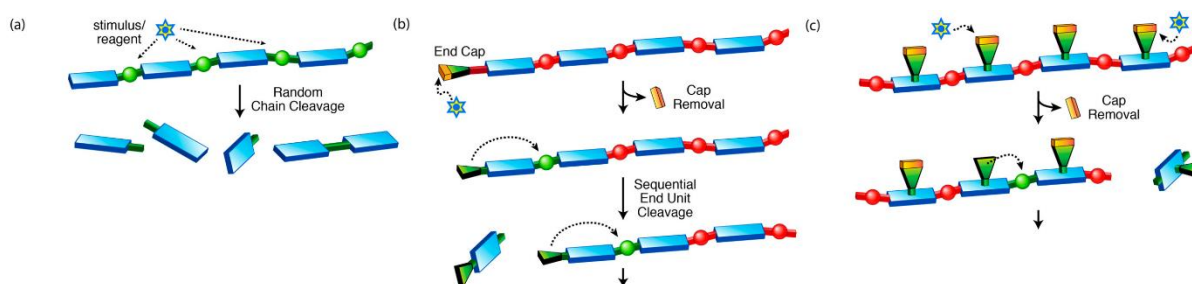
Figure 2.6 Schematic representation of polymer degradation mechanisms: (a) backbone cleavage of polymer chain, (b) end capped self-immolative polymer (SIP) and (c) sidechain self-immolative polymer (SIP). Red dots are stable under current conditions, whereas green linkages are labile. Adapted with permission from ref. [136] © 2019 American Chemical Society.

A more versatile variation of SIPs are the chain-shattering SIPs or sidechain degradable polymers, where the trigger unit protects a group in the sidechain, that causes depolymerization upon liberation. This mechanism was applied by elimination-rearomatization and by intramolecular nucleophilic attack (backbone biting).[110,137,138] Since these mechanisms can be applied in different synthetic platforms, their structural variety is larger and compatibility with living organisms can be optimized.[128] Most degradable polymers are classified as backbone-degradable polymers and have functional groups along their main chain that cleave independently *via* chemical or photochemical reaction, in which case the degradation rate remains relatively constant until the trigger or cleavable functionality is consumed.[136,139,140]

2.4 pH responsive polymeric diketals as pH responsive drug delivery systems

Cancer cells have an altered metabolism, where even under sufficient oxygen supply their main source of energy is the conversion of glucose to lactate, that typically occurs under hypoxic conditions. Since this metabolic path is less efficient, glucose consumption can be increased by 10- to 15-fold. This phenomenon, also known as the WARBURG effect, is one of the hallmarks of cancer metabolism that implies excessive production of protons, which if stayed inside the cells would result in fatal intracellular acidosis. The cells solve this problem by increasing mechanisms of proton transportation which expel excess acidity. This allows cancer cells to keep a relatively normal intracellular pH value. The expelled excess protons accumulate in the ECM, where chronic hypoxia and relative lack of blood vessels impede adequate proton clearance, thus creating an acidic microenvironment. This microenvironment is quite heterogeneous due to the tumor's metabolic heterogeneity and variable degrees of hypoxia inside the tumor mass.[141–143] The pH in the tumor ECM can be as low as 6.8.[144–146] In endosomes it can drop further to $6.0 - 6.5$, in late endosomes down to $5.0 - 5.5$ and in lysosomes the pH value can drop down to $4.5 - 5.0$.[66,147] These tumor specific pH

abnormalities can be exploited in stimuli responsive drug delivery systems, which rely on incorporation of pH sensitive functional groups into their molecular structure.
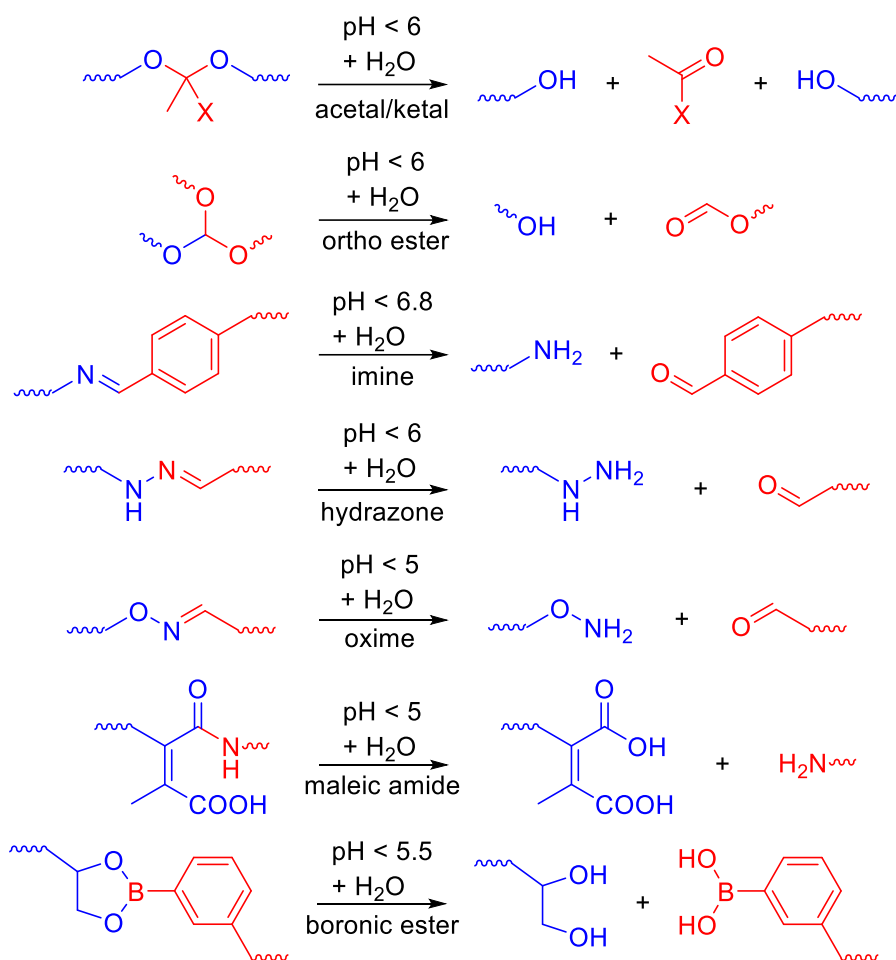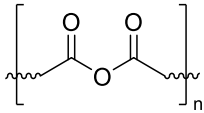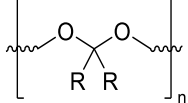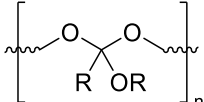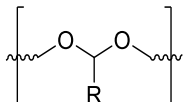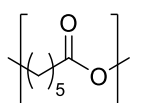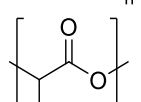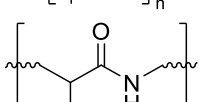
Scheme 2.5 Overview of selected hydrolysable functional groups and their approximated cleavage conditions, which have been used as stimuli responsive moieties in pH degradable polymers.

Many different pH sensitive functional groups have been implemented as the cleavable site of action into the backbone of polymers to form pH degradable polymers, some of whom are shown in Scheme 2.5. The polymers developed in this area include among others acetals (ketal)[148,149], ortho esters, imines, hydrazones, oximes, maleic amides and phenyl boronic esters.

The hydrolysis rates of the functional groups rely on multiple external factors like pH value and temperature but are even more dependent on the chemical characteristics of the functional groups and the properties of the polymeric backbone. Table 2.1 gives an overview of some classes of degradable polymers based on literature data. Of course, these data are susceptible to significant fluctuations based on the chemical variability within a polymer class.[150] However, the values can provide a good idea of the magnitude of the variations in the erosion properties among the various polymer classes. The erosion rates shown here indicate that poly(anhydrides) erode the fastest, followed by poly(ketals) and poly(ortho esters), which erode at almost the same rate.[151]

Table 2.1 Hydrolysable polymers and the hydrolysis-rates of the degradation at pH 7.4 and 25 °C.[151,152]

structure	polymer	hydrolysis rate λ (s^{-1})
	Poly(anhydrides)	1.9×10^{-3}
	Poly(ketal)	6.4×10^{-5}
	Poly(ortho esters)	4.8×10^{-5}
	Poly(acetal)	2.7×10^{-8}
	Poly(ester) ε-caproclactone	9.7×10^{-8}
	Poly(ester) PLA	6.6×10^{-9}
	Poly(amides)	2.6×10^{-13}

Especially polyorthoesters received a lot of attention as a degradable polymer for drug delivery during the last decade. [127,153,154] However, as a degradation product they form carboxylic acids which themselves can accelerate polymer breakdown and cause an autocatalytic degradation.[155–157] In addition, the triggering of inflammation is associated with acidic degradation products of biodegradable polymers.[158] Therefore polyketals are of great interest as acid-sensitive drug delivery since they form non acidic degradation products with low toxicity.[159] Among the huge variety of ketal groups, dimethyl ketals exhibit the fastest hydrolysis kinetics.[160] There are numerous studies on the usage of polyketal polymers alone, in blends, or as co-polymers for various applications available.

The first dimethyl ketal polymer for pH-sensitive drug delivery was published by HEFFERNAN and MURTHY in 2005.[159] They synthesized poly(1,4-phenyleneacetone dimethylene ketal) (PPADK) by a polycondensation reaction of benzene dimethanol and dimethoxypropane. The acid sensitive polymer was isolated with a molecular weight of M_w = 4 000 g/mol and could be used to formulate nanoparticles. The hydrolysis kinetics were evaluated by incubation of milled polymer powder in buffered solution and quantification *via* ^{1}H NMR spectroscopy. Figure 2.7 shows the synthesis and degradation (left) and degradation kinetics (right) of PPADK particles

at three different pH values. The determined threefold increase of the decay half-live time of the polymer particles from pH 7.4 to pH 5.0 was significantly less than the 250-fold increase of degradation time for water-soluble ketals. It was hypothesized that the lower pH sensitivity of PPADK is due to its water insolubility, which limits the diffusion of water and creates another rate-limiting step that is pH-independent.
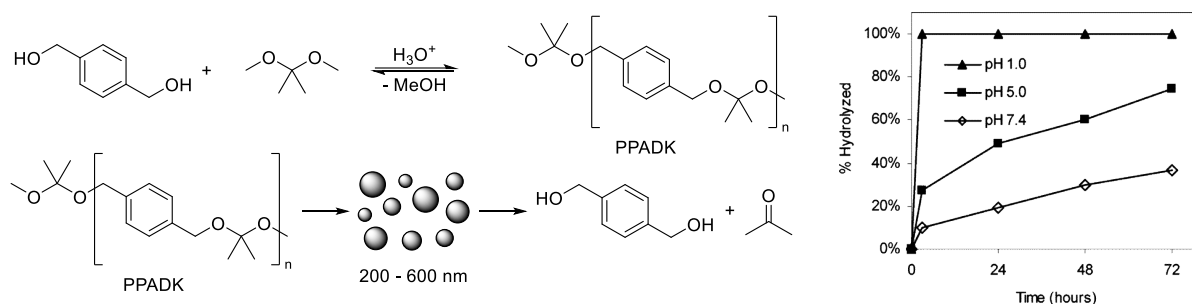
Figure 2.7 Synthesis of the polyketals PPADK *via* the acetal exchange reaction, formulation of nanoparticles and degradation in acetic environment (left). Degradation kinetics of PPADK nanoparticles at different pH values (right). Adapted with permission from ref. [159] © 2005 American Chemical Society.

The PPADK polymer was assumed to be potentially more hazardous than its aliphatic counterparts due to its aromatic structure.[161,162] Therefore a derivative of PPADK based on cyclohexane dimethanol, which is listed on the 'FDA – generally recognized as safe' (GRAS) list, was synthesized using the same acetal exchange reaction and published under the name poly(cyclohexane-1,4-diyl acetone dimethylene ketal) (PCADK). The polymer could be synthesized on a multi gram scale in a one-step synthesis with a molecular weight of M_w = 6 300 g/mol. The degradation kinetics were determined by incubation of ground microparticles in buffered solution and quantification *via* ^{1}H NMR spectroscopy. As shown in Figure 2.8 the hydrolysis rate was dependent on the pH value of the buffer, but compared to PPADK particles, it drastically increased. The half-life time at pH 4.5 was 24 d and at pH 7.4 it was calculated to be 4 years.[163]
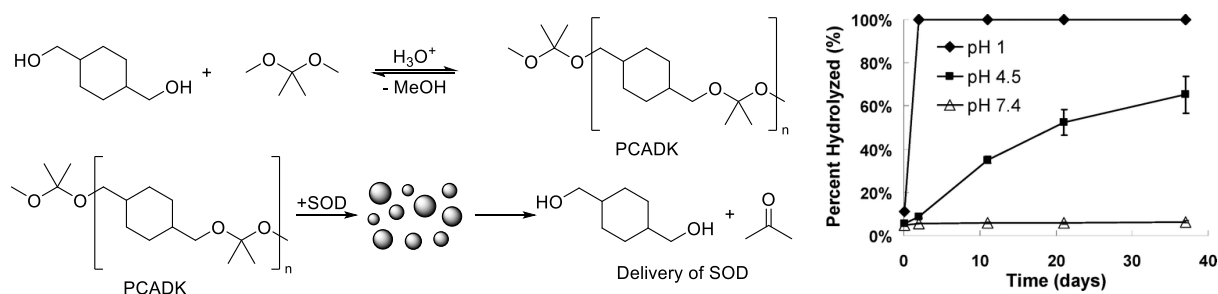
Figure 2.8 Synthesis of the polyketal PCADK *via* the acetal exchange reaction, formulation of nanoparticles and degradation in acetic environment (left). Degradation kinetics of PCADK nanoparticles at different pH values (right). Adapted with permission from ref. 162 © 2007 American Chemical Society.

Despite its extremely slow degradation rate, the application of PCADK particles for sustained release was evaluated in several use cases. The therapy of cardiac dysfunction following acute myocardial infarction with PADK bases DDS resulted in improved cardiac functions and

reduced fibrosis when tested on rats.[164] PCADK particles could be loaded with superoxide dismutase (SOD) by a double emulsion procedure and the formulation was tested as a therapeutic intervention for cardiac injury. Compared to treatment with free SOD, a superior repair capability was exhibited.[165] *In vitro* and *in vivo* studies of the treatment of acute myeloid leukemia (AML) with PCADK supported delivery of cytarabine offered a more effective alternative to treatment with the free drug.[166] In another study, PCADK nanoparticles were co-encapsulated with miR124, an inhibitor of arthritis development, and the anti-inflammatory medication ketoprofen. In an arthritic model, the nanoparticles demonstrated increased effectiveness, indicating that the PCADK system improves drug release at the target region.[167] Two more approaches for treatment of induced rheumatoid arthritis in rats with hyaluronic acid coated PCADK particles and with nanoparticles that consist of a PLGA, PCADK and PEG-*b*-PLGA blend were published.[168,169] Also, microspheres with a PLGA/PCADK blend were used to deliver Bevacizumab which is an anti-vascular endothelial growth factor for the treatment of age-associated macular degeneration. The anti-angiogenic properties were tested using chorioallantoic membrane (CAM) assay with fertilized chicken eggs and were tested in rabbit eyes. Again, the use of PCADK particles improved the therapeutic efficiency and complements the promising therapeutic prospects of PCADK as a potential nanomedicine.[170]

Since the erosion rate of PCADK is very low, a series of dimethyl ketals with varying aliphatic diols as comonomers were synthesized by YANG, MURTHY *et al.* With this series of derivates, they accelerated the hydrolysis kinetics by increasing their hydrophilic/hydrophobic balance. Six polyketals have been synthesized (PK 1 – PK 6) by copolymerization of cyclohexane dimethanol with butanediol, varying concentrations of pentanediol, hexanediol and octane diol with similar weight average molecular weights ranging from 2 200 to 2 600 g/mol. The hydrophobicity of the used diols differs from that of cyclohexane dimethanol (log P = 1.46). PK 1, PK 2 and PK 3 were copolymers synthesized with varying concentrations of pentanediol, which has a log P value of 0.27 and is therefore significantly more polar than cyclohexane dimethanol. With increasing amount of pentanediol, the hydrolysis kinetics have also increased, showing that a higher polarity of the polymerized diols translates into an increase in hydrolysis kinetics. The derivates PK 4, PK 5 and PK 6 had comparable comonomer contents to PK 3, but were synthesized with butanediol, hexanediol and octanediol as comonomers. Table 2.2 demonstrates how each has a lower polarity (log P) value than the previous one and at the same time the half-life time at pH 4.5 as well as at pH 7.4 increases. This demonstrates that the hydrolysis kinetics of polyketals can be tuned by varying their hydrophilicity and supports the hypothesis that diffusion of water into the polyketals is the rate determining step governing their hydrolysis. PK 3 was chosen as the most promising

contestant because of its fast hydrolysis kinetics and the better biocompatibility of pentanediol compared to butanediol.[11]

Table 2.2 Composition and degradation half-life time of polyketal copolymers and log *P* values of the copolymerized diol B. Shorter chain length and higher content of diol B cause shorter half-life times.[11]

n = 2: PK4
n = 3: PK3
n = 4: PK5
n = 6: PK6
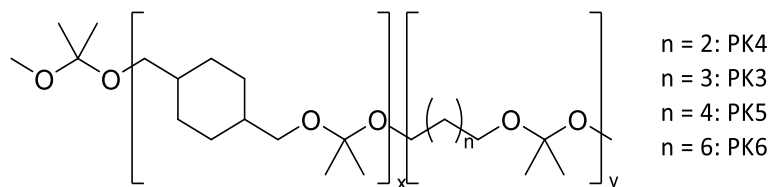
| polymer ID | polymer composition | | half-life | | log *P* of diol B |
	monomer diol B	y	pH 4.5	pH 7.4	
PK 4	1,4-butanediol	3.2 %	1.0 d	54 d	-0.83
PK 3	1,5-pentanediol	13.3 %	1.8 d	39 d	0.27
PK 5	1,6-hexandiol	14.7 %	4.4 d	53 d	0.76
PK 6	1,8-octanediol	12.7 %	18.6 d	360 d	1.75

Nanoparticles of PK3 were formed and were estimated to be suitable for treating acute inflammatory diseases because of their rapid hydrolyzation in the phagolysosomes of macrophages. The therapeutic efficacy of imatinib loaded PK3 microparticles was investigated in mice using a Concavalin A model of acute liver failure.[11]

The pharmaceutical potential of PK 3 has been investigated in several applications both *in vitro* and *in vivo* in several applications. SOD loaded PK 3 NPs ingested as an aerosol and inhibited the extent of lung fibrosis.[171] In another application for pulmonary drug delivery, Magnolol exhibited superior tissue repairing capability in a rat model of lipopolysaccharide induced lung inflammation. This drug is well-known as a potential anti-inflammatory agent but has limited clinical utility due to its poor solubility.[172] In two further studies, PK 3 bases NPs were tested as delivery systems to treat rheumatoid arthritis *in vitro* and *in vivo* using a rat arthritis model. All cases demonstrated the increased efficacy comparted to a treatment with the free drug and the high biocompatibility.[173,174] NADPH oxidase (NOX2) is a marker, that is significantly increased in myocardial infarction. In two cases a RNA based strategy for treating oxidative stress-induced myocardial infarction PK 3 based drug delivery systems showed promising results to overcome premature degradation of the RNA.[175–177]

Based on the development of PPADK, PCADK and PK 3 further functionalization of the polymer has been done. Amphiphilic copolymers have been established by attaching PEG to terminal hydroxy groups of polyketals *via* urethane or ester groups.[178,179] By addition of monohydric alcohols to the reaction mixture a reliable method of end group functionalization was established. Dialkyne terminated polyketals were functionalized with hydrophilic PNVP and

PEG chains to form amphiphilic ABA triblock copolymers. Doxorubicin loaded NPs of these were formed and showed enhanced efficacy for the treatment of murine lymphoma.[180,181]

The acetal exchange polymerization is a convenient method to form polyketals in large quantities. However, because distilling off methanol to shift the equilibrium towards high conversions is required and the characteristics of the CAROTHERS equation of high molecular weights at high conversions, molecular weight of the resulting polymer is limited to about 5 000 – 6 000 g/mol. GUO et al. developed a LEWIS acid catalyzed polyaddition reaction diols and diisopropenyl ether to dimethyl ketals that also allowed incorporation of steric demanding substrates such as drug molecules into the polymeric backbone. By this method high molecular weights of 45 – 193 kDa have been achieved.[182] In other approaches dimethyl ketal containing monomers were synthesized and then polymerized into degradable polymers of higher mass. For example, ELLING et al. developed an alternating ring-opening metathesis polymerization (AROMP) of 1,1-disubstituted cyclopropenes and dioxepines and achieved molecular weights of about 20 – 30 kDa. These approaches bear a lot of potential, however, they have high demands in purity of the reagents and reaction conditions, and the reaction is hard to scale up. Diamino-, dihydroxy- and dialyne-monomers of dimethyl ketal have been used in polyadditions to form pH degradable polymers.[183–187] In a very interesting approach ZHONG et al. added the drug Gemcitabine via two dimethyl ketal linkages into the backbone of a monomer and formed a polymer by a poly-MICHAEL-addition.[186] The here discussed concepts, as well as further examples and a more comprehensive overview of the applications in vitro and in vivo, were recently reviewed by RAJAGOPAL et al.[188]

The cleavage of polymeric bonds in hydrolytically cleavable polymeric nanoparticles is the most crucial factor that governs the drug release profile.[189] The degradation kinetics are primarily dependent on the rate of chemical cleavages in the backbone of the polymer. Some representative examples were already presented in Table 2.1. But further, the degradation kinetics get influenced by several other factors including: molecular weight, hydrophobicity, polymer glass transition temperature (T_g), surface charge and polymer crystallinity.[5,190] The effect of glass transition temperature is closely related to the polymer crystallinity. It dictates if a polymer is in its "glasslike" or "rubberlike" state and can be determined using a differential scanning calorimeter (DSC).[191] If the polymer is below the T_g, it will be in a glassy state, meaning its mobility is restricted and its diffusion rates are low. Water and drug molecules cannot move through the matrix easily. The rubbery state can be reached by rising the temperature above T_g. Water and drug molecules can move through the matrix, hydrolytic degradation and drug release rates will be increased.[192,193] However, it must be noted that in nanosized systems water can act as a plasticizing agent and lower the glass transition temperature of NPs compared to the macroscopic properties.[194]

Another factor that influences several physical properties such as crystallinity, viscosity and glass transition temperature is the molecular weight. Because it affects further factors, it also has a profound influence on the degradation rate of degradable particles. Polymers with a lower molecular weight degrade faster than their higher molecular weight counterparts.[195–198] The influence of the hydrophilic/hydrophobic balance on degradation rates could already be observed in the previous mentioned examples. As shown in Table 2.2 the hydrolysis rate of polyketals PK 3 – PK 6 was adjusted over a wide range just by interchanging the polymerized diols from butanediol to octandiol.[11] And the erosion rate of poly(ε-caprolactone) and PLA particles shown in Table 2.1 differs by an order of magnitude, although both polymers are polyesters, because poly(caprolactone) is way less polar.[151] A more profound studied example is the comparison of PLGA particles with different lactide to glycolide (L:G) ratios. The extra methyl group in the side chain of lactide groups makes PLGA with high ratios of lactide more hydrophobic. In addition to the lower flexibility of the polymer chains, higher hydrophobicity is the main reason for the lowered permeability of water into the polymeric matrix and the resulting slower degradation of polymer and decreased release rates. Figure 2.9 shows release rates from PLGA NPs with a L:G ratio of 50:50 (fastest hydrolyzation) up to 85:25 (slowest hydrolyzation).[199,200]
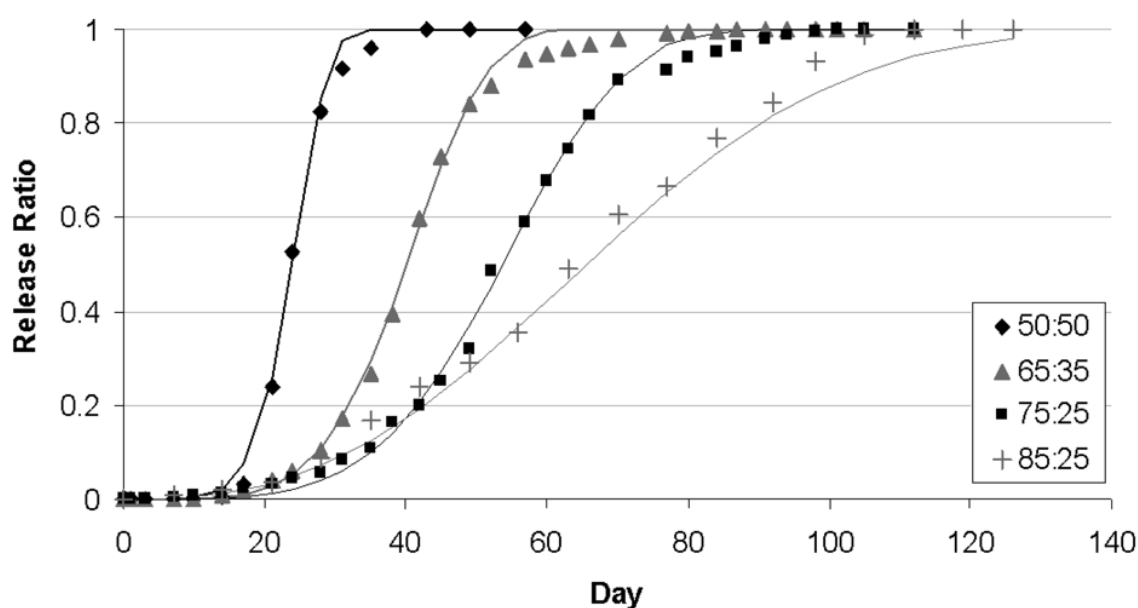
Figure 2.9 Modeled *in vivo* release profiles for PLGA copolymers with varying lactid:glycolide (L:G) radios. The profiles show a correlation between release rate and glycolide content. Reprinted with permission from ref. [199] © 2011 MDPI.

Applied to polyketals PARAMONOV *et al.* studied the degradation behavior of a set of ketal containing polyurethanes and polyureas and observed a clear and direct link between the estimated hydrophobicity of the polymer and the degradation speed of the respective particle.[149] The complex interplay of these factors should already be taken into account when developing a DDS and represents possibilities for manipulation of the desired properties.

Compared to well established systems, polyketals are a relatively new platform for drug delivery systems. They have some distinctive and promising properties: They are fast and fully acid degradable in mildly acidic environments and have good biocompatibility due to their pH neutral degradation products. In several cases their efficacy could be shown but their clinical feasibility is yet to be proven. It can be expected that further studies on the application of polyketals-based DDS in different cases could help to learn more about the properties and range of applications.

2.5 Light-responsive polymers

Light is a popular stimulus for degradable polymeric drug delivery systems because of its cleanliness, efficiency, and ability to manipulate in a spatiotemporal manner by the precise control of location, intensity and irradiation time. Light can induce covalent changes, such as isomerization, rearrangements or bond cleavage of photo-responsive groups which causes a change in polymers physicochemical properties and eventually induces drug release from light-responsive DDS.[201–203] As many stimuli-responsive functional groups, photodegradable polymers also have their origins in protecting group chemistry. Since their introduction in 1962, several light-cleavable protecting groups have been developed and incorporated into photodegradable polymers and nanoparticles, some of whom are shown in Scheme 2.6 such as coumaryl, phenacyl and benzyl-based groups like pyrene, as well as diazonaphtoquinone and spiropyran.[204–206] However, by far the most prominent and widespread used functional groups for photo-uncaging are *ortho*-nitrobenzyl (oNB) groups.[207,208]
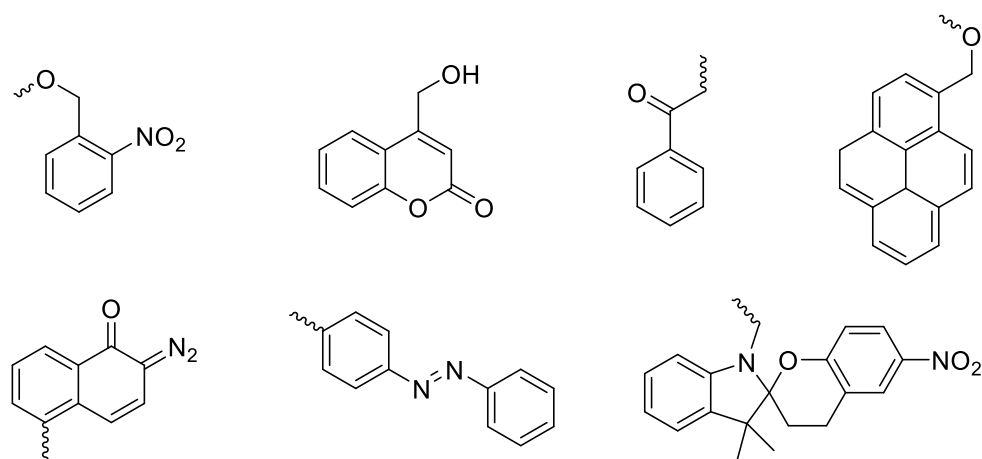
Scheme 2.6 Most frequently used structural motives for photocleavable protecting groups. From top left to bottom right: *ortho*-nitrobenzyl (oNB), coumaryl, phenyacyl, benzyl (and its polyaromatic derivates), diazonaphtoquinone (DNQ), diazo and spiropyran.

In biochemical research oNBs have a long history of application, for example for photo uncaging adenosine triphosphate or the release of the antitumor drug 5-fluorouracil.[209,210] There are also many examples of applications for DDS systems based on the light-responsive

degradation of oNB functionalized polymers in micelles, polymersomes, nanogels and nanoparticles. Its first applications can be dated back to 2008.[109,110,137,211–215] In all cases, the photo cleavage is based on the same photo-redox reaction. First reports of a photoinduced isomerization of *o*-nitrobenzaldehyde into the corresponding nitrosobenzoic acid were reported in 1901 and were further investigated and described in 1962.[204,216] Later, the mechanism of this intramolecular redox reaction was thoroughly investigated and classified as a NORRISH-Type II reaction.[125,217,218]
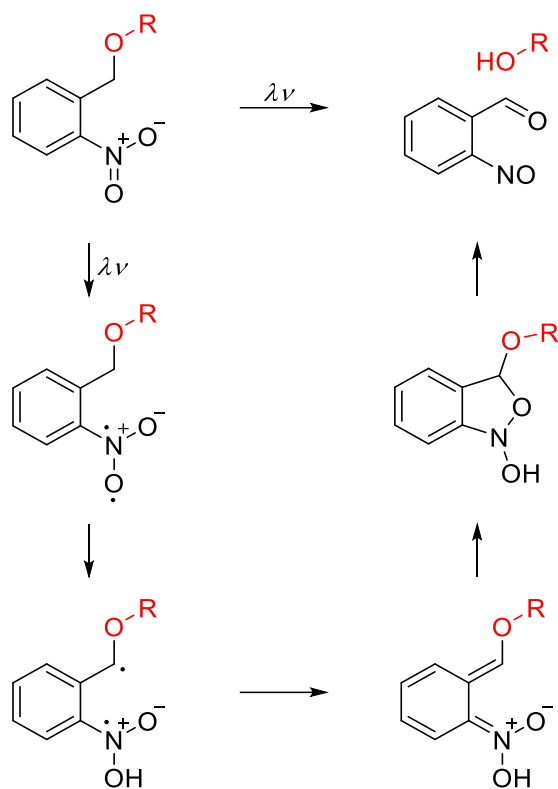
Scheme 2.7 Proposed NORRISH-type II reaction mechanism of the photoinduced redox reaction of *ortho*-nitrobenzyl (oNB) ethers.[205,207]

As shown in Scheme 2.7, the reaction gets initiated by a photon that breaks the N=O π bond of the nitro group into a diradical. The oxygen radical abstracts a proton from the benzyl group and forms an *aci*-nitro compound (bottom right) and then forms a five-membered ring. The OR group that is attached to the benzylic position gets cleaved and a nitroso aldehyde is formed. oNB groups are quite versatile regarding to the R group. Alkoxide, phenolates, esters, carbamates, phosphates, carbonates, or thiolates can all be cleaved in high yields by irradiation. Depending on the media and substrate specifics, the decay of the *aci*-nitro compound may vary in detail.[219]

The interaction between matter and electromagnetic radiation is wavelength specific. Each wavelength interacts with certain parts of atoms or molecules in a very particular way. Gamma radiation, for example, can knock electrons out of the inner shell of an atom, the absorption of infrared radiation causes molecular bonds to vibrate and microwave radiation causes

molecular chains to vibrate and rotate. UV-radiation is characterized by the ability to break molecular bonds and generate e.g. radicals. This makes it an ideal initiator for a wide spectrum of photoreactions. However, in particular irradiation with light of the UV-C and UV-B regions can be harmful to biological systems. In fact, it is so harmful that it is used for sterilization of water or surfaces. On the human skin, radiation can cause altering protein, lipids and nucleic acids/DNA, which can turn into skin cancer.[220] This leaves only a small section of the UV-spectrum as an applicable trigger. Irradiation with UV-A light (315 – 380 nm) can interfere with photo responsive molecules but nevertheless can be applied in biological systems, when applied in moderate intensities. But UV-light suffers from a poor penetration depth of below 1 mm into tissue, limiting its medical applicability drastically. The penetration depth of light increases consecutively with its wavelength and reaches about 5 mm at near infrared area (NIR, > 780 nm). [208,221] For the required wavelength to cause covalent bond cleavage, the absorption maximum of the chromophore group is the most used criterion. Although there is a correlation between these two values, the absorption maximum is not equivalent to the wavelength that cases the highest reaction rate.[222] Often the reactivity maximum is strongly redshifted compared to the absorption maxima.[223] As an example for this rather recent findings, the absorption spectra and the action plot (conversion rate relative to irradiation wavelength) of an oNB diol is shown in Figure 2.10. The Diol has a local absorption maximum around 250 nm and a UV-cutoff below 230 nm. However, the conversion rates increase to only above 300 nm, reaching maximum at 350 nm and falls fast at 400 nm.

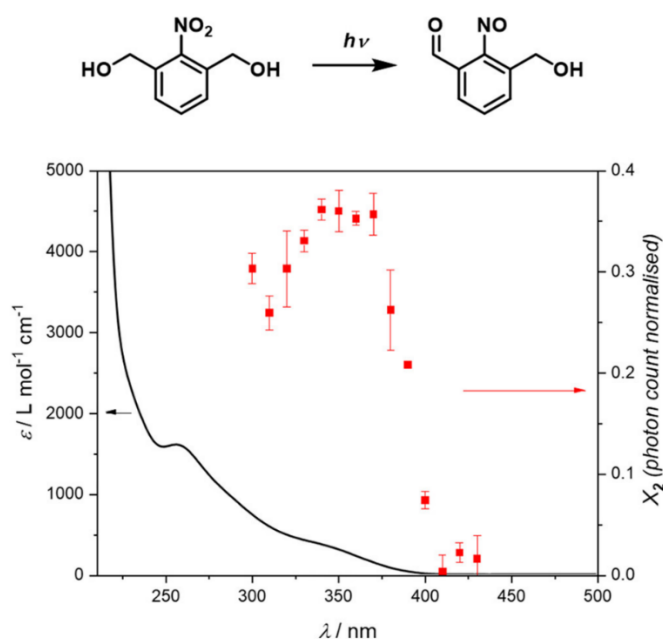*Figure 2.10* Top: Photoisomerization of an oNB diol to its corresponding nitroso benzaldehyde. Bottom: Absorption spectra of oNB diol and the action plot of its photoisomerization in acetonitrile-d_3 showing the photon-normalized conversion rate X_2. Maximum conversion rate is significantly red shifted compared to the absorption maxima. Reprinted with permission from ref. [224] © 2021 American Chemical Society.

Huge efforts were made to develop derivates of the core oNB structure to achieve a bathochromic shift of the absorption maximum, but also to increase the quantum yield, to maximize the conversion rates at higher wavelength and consequently to higher penetration depth.[205] Two main positions are substituted to modify the properties of oNB groups. A methyl group in the benzylic position increases the quantum yield and moreover it causes the formation of a ketone instead of the aldehyde as a product. It is therefore thought to have less interference with proteins.[140,225,226] A substitution of the aromatic ring was found to have only minor effects on the quantum yield. However, the absorption maxima can be shifted by the introduction especially of electron donating groups like methoxy-groups, 1,2-methylendioxybenzol or benzofuran.[140,225,227–229] Despite the advantages of the substituted oNB derivatives, they have been used rarely in DDS and in most applications the classical oNB without substituents is used. Reasons for this could be the lower synthetic effort, sufficient properties to introduce model concepts or the more extensive studies on the well-known derivatives.[139,210,230–233] With increasing wavelength of the light, the penetration depth may rise, but the ability to cause cleavage of covalent bonds declines rapidly. NIR responsive chromophores are an intriguing approach, however penetration depth is still very limited (about 5 mm) and sophisticated strategies are necessary for a functional delivery system. This goal can be accomplished by thermal release of photothermally responsive systems, or upconverting nanoparticles (UCNPs), which both require an inorganic core with a smart polymeric shell or two-photon absorbing chromophores, which require high intensity NIR laser and only reach necessary photon densities in a small confocal volume.[234–239] Despite the mentioned limitations, the high spatiotemporal control and easy application make light degradable DDS of interest for future therapies in highly specialized applications such as photodynamic therapy (PDT) and for endoscopic and minimally invasive procedures.[109,240]

2.6 Dually responsive systems for accelerated degradation

Novel dual and multi-stimuli sensitive polymeric nanoparticles that react to a combination of two or more stimuli are being developed to further enhance drug release capabilities. The integrated reactivities can be addressed either sequentially or simultaneously to give unprecedented control over drug delivery and enhance anti-cancer efficiency of the DDS.[241] Endogenous (e.g. pH, redox, enzyme) and exogenous (e.g. light, magnetic field, ultrasound) stimuli can be combined with each other in different combinations to achieve set goals. For example, Soppimath *et al.* synthesized pH- and temperature-responsive polymeric micelles, whose lower critical solution temperature (LCST) in mildly acidic conditions were below the temperature of physical conditions while in neutral and basic conditions was above 40 °C.[242]

In an idealized classification the interaction between different functionalities can be categorized into "AND" and "OR" gate NPs. "OR" gate NPs combine two stimuli whereas one of two possible triggers is sufficient to initiate drug release. Such a system is rather easy to create by synthesizing statistically or iterative copolymers with two different stimuli-responsive functionalities. These vehicles are ideal for synergistically working triggers, for example pH and redox responsive DDS for anti-tumor drug delivery, where the release in the targeted area (high GSH level, low pH values) is further enhanced compared to healthy tissue.[243,244] Endogenous stimuli can also be combined with exogeneous stimuli. For example, ZHANG *et al.* recently published a photo and acid dual degradable polymeric nanoparticle with oNB dithiol and ketal functionality displayed in Figure 2.11Figure 2.11. These particles can be degraded both by the presence of acid and by irradiation with UV-light.[6]
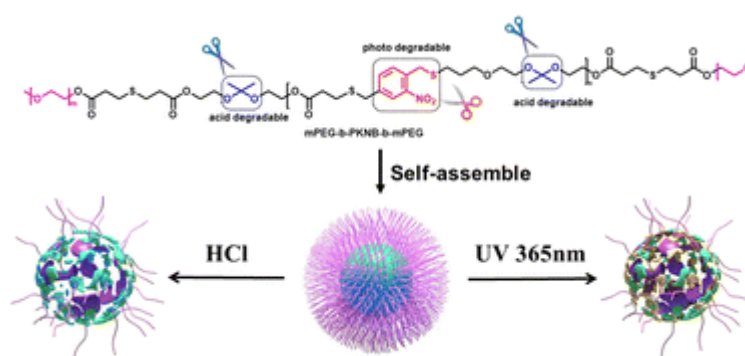
Figure 2.11 Photo and acid dual degradable polymeric nanoparticles from *o*-nitrobenzyl dithiol with thiol-ene click polymerization. Reprinted with permission from ref. [6] © 2023 The Royal Society of Chemistry.

"AND" gate NPs on the other hand only release their cargo when both of two stimuli are present. Figure 2.12 shows a delivery system published by MAHMOUD *et al*. It consists of a polymer with pH degradable ketal functions that are protected from mildly acidic conditions by the hydrophobicity of the polymer. In the presence of reactive oxygen species (ROS), the oxidation sensitive thioether gets oxidized to sulfoxide.
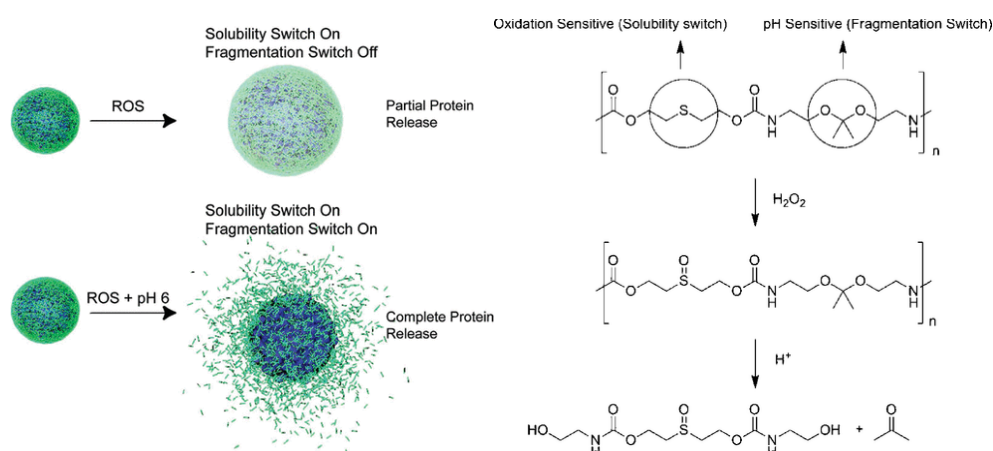
Figure 2.12 Protein-loaded polymeric nanoparticles only show partial release in the presence of reactive oxygen species (ROS). Only the concurrent presence of low pH values enables complete protein release (left). H_2O_2 oxidates thioether, the higher solubility allows the admittance of acid into the particle and cleavage of the ketal bonds. (right) Adapted with permission from ref. [245] © 2011 American Chemical Society.

By this oxidation the polymer undergoes a polarity switch to a more hydrophilic backbone and allows admittance of the mildly acidic media. This causes complete particle breakdown and full release of the cargo.[245] Another example was published by JÄGER *et al.*, where secondary amino groups in the polymers sidechain were protected by boronic esters. Only the ROS sensitive cleavage of boronic esters deprotected the amino group and allowed its protonation in acidic environment to cause disassembly of the micelles, making this a ROS and pH "AND" gate responsive DDS. Since there is always at least a partially responsiveness to each stimulus individually these approaches can also be interpreted as stimuli accelerated degradations.[7] JAZANI and OH identified three fundamental mechanisms of accelerated degradation of acid-degradable nano assemblies.[246] The first strategy is based on incorporating tertiary amine groups into acid-degradable copolymers. When tertiary amine groups are protonated, hydronium ions can more easily enter the hydrophobic core, increasing their hydrophilicity and accelerating their breakdown.[247] In similar fashion the hydrolysis can be promoted by copolymerization of methacrylates bearing pendant tertiary amino groups with acid cleavable methacrylates.[248] The second strategy involves a stimuli-responsive cleavage, for example polyketals bearing oNB masked carboxylate functionalities in the polymeric backbone. Upon irradiation the polarity of the polymer gets increased and causes an acceleration of the degradation.[249] The third strategy is a self-amplification of acetal degradation through the formation of acids during the degradation process. This was already an undesirable side effect at the early stages of the development of poly(ortho esters) based on butyrolactone, but it can also be used to deliberately accelerate the release of active ingredients.[136,250]

Maintaining a balance between fast drug release at the site of action and stable particles with low premature release in bloodstream and healthy tissue is an important aspect for the design of smart drug delivery systems. Only a few strategies have been explored to accelerate the hydrolysis of acid-cleavable polymers and their particles despite the huge potential for improvement of therapeutic efficacy by dually responsive polymeric nanoparticles.

3 Results and discussion

The following chapter is divided into two parts, dedicated to different synthesis platforms. The Chapter 3.1 is devoted to the synthesis and characterization of pH- and light-responsive polyketals. Nanoparticles have been formulated and degraded in buffered solutions with and without prior UV-irradiation. Studying the degradational behavior showed that implementation of light cleavable oNB groups into the backbone of polyketals allows the hydrolytic particle breakdown to be accelerated by a single irradiation event. The Chapter 0 discusses the synthesis of light cleavable polyurethanes derived of the lysine based diisocyanate LDI combined with hydrophilic building blocks, the formulation and study of the degradational behavior of those.

3.1 Light accelerated degradation of polyketals

Stimuli responsive polymers undergoing a change in structure and properties upon exposure to exogenic stimuli such as light show great potential as smart drug delivery systems. Although their unique properties provide high control over time and location of drug release, they rely on prolonged exposure times towards the trigger and suffer from incomplete degradation. Polyketals containing acetonide linkages are known for their fast and tunable degradation kinetics, easy synthesis and pH neutral degradation products. The hydrolysis kinetics of such hydrophobic nanoparticles depend on the diffusion of water through the polymeric matrix and the molecular weight of the polymer. By introduction of light cleavable *ortho*-nitrobenzylic (oNB) motifs to hydrolysable polymers we designed smart polymeric nanoparticles whose permeability can be increased by a single irradiation event and thus significantly accelerate particle degradation kinetics.

3.1.1 Synthesis of small molecules and polymers

To ensure even distribution of the responsive monomers, both the light-responsive monomer and a filler comonomer to build the polymer backbone, should have similar reactivity. The easiest conceivable method is to use monomers with high structural similarity, as it can be assumed that they also have similar reactivity. As a synthesis platform benzene dimethanol (**3**) was chosen as diol component, as the aromatic structure makes it simple to find a structural similar oNB chromophore and the degradation kinetics of benzene dimethanol based PPADK particles are in the range of hours to days.[163] The light cleavable unit was chosen to be the chromophore oNB benzene dimethanol (**2**) since it has high chemical similarity to

benzene dimethanol (**3**) in PPADK (**5**) and is expected to polymerize evenly along the polymeric backbone.

Scheme 3.1 Reduction of nitroterephthalic acid (**1**) to the oNB diol (**2**).[233,251]

The synthesis of chromophore **2** was carried out based on a literature known one step reduction of nitroterephthalic acid (**1**) with borane tetrahydrofuran complex overnight.[233,251] Crude product was purified by recrystallization from chloroform and yielded 74 % of the light-responsive oNB monomer **2**. The structure was confirmed by NMR spectroscopy, determination of the melting point and UV-VIS spectroscopy. As described in the literature, the absorption maximum peaked at 260 nm.

Scheme 3.2 Synthesis of the polyketal PPADK (**5**) by polycondensation of benzene dimethanol (**4**) and DMP (**4**).

As a reference material and to establish the synthesis platform for the formation of polyketals, the poly(1,4-phenyleneacetone dimethylene ketal (PPADK, **5**) was synthesized based on the literature procedure by HEFFERNAN, MURTHY *et al.*[159] The Synthesis of PPADK (**5**) was carried out in a two-neck round bottom flask with a thermometer, a VIGREUX column and a short path distillation head. To obtain polymer, removal of the formed methanol was necessary to shift the equilibrium towards the side of the product. The boiling point of the comonomer dimethoxypropane (DMP, **4**) is 83 °C, the boiling point of methanol is 65 °C. This boiling point difference is not sufficient to selectively rectify the methanol and carry out the synthesis with equal amounts of DMP (**4**) to benzene dimethanol (**3**). Consequently, DMP gets continuously distilled off and must be replaced gradually. After the reaction has ended, the catalyst must be deactivated by addition of a base, such as Et$_3$N, to prevent decomposition of the polymer during the precipitation in cold methanol. Additional base was added to the precipitant to ensure polymer stability. PPADK (**5**) was isolated in a yield of 75 – 85 % and with an average number molecular weight (M_n) of 4 400 – 6 200 g/mol (THF-SEC). UV-VIS spectroscopy of the final polymer shows a maximum absorption at 265 nm, slightly bathochromic shifted compared to the oNB monomer.

Attempts to modify the procedure, such as varying the temperature, reaction time and solvent, to obtain higher molecular weights were not successful. Structure and molecular

weight of the polymer were confirmed by ^{1}H-NMR spectroscopy as well as SEC. Et$_3$N must be added to CDCl$_3$ prior to solving the sample for spectroscopic analysis since the acidity in deuterated chloroform is sufficient to decompose the polymer within minutes and formation of acetone can be observed in the ^{1}H-NMR spectrum during successive measurements. Analysis of Et$_3$N stabilized samples did not show any signs of degradation.

Based on the synthesis of PPADK (**5**) an oNB containing derivate with 10 % of the light-responsive monomer oNB benzol dimethanol (**2**) was synthesized. Photolytic cleavage of the polymeric backbone must only be accomplished partially since the main course of degradation will be by hydrolysis. For this reason, it was estimated that 10 % of light-responsive monomers are sufficient to induce hydrolytic degradation. However, it is obvious that this value can have a great influence on several factors such as the degradation behavior or the toxicologic profile of the particles. The proportion of cleavable monomers could be adjusted at a later stage to control the hydrolysis kinetics of the particular system.
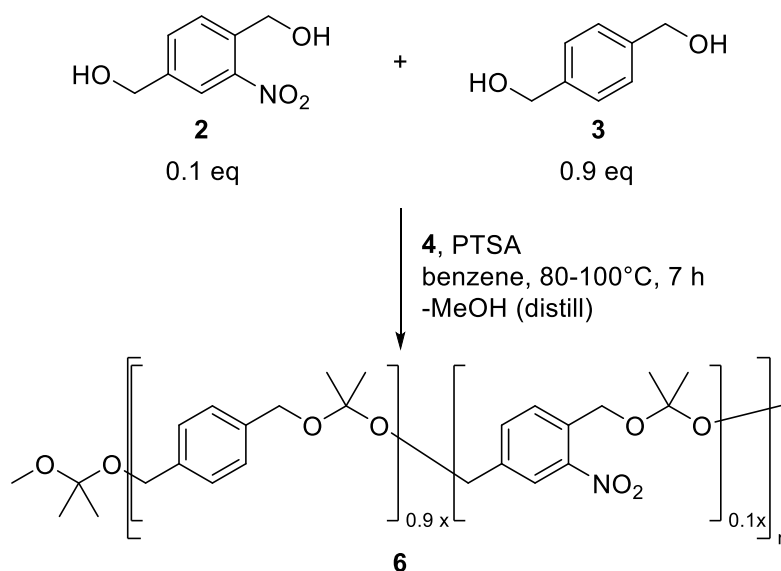
Scheme 3.3 Synthesis of the polyketal oNB PPADK (**6**) by polycondensation of benzene dimethanol (**4**), the oNB diol **2** and DMP (**4**).

As displayed in Scheme 3.3 the polymer oNB PPADK (**6**) was synthesized in an identical procedure as the polymer **5** but with 10 % of light-responsive oNB monomer **2** in the initial reaction mixture. The final polymer was isolated in yields around 80 % after purification and with a number average molecular weight (M_n) of 4 800 – 6 200 g/mol (THF-SEC). The UV-VIS spectrum of the product showed an absorption band at 260 nm, which corresponds to the absorption maxima of the light cleavable monomer, indicating successful incorporation of the monomer **2** into the polymer. This finding is supported by the ^{1}H-NMR results. Based on the NMR data, the ratio of the two monomers **2** and **3** in the polymeric backbone is 0.94:9 and aligns with the used 1:9 ratio in the feedstock.

3.1.2 Light induces polymer degradation

As proposed in Chapter 1.1, an initialization or acceleration of the hydrolytic degradation of oNB PPADK nanoparticles requires decrease of the molecular weight upon irradiation of the polymer. To examine the properties during the UV-irradiation, oNB PPADK (**6**) and, as a reference, PPADK (**5**) have been irradiated with UV-light with a wavelength of 320 – 480 nm an intensity of 300 mW/cm² in a DCM solution (stabilized with 0.1 % Et₃N) and have been characterized by UV-VIS spectroscopy and SEC analysis.
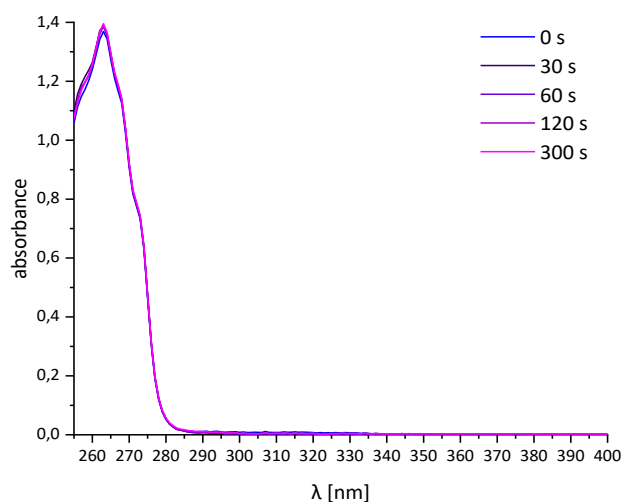

Figure 3.1 UV-VIS spectra of PPADK (**5**, 0.4 g/L) in DCM during irradiation with UV-light.

In the first step of characterization, UV-VIS spectra were measured in between subsequent irradiation steps to detect any changes that indicate that photoisomerization is taking place. The UV-VIS spectra of PPADK (**5**) displayed in Figure 3.2 shows a sharp absorption band with a maximum absorption at 265 nm and rapidly declines to no measurable absorbance at about > 280 nm. This is consistent with the expected range of absorption of benzene dimethanol (**3**) as the starting material. The absorbance of oNB PPADK (**6**) shown in Figure 3.2 has a maximum at 260 nm and falls off continuously at higher wavelength with a plateau around 315 nm and then further decreases until reaching zero absorbance around 400 nm. In the first set of experiments, the polymer concentration was chosen to be 40 mg/L. However, the absorbance of PPADK polymer was very low. It was concluded that with this low absorbance the probability of photoisomerization was very low and changes of the absorbance would be difficult to recognize due to the worse signal to noise ratio. For this reason, the experiment was repeated with a 10-fold concentration of PPADK (**5**) (Figure 3.2, left). However, in case of oNB PPADK (**6**) the absorbance of 40 mg/L was about 0.8 – 1.2 which is expected to show a linear relationship of concentration to absorbance according to the Lᴀᴍʙᴇʀᴛ-Bᴇᴇʀ law. For reasons of better visual comparability only results of the high concentration PPAKD solutions

are presented, however, observations did not differ from the results of the more diluted samples.
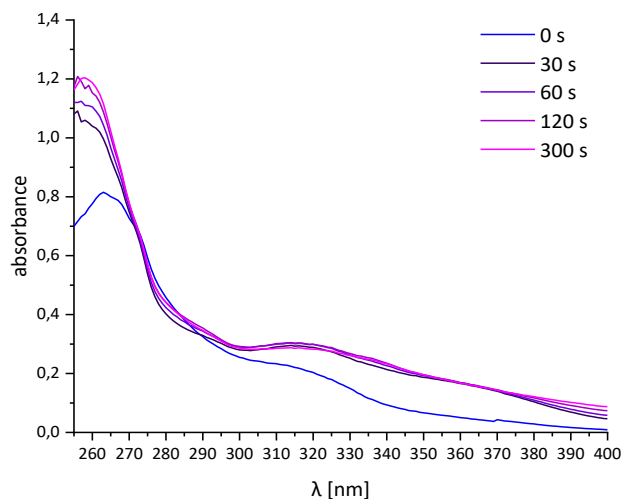

Figure 3.2 UV-VIS spectra oNB PPADK (**6**, 0.04 g/L) in DCM during irradiation with UV-light.

As can be seen in the spectral data, upon irradiation with UV-light no change in the absorbance of PPADK could be observed even after extended irradiation times up to 300 s. oNB PPADK (**6**) on the other hand shows a sharp increase of absorbance at the maximum around 260 nm and a decline of absorbance at the broad absorbance band at 300 – 400 nm. After fast initial changes during the first seconds of irradiation, the change of absorbance is lower at later timeframes. This data supports the successful incorporation of the oNB bearing monomer **3** into the polymeric backbone as well as a photoisomerization reaction of the oNB group upon irradiation of the oNB PPADK (**6**) solution. The majority of the photoisomerization takes place during the first seconds of the irradiation, after about 2 min almost no further isomerization takes place. However, it should be noted that this value can highly depend on the concentration due to absorption effects.

To investigate, if the photoisomerization transcends into a degradation of the polymer, irradiated samples have been analyzed by SEC. Both PPADK (**5**) and oNB PPADK (**6**) have been dissolved in DCM (stabilized with 0.1 % Et$_3$N) with a concentration of 1.6 mg/L. 3 mL of sample were irradiated for 0 – 300 s with the above-mentioned UV-light source in a 1 cm cuvette. The DCM was removed in vacuum and samples were resolved in THF for SEC analysis. Figure 3.3 shows the normalized elution curves of PPADK (**5**, left) and oNB PPADK (**6**, right) of the native polymers and after each irradiation step.
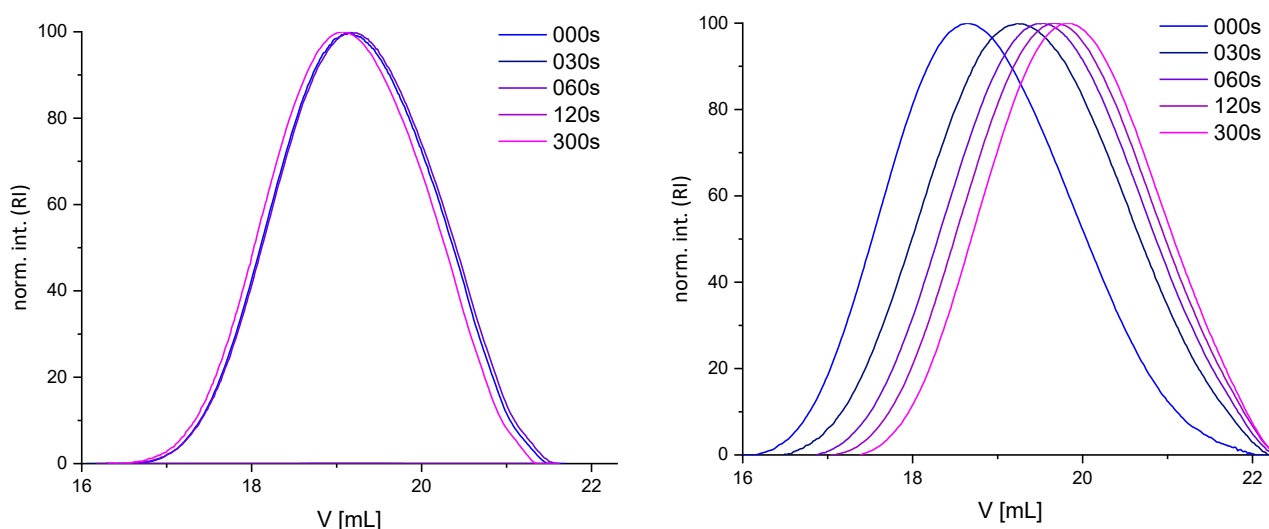
Figure 3.3 Normalized elution curves of PPADK (**5**, left) and oNB PPADK (**6**, right) of the native polymers and after irradiation with UV-light. oNB PPADK shows a strong decrease of the molecular weight.

The SEC elution curves shown in Figure 3.3 show, that PPADK (**5**, left) remained at the same molecular weight in each irradiation step, while irradiated oNB PPADK samples (**6**, right) appeared at higher elution volumes, the longer they were exposed to UV-light. With PS-calibration of the THF-SEC, number average molecular weights of about 5 000 g/mol were ascertained in both cases, which is consistent with the number average molecular weight calculated from the ^{1}H-NMR data. According to the data plotted in Figure 3.4, the determined number average molecular weights of the light-responsive oNB PPADK (**6**) decreased fast from 5 000 g/mol and converged towards 2 000 g/mol while irradiation of the PPADK (**5**) reference material showed no decrease of the molecular weight. The convergence indicates that further irradiation of the polymer would not lead to significant decrease of the molecular weight.

Figure 3.4 Average number molecular weight of native and irradiated PPADK (**5**, blue) and oNB PPADK (**6**, pink) determined by THF-SEC with PS-calibration.

33

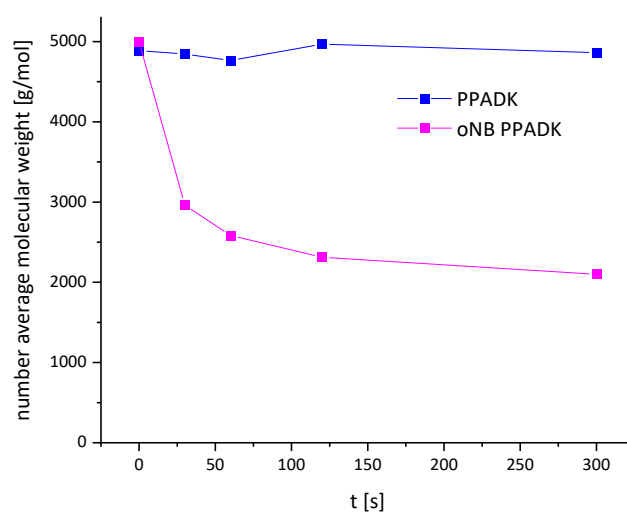The UV-responsive degradation studies reveal that copolymerization of the polyketal PPADK with an oNB functionalized monomer (**2**) lead to a UV-degradable polyketal. Upon irradiation the polymer conducted fast photo-isomerization and degraded within the first 30 s to 60 s of the irradiation towards an average number molecular weight below 50 % of the initial molecular weight of the polymer.

3.1.3 Formulation of nanoparticles

Polymeric nanoparticles have been formulated by nanoprecipitation from THF into aqueous PVA solution. Based on previous procedures a method was developed. The most convenient and reliable method comprised 5 mg polymer in 1 mL THF and fast injection into 10 mL of 2 % PVA solution with submerged cannula. This method resulted in the formation of nanoparticles with a hydrodynamic diameter ranging from 150 nm to 190 nm and monomodal size distribution with a small PDI of 0.05 to 0.14. Such narrow size distributions are desirable as they lead to precise size-dependent properties. Higher concentrations up to 10 mg of polymer were tested, however, formation of macroscopic precipitate on the dispersions surface implies a non-optimal NP formulation. Also, polydispersities of these solutions were much higher and, in some cases, a multimodal particle size distribution was observed. Variation of PVA solution between 1 – 5 % did not show any significant influence on the particle size or PDI. 5 % PVA solutions are tedious to prepare due to the poor solubility and particles require a prolonged centrifugation time during workup due to the high viscosity of the solution. For this reason, 2 % PVA was chosen as the surfactant concentration.
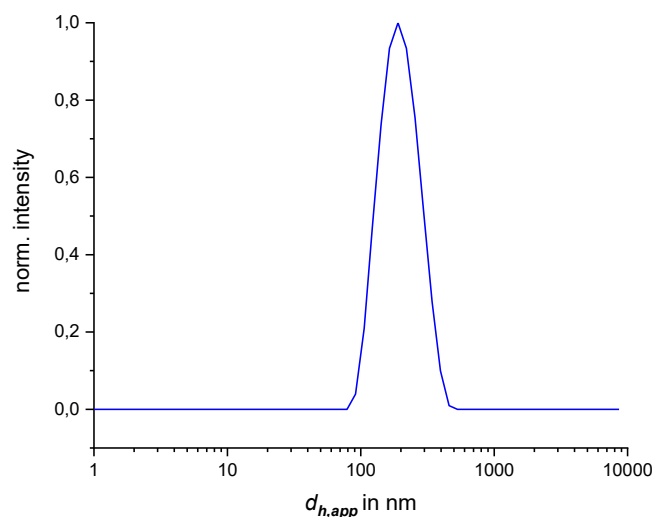

Figure 3.5 Particle size distribution of PPADK (**5**) nanoparticles determined by dynamic light scattering (DLS).

To get better understanding into the workup process, a thorough workup was carried out with prolonged centrifugation times and, analyzation of both, particles and supernatant solutions,

isolation of the nanoparticles by freeze drying. Crude NPs have been prepared as described above and were analyzed by DLS. As the dispersion was diluted 1:50 in demineralized water, the presence of PVA did not interfere with the results of the DLS measurement. This was also confirmed by multiple additions of 2 % PVA stock solution with consecutive unchanging measurement results.

Table 3.1 Particle diameter (z-Average), polydispersity index (PDI) and scattering intensity (count rate) of nanoparticle dispersions and supernatant fractions at different stages during the workup of PPADK nanoparticles.

	z-Ave (nm)	*PDI*	*count rate* (kcps)
crude NPs	185.1	0.100	20 000
supernatant 1	108.7	0.146	2 300
supernatant 2	142.4	0.117	945
supernatant 3	150.6	0.096	779
final nanoparticles	199.5	0.073	16 000
redispersed particles	246.7	0.234	7 800

Crude nanoparticle dispersion was divided into fractions and centrifuged for 2 h at 12 000 RCF. The supernatant was removed by decanting and centrifugate was redispersed in demineralized water. DLS measurements of the supernatant revealed that despite the prolonged centrifugation time, there were still considerable amounts of particles present in the dispersion. The particle size in the supernatant, at around 109 nm, is significantly smaller than the mean particle diameter of the raw NP dispersion, in which the mean diameter was 185 nm. Consequently, the average diameter of the isolated and purified particles is expected to rise, which indeed can be observed after the last purification step (final nanoparticles) in Table 3.1. This observation aligns with the STOKES-Equation, which proclaims higher sedimentation speeds for larger spherical bodies. Also, the equation states that viscosity of the dispersant heavily influences the sedimentation time. Since after the first isolation only water was used to redisperse the particles, the centrifugation time was lowered to 1 h per workup step as its viscosity is significantly lower than from the PVA solution. In both cases there were still particles observable in the supernatant after decanting, however scattering intensities indicate, that loss of particle yield by the later purification steps is lower than in the first workup step. After purification three aliquots were taken, lyophilized and the yield was determined as 72 % ± 15 %. The relatively high spread of the values is due to the small sample size. To isolate the purified polyketal particles, 5 % w/w of trehalose was added to the purified particle dispersion and the dispersion was lyophilized. Trehalose is applied as a lyophilization agent, that build scaffolds to prevent nanoparticle coagulation and ease redispersing.[252]

However, DLS measurements of lyophilized polyketal nanoparticles that were redispersed did not meet the quality criteria as shown in Table 3.1. Measured particle diameter and PDI significantly increased compared to the purified nanoparticles. This indicates that despite intensive homogenization by ultrasound and using a vortex, the particles have not completely separated again and are agglomerating. Since an influence on degradation properties could not be excluded, only freshly prepared nanoparticles were used for their characterization. As high yields are an irrelevant metric for characterization experiments, the time for separation by centrifugation was lowered to 10 min per run to optimize the work up process.

3.1.4 Particle degradation NMR

In the following the degradation behavior of PPADK and oNB PPADK nanoparticles in isotonic buffer solutions should be characterized before and after irradiation to determine, how the partially photo cleavage of light-responsive polyketals influences the particle breakdown at different pH values. The most widespread used buffering system is the PBS (phosphate-buffered saline) buffer solution. It contains 137 mM NaCl, 2.7 mM KCl and 12 mM of the active buffering ingredients (hydrogen phosphates). However, the pH value of the PBS buffer is 7,4 per default and can be only varied slightly. For characterization of the pH dependent properties a buffering system that covers the whole range from pH 3.0 to 7.4 should be available. For this reason a set of isotonic buffering systems based on the MCILVANE buffer chart were calculated.[253] In PBS buffer solutions, only a small portion of the containing ingredients is actually buffering the pH value while the majority are pH neutral salts and only contribute to the salinity. In later degradation experiments described in Chapter 3.1.5, a buffer composition closer to the PBS buffer (a citric-PBS) was chosen to more closely resemble a biological system and allow better comparability with elsewhere published particulate drug delivery systems. However, for the NMR degradation experiments citric acid should be used as an internal standard for quantification and therefore higher concentrations of the acid and base are required. Due to this the composition of isotonic citrate-phosphate buffers was calculated. The exact recipes of the citric-PBS buffers are listed in Chapter 4.2.

The MCILVANE citrate-phosphate buffer table provides a set of stock solution ratios of disodium hydrogen phosphate (component A) and citric acid (component B) for pH values ranging from 2.2 to 8.0. According to the HENDERSON-HASSELBACH equation, the pH value of a buffer solution is only dependent on the molar ratio of the buffering components and not on their absolute concentration. The MCILVANE buffer chart is not only true for the given volumes of stock solutions but is valid for every substance amount that fulfills the same ratio. For this reason, molar ratios r for every pH value were calculated according to equation (1).

$$r(pH) = \frac{n_A}{n_B} \quad <=> \quad n_B = \frac{n_A}{r(pH)} \tag{1}$$

In order to generate a data set that provides a good approximation of the mixing ratio of the components for any given pH value (2.2 − 8.0) between the given data points, the ranges between the given table values were linearly interpolated and the required molar ratio *r* for each pH was calculated. The acquired data is displayed in Figure 3.6.
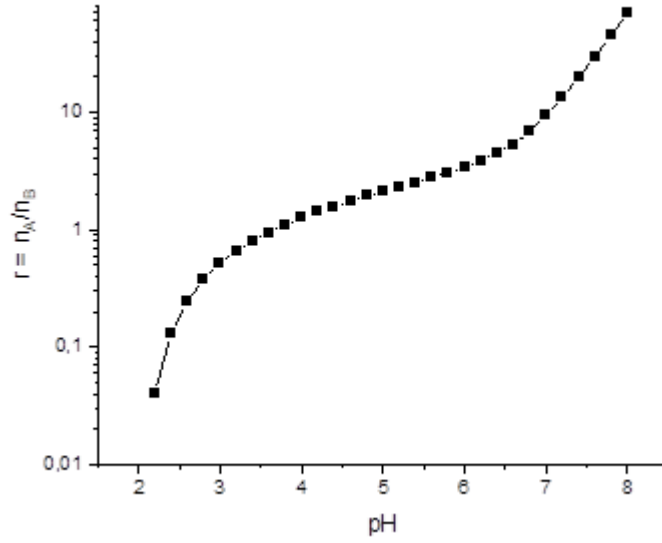

Figure 3.6 Plot of the numerical table that describes the required molar ratio *r* of the buffering components disodium hydrogen phosphate (A) and citric acid (B) to create buffer solutions with the targeted pH values.

The osmolarity or osmotic concentration $c_{osm,i}$ is dependent on the substance concentration c, the substance specific VAN`T HOFF factor ($L_{iso,i}$) and the cryoscopic constant (E_n) of the solvent and can be expressed as shown in equation (2).

$$c_{osm,i} = c \cdot \frac{L_{iso,i}}{E_n} = \frac{n \cdot L_{iso,i}}{V \cdot E_{n,H_2O}} \tag{2}$$

The osmolarity of a mixture is given by the sum of the osmolarity of the individual components. For a binary mixture of the buffer components disodium hydrogen phosphate (A) and citric acid (B), the total osmotic concentration c_{osm} can be calculated according to equation (3).

$$c_{osm} = \frac{n_A \cdot L_{iso,A}}{V \cdot E_n} + \frac{n_B \cdot L_{iso,B}}{V \cdot E_n} \tag{3}$$

According to equation (1) the amount of substance B (n_B) can be expressed as a term of the molar ratio $r(pH)$ and the n_A. If equation (1) is inserted into equation (3) and converted by factoring out the term $n_A/V \cdot E_n$, equation (4) is obtained.

$$c_{osm} = \frac{n_A}{V \cdot E_n} \left(L_{iso,A} + \frac{L_{iso,B}}{r(pH)} \right) \qquad (4)$$

Transformation of equation (4) results in equation (5), which allows to calculate the required substance A (disodium hydrogen phosphate) for every desired pH value and osmotic concentration taking into account the required volume of the buffer solution and the literature values for $E_n = 1.86 \frac{\text{K} \cdot \text{kg}}{\text{mol}}$, $L_{iso,A} = 4.3 \frac{\text{K} \cdot \text{L}}{\text{mol}}$ and $L_{iso,B} = 2.0 \frac{\text{K} \cdot \text{L}}{\text{mol}}$. The amount of substance of component B (citric acid) can easily be calculated by equation (1) afterwards.

$$n_A = \frac{c_{osm} \cdot V \cdot E_n}{L_{iso,A} + \frac{L_{iso,B}}{r(pH)}} \qquad (5)$$

Degradation kinetics of pH responsive polyketals were tracked by ^{1}H-NMR spectroscopy. 5 mg of PPADK polymer were formulated into nanoparticles as described before. However, during workup by centrifugation redispersed fractions were fused and concentrated to yield in a singular fraction of 1 mL after the third purification step. NPs were separated by centrifugation again and redisperse in 37 °C citric-PBS buffer solution with various set pH values between pH 3 and pH 7.4. The sample was measured at regular intervals using NMR spectroscopy and incubated at 37 °C between measurements with constant stirring.
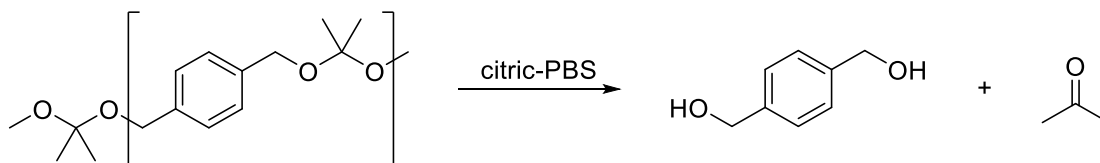

Figure 3.7 Acid catalyzed hydrolyzation of pH responsive polyketals lead to the formation of diol and acetone.

As shown in Figure 3.7 degradation in aqueous solution leads to the formation of the diol and acetone as a degradation product. Increase of signal intensity of the degradation products could be quantified relative to the signals of the CH$_2$ group of citric acid as an internal standard. After 120 h of degradation, several aliquots of DCl were added to fully degrade the remaining NPs. PPADK and oNB PPADK particles were characterized in their native form and after 30 s of UV-light exposure after redispersion in the buffer solutions. Right after redispersion the NP dispersion was white colored and very cloudy due to their high concentration, which is required to allow reliable quantification in NMR spectroscopy. The absorption and scattering could possibly lead to an attenuated exposure to UV-light. As an opposing effect, the irradiation was carried out in NMR tubes with a diameter of 4.5 mm. These effects do not influence the comparison of any of the NMR degradation experiments but should be considered when degradation is compared to other degradation experiments.

As expected, the polymers formulated as nanoparticles did not show any signal in the ^{1}H-NMR spectrum. The CH$_2$ group of citric acid did show a clearly assignable signal at 2.77 ppm. As the degradation progresses, singlet signals at 2.21 ppm, 4.45 ppm and 7.4 ppm, which corresponds to the methyl group of acetone, the benzylic group and the aromatic group of

the diol, show a simultaneous increase in intensity. However, the acetone signal is getting broader and asymmetrical at later stages of the degradation and after full degradation by the addition of DCl and incubation for 30 min, the signal cannot be clearly assigned. The high reactivity of acetone in acidic environments with tautomerization and aldol chemistry could lead to the formation of byproducts. In addition, the high volatility of acetone could distort a quantification after several conversions for quantification. For this reason, acetone was dismissed as an analyzable marker. Benzylic protons of the diol were close to the HDO signal, which had a high intensity due to residual water from the NP formation. However, the aromatic protons from the diol were isolated signals, sharp and easy to evaluate and were chosen as a marker for the degradation of the nanoparticles for that reason.

Figure 3.8 shows the relative degradation of the non-irradiated PPADK NPs based on the normalized relative signal intensity of benzene diol and in Figure 3.9 the signal strength of its UV-irradiated counterpart is displayed. In both experiments, the pH 3.0 sample showed already a relative degradation of 3 % at the first measurement after the sample preparation, which was estimated to take 5 min. Within the first 48 h of degradation, the NPs at pH 3.0 achieved full degradation within the expected scale of deviation. At pH 5.0, the degradation was distinctly slower and reached $9 - 10$ % after 48 h and $10 - 20$ % after 120 h. The degradation of the samples with a pH value of 6.0 was even slower, and the lowest degree of degradation was observed at a pH value of 7.4, where almost no degradation of the particles was observed with 0.2 % and 1.2 % respectively.

In a direct comparison of native and UV-irradiated particles, only non-significant deviations without a clear trend can be recognized. At the data point after 48 h the degradation curves are congruent, after 120 h pH 5.0 shows a slightly increased degradation in case of the non-irradiated sample, at pH 6.0 the irradiated sample shows a slightly stronger degradation. After the addition of DCl, intensive, sharp and characteristic signals of benzene dimethanol can be identified in all samples. The observations from the spectroscopic analysis are consistent with the observations at the macroscopic level. The sample with the lowest pH value showed no residual turbidity after 24 h and was colorless and clear. The other samples, however, showed no perceptible decrease in turbidity. After addition of DCl and incubation, all samples were colorless and clear, indicating a complete degradation.
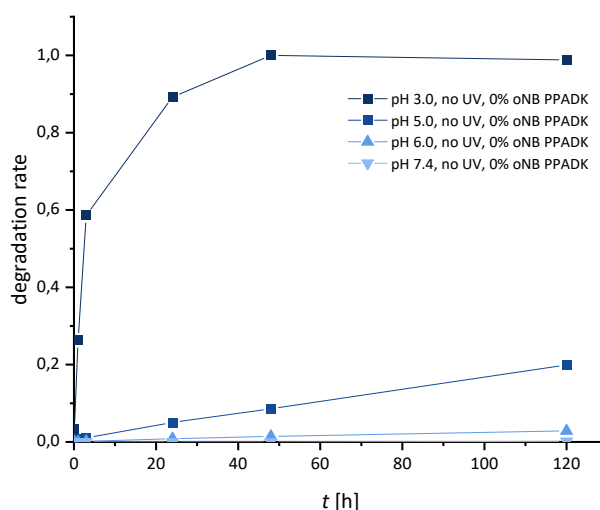
Figure 3.8 Degradation of PPADK (**5**) nanoparticles in citric buffer (in D_2O) without UV-irradiation based on ^{1}H NMR spectroscopic data.
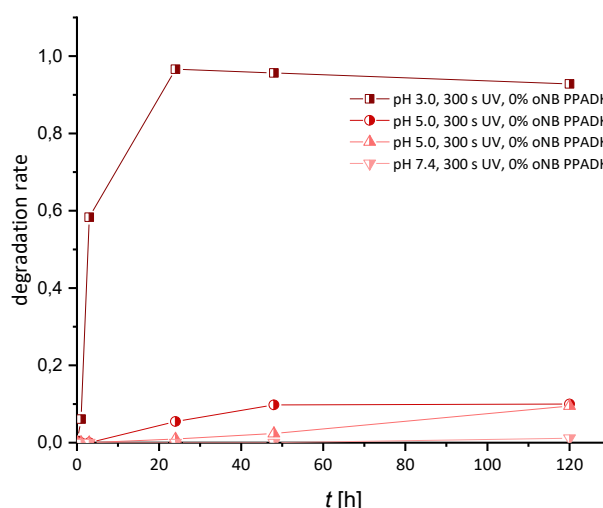

Figure 3.9 Degradation of PPADK (**5**) nanoparticles in citric buffer (in D_2O) after 300 s of UV-irradiation (right) based on ^{1}H NMR spectroscopic data.

The results show that the hydrophobicity of the particles plays a significant role in their degradation by protecting them from premature degradation. This suggests that hydrophobic surfaces can increase the stability of the particles, by reducing the penetration of aqueous media into the polymeric matrix. It was also found that the degradation of the nanoparticles is strongly dependent on the pH value of the medium. At lower pH values the degradation is significantly accelerated. As was expected, the UV-irradiated particles showed no significant difference in degradation compared to the non-irradiated particles. This suggests that irradiation has no effect on the degradation kinetics of the non-photosensitive PPADK nanoparticles.

The experiment was also conducted with oNB PPADK (**6**) nanoparticles to characterize the degradation behavior of light-responsive NPs after a singular and short UV-irradiation event. As in the previous experiment, polymer in particulate form did not show any signals in the NMR spectrum although it was irradiated previously. The degradation could also be tracked on the basis of the NMR signal caused by the benzene dimethanol relative to citric acid.

Figure 3.10 shows the normalized relative degradation of non-irradiated oNB PPADK NPs (**6**) and Figure 3.11 the degradation of their UV-irradiated counterpart. Unsurprisingly the pH 3.0 samples showed the fastest degradation again. The UV-irradiated samples showed a slightly faster degradation in the initial phase of the experiment. However, after 24 h both UV-irradiated as well as the native NPs have degraded > 90 % and virtually completely degraded within 48 h. At pH 5.0 degradation of the native oNB PPADK particles is about as fast as the PPADK NPs shown before. The irradiated oNB PPADK nanoparticles on the other hand degraded considerably faster. After 2 h, the UV-irradiated NPs degraded 6 % while the native NPs did not show any sign of degradation at all. After 48 h, native NPs showed 4 % erosion compared to 54 % in case of the UV-irradiated NPs and finally after 120 h of degradation, native NPs degraded 9 % and UV-irradiated 73 %. Similar behavior can be observed for the other pH values. At pH 6.0 final erosion of the UV-irradiated particles after 120 h amounts to 47 % compared to 4 % in case of the native NPs. Finally at pH 7.4 the degradation of the native NPs showed similar behavior as of PPADK NPs, but degradation of the UV-irradiated NPs was accelerated to 25 % after 120 h.
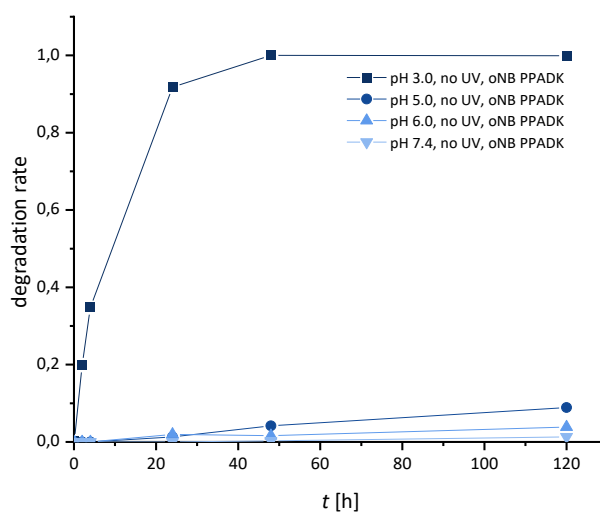
Figure 3.10 Degradation of oNB PPADK (**6**) nanoparticles in citric buffer (in D_2O) without UV-irradiation based on ^1H NMR spectroscopic data.
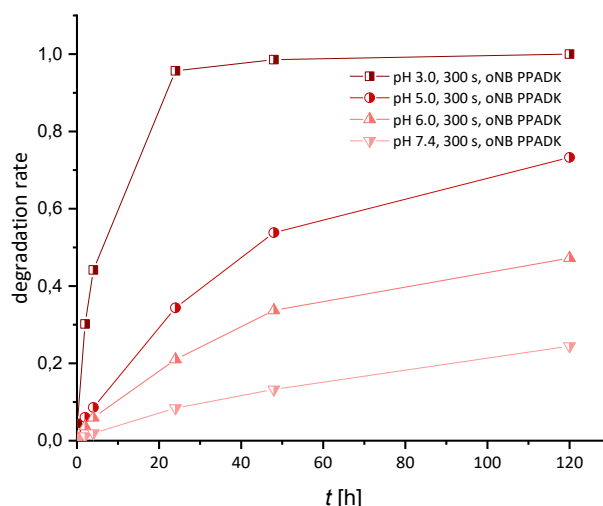

Figure 3.11 Degradation of oNB PPADK (**6**) nanoparticles in citric buffer (in D_2O) after 300 s of UV-irradiation (right) based on ^1H NMR spectroscopic data.

It can be concluded that oNB PPADK NPs show almost identical behavior as PPADK NPs when not irradiated. As before, hydrophobicity is limiting the fast erosion of ketal functional groups. A strong dependence on the pH value can be noted with the fastest erosion at low pH values and almost immeasurable degradation at neutral pH values. The copolymerization of oNB functionalized monomers had no significant effect on the degradation behavior of the particles. Prior irradiated oNB PPADK NPs overall showed accelerated degradation compared to the native counterparts. At pH 3.0, the acceleration was almost unnoticeable due to the fast degradation. Only two datapoints were in the evaluable degradation stage, revealing a too low time resolution to keep track of the degradation at so low pH values. At pH 5.0, 6.0 and 7.4, however, the particle breakdown is evidently accelerated. Putting the relative

42

degradation of all series of measurements in relation to each other shows an average acceleration by the factor 34.2 ± 5.6 after irradiation. Since significant erosion also takes place without irradiation at pH 5.0 and 6.0, the presumably correct interpretation of this effect is, that an acceleration takes place. However, in the case of pH 7.4, measured degradations ranged from 0.2 – 1.2 %. Considering the relatively high error of NMR quantification, this degree of erosion is negligible. For this reason, the irradiation of the oNB particles could also be described as an activation or on-switch of the nanoparticles.

3.1.5 Characterization of particles by light scattering

To study the particle characteristics and the kinetics of the particle degradation, light scattering experiments of incubated polyketal particles were conducted. To allow better comparability with the more common PBS buffered particle systems and to resemble biological systems as close as possible, the citric buffer from Chapter 3.1.4 was modified to match the properties of a PBS buffer. It contains 137 mM NaCl, 2.7 mM KCl and 12 mM of the active buffering ingredients, which were dependent on the composition of the MᴄIʟᴠᴀɴᴇ buffer chart that is shown in Figure 3.6.[253] The exact recipes of the citric-PBS buffers are listed in Chapter 4.2. Nanoparticles prepared as described in Chapter 3.1.3 were degraded in the isotonic citric-PBS buffer at pH values between 3.0 and 7.4. The relative degree of degradation was tracked by dynamic light scattering (DLS). The course of scattering intensity, an indicator for responsiveness of stimuli responsive particles, is well established, especially as an identificatory for particle degradation.[251] Within the first trial experiments it became apparent that the scattering intensity is declining to close to zero in under 24 h, even in case of the pH 7.4 sample, although only negligible degrees of degradation could be observed in the previous experiments in Chapter 3.1.4. Due to this incoherence, it was concluded that coagulation and/or sedimentation of the particles may happen, which is caused by a lack of stabilization of the NP dispersion. In general, there are two known stabilization mechanisms for particle dispersion. Electrostatic stabilization, which relies on electrostatic repulsion, and steric stabilization, which occurs when using nonionic surfactants. Measurements of the zeta potential revealed that values ranged in the slightly negative area, but close to zero. This observation was expected since no ionic surfactants were used for stabilization. Instead, PVA was used during the formulation of the NPs and was expected to remain adhered to the particles by absorption or by coprecipitation of the hydrophobic sections of the surfactant. Since the observations suggested that there was not sufficient stabilization, small quantities of PVA were added to the purified and diluted NP dispersion. Figure 3.12 shows the course of the normalized DLS scattering intensity over time for an unstabilized PPADK NP dispersion (no

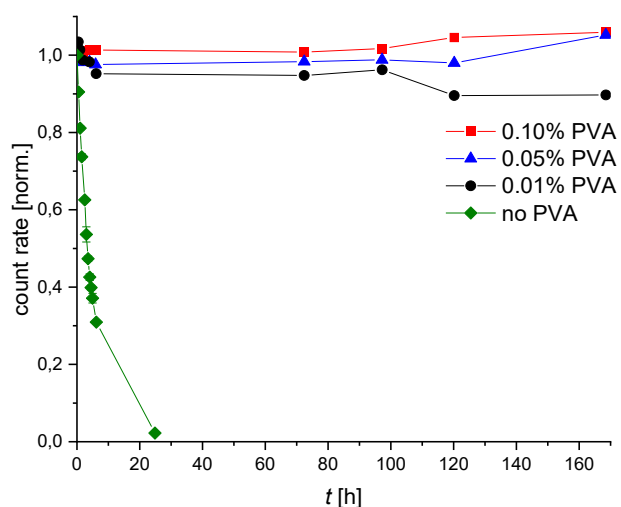PVA) and PVA stabilized dispersions with concentrations of 0.01 %, 0.05 % and 0.10 % of the surfactant.Figure 2.6

Figure 3.12 Normalized scattering intensity of purified PPADK NPs in citric-PBS buffered solution without any additional stabilization (green) and with addition of different concentrations of polyvinyl alcohol as a kinetic stabilizing agent.

The normalized count rate of the particles which are not additionally stabilized drops to almost zero in less than 24 h whereas all samples with added PVA remain relatively constant. Only in the case of 0.01 % PVA was a slight decrease observed over the entire duration of 160 h, although this is within the expected error range of the individual measurements. It can be concluded that during the thorough purification PVA gets completely washed out of the formulation so that no stabilization is provided. This was surprising as it was expected that PVAs adhesion to the particles surface would be too strong to get detached or might also be embedded into the particle structure during the formation. Since small quantities of PVA do not interfere with the DLS measurements, 0.05 % of PVA stabilizer were added to the NP dispersions for the further characterization of the degradation behavior.

The experiments in the following section were carried out by Leon Koch in the working group of Prof. Klaus Huber at the University of Paderborn. For further verification of the degradation process and to get insight into the particle constitution during the erosion of the particles, time resolved multi angle light scattering (TR-MALS) experiments were conducted of PPADK (**5**) NPs during the erosion in pH 3.0 citric buffered solution.

Freshly formulated nanoparticles were separated from the dispersing water by centrifugation and redispersed in a pH buffer as described in Chapter 3.1.4. The subsequent hydrolytic decomposition of the particles was monitored *via* the count rate of the scattered light. Figure 3.13 shows the signal intensity of the dynamic light scattering decreasing rapidly from 3 000 kcps over a few hours. After 25 h, the remaining scattering intensity was only 500 kcps. The progression appears to run asymptotically towards zero, so that it can be assumed that

no nanostructure remains after a sufficient period of time that could cause light scattering. This would be the case if the polymer had completely dissolved into its low-molecular components and no aggregates remain.
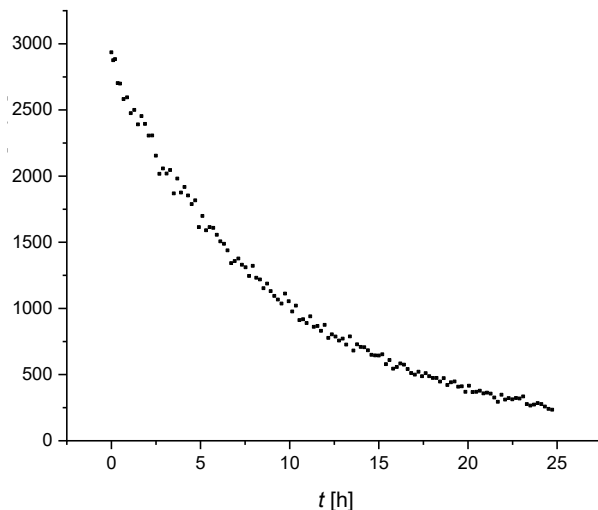

Figure 3.13 Scattering intensity (in kcps) of purified PPADK NPs in citric-PBS buffered solution at pH 3.0 over the duration of 25 h sows a strong decrease in intensity, which is assumed to be equivalent to a disintegration of the particle structure.

In the following experiment, the decrease in scattering intensity was measured in a multi-angle light scattering (MALS) setup from eight different angles over a period of 300 min. The plot of the data is shown in Figure 3.14.
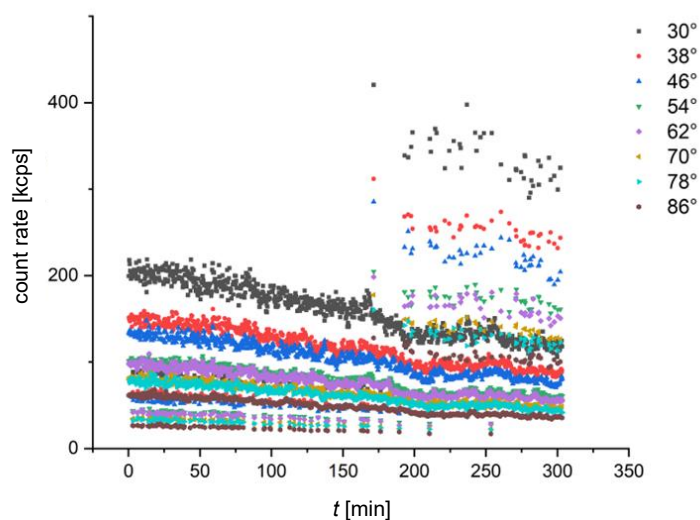
Figure 3.14 Plot of the raw data from an multi-angle light scattering (MALS) experiment, observing the scattering intensity of PPADK (**5**) NPs in pH 3.0 citric buffered solution from different angles between 30° and 86°.

It is noticeable that the lowest intensity was measured at large angles up to 86° and that this decreases slightly over the observed period. The smaller the angle, the greater the scattering intensity and the greater the absolute decrease in intensity over time. Larger particles scatter

light preferentially in the forward direction (smaller angles), while smaller particles tend to scatter light isotropically. The observation could therefore be interpreted that the particles become smaller in diameter during decomposition, thus reducing the proportion of forward scattering.

The data can be plotted in a variant of the ZIMM plot displayed in Figure 3.15, where $\sqrt{Kc/R}$ is plotted against q^2, where K is an experiment-specific constant, c is the mass concentration of the polymer, R is the RAYLEIGHT scattering intensity and q is the scattering vector.
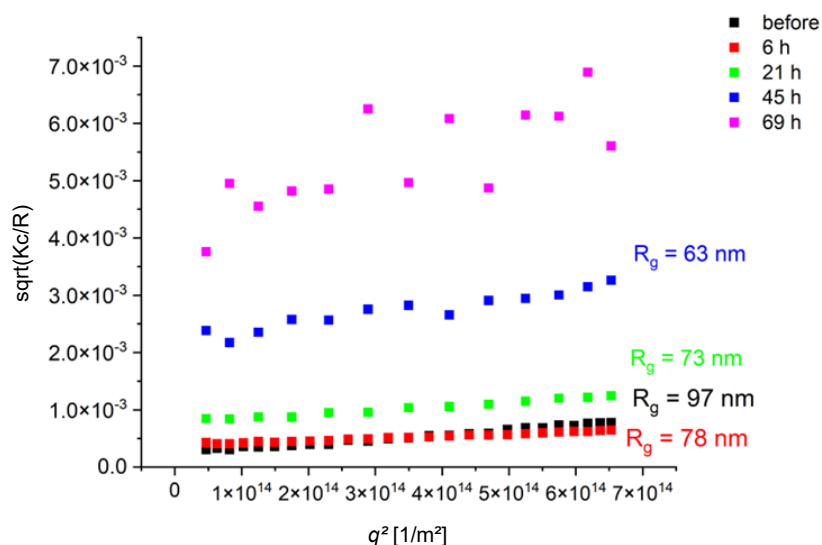

Figure 3.15 ZIMM-Plot of the pH responsive PPADK (**5**) NPs after different degradation times in pH 3.0 citric buffered solution.

The slope of a data set in this form of representation is proportional to the radius of gyration R_g. The determined radius of gyration at the beginning of the experiment was 96 nm, after 6 h 78 nm, after 21 h the measured radius was 73 nm and finally after 45 h it was still 63 nm. At the last data point after 69 h, the values scattered so strongly that an evaluation is no longer possible. The radius of gyration (R_g) and the hydrodynamic radius (R_h) are both measures of the size of a polymer in solution, but they are based on different physical principles. R_g describes the distribution of mass around the particle's center of gravity, while R_h represents the effective size of the solvated particle, which is influenced by its motion in solution. Although there is no direct relationship between R_g and R_h, both quantities in conjunction with the molecular weight can provide valuable information about the conformation and behavior of the polymer in solution. A comparison with the hydrodynamic radii determined is shown later in Table 3.2.

The weight-average molecular weight M_w can also be determined using the RAYLEIGH-equation and is included in the plot in the ZIMM-plot as part of the y-axis intercept. In this experiment, however, the molecular weight cannot be determined precisely because the refractive index dn/dc and the second virial coefficient A_2 are not known, and the exact concentration has not

been determined. In addition, the molecular weight of the polymer can only be determined for solvated polymer coils, whereas in the present experiment the material is a densely packed nanoparticle in which many polymer chains are aggregated together. To demonstrate that the analysis data shows a disintegration of the particles, the evaluation of the molecular weight was carried out using dummy values for *dn/dc* and A_2.
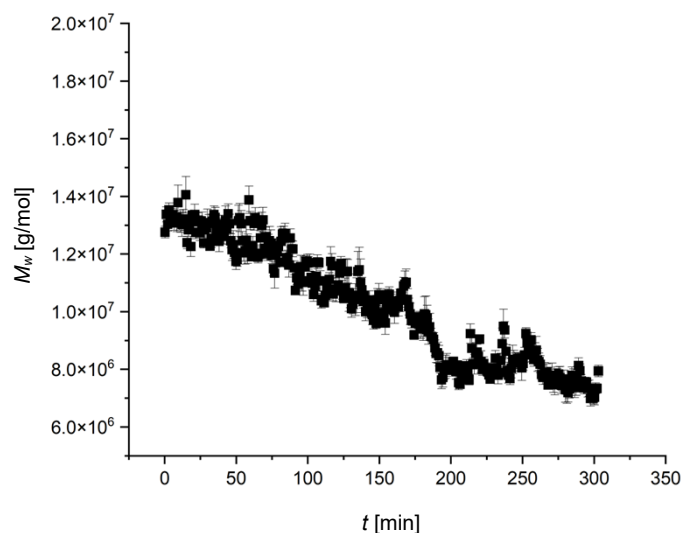

Figure 3.16 Decrease of the average molecular weight of an PPADK (**5**) nanoparticle during the degradation in pH 3.0 citric buffered solution.

Although the molecular weight cannot be determined with this evaluation, the relative change in the weight-average molecular weight of the particles can be determined. Figure 3.16 shows a strong decrease in the calculated molecular weight of the particles over the observed period of 300 min from around 40 % of the initial value of $1.4 \cdot 10^7$ to $0.8 \cdot 10^7$. Possible explanations for this observation are that oligomeric chains are released from the particle and pass into solution, which is rather unlikely due to the high hydrophobicity of the polymer, or that a degradation of the chemical polymer structure occurs and a degradation to low molecular weight components takes place.

Finally, information about the shape factor of the particles can be obtained from the experiment. The particle shape factor P_z is plotted as a function of the dimensionless quantity $q \cdot R_g$. A comparison with theoretical models allows conclusions to be drawn about the shape of the scattering particle.
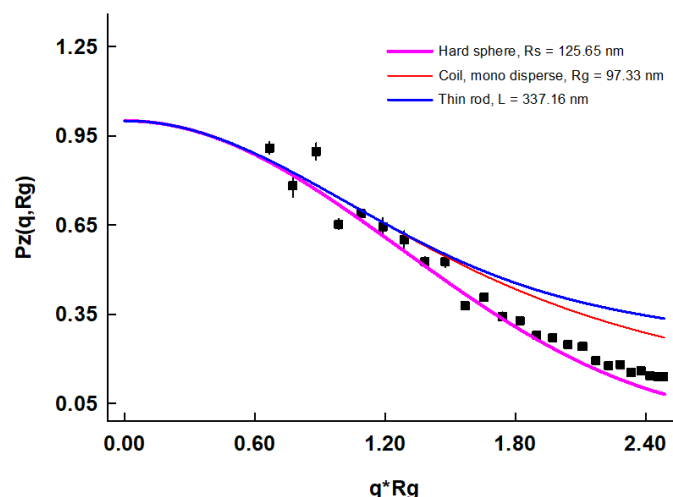
Figure 3.17 Plot of the formfactor (P_z) in dependence on the dimensionless quantity $q*R_g$ of PPADK NPs.

In Figure 3.17 at the low-angle range ($q \cdot R_g$ << 1), the value of P_z is close to one, which indicates homogeneous scattering with no recognizable internal structure and is typical for these experiments. In the high angle range ($q \cdot R_g$ >> 1), the value drops. The shape of the drop provides information about the internal structure and density distribution of the particle. The figure shows a comparison of the particle shape functions for monodisperse coils, hard spheres and thin rods. A comparison with the plot of ideal shaped particles shows a high degree of agreement with the model for hard spheres, which is why it can be assumed that the particles are also hard spheres. The perceptible deviation from the ideal model can be explained by the polydispersity of the particles.

The determined shape can be confirmed by another value. Table 3.2 shows the determined radii of gyration and the hydrodynamic radii of the particles after different times. The ratio R_g/R_h is a measure of the compactness of macromolecules and particles and provides information about their shape. This is typically 0.77 for monodisperse, compact spheres and is higher for more rod-shaped structures (> 1.7), flushed random coils (1.5) or hollow spheres (1.0). In all states of degradation, the ratio is between 0.64 and 0.75, which indicates the presence of hard spheres.

Table 3.2 Overview of the determined radius of gyration (R_g), hydrodynamic radius (R_h) and the ratio R_g/R_h, which is a measure of the compactness of the particles, of PPADK NPs in pH 3.0 citric buffered solution at the start of the experiment, after 6 h, 21 h and 45 h. After 69 h scattering intensity was too low for evaluation.

Sample	R_g in nm	R_h in nm	R_g/R_h
Reference	97	147.6	0.66
After 6 h	67	101.4	0.66
After 21 h	64	100.0	0.64
After 45 h	57	75.9	0.75
After 69 h	-	-	-

In summary, it was found that PPADK (**5**) NPs in pH 3.0 citric phosphate buffered solution show a continuous decrease in dynamic light scattering (DSL) over the entire observed period of 25 h. To better interpret this observation, MALS experiments were performed to show that the particles are present as hard spheres. Both the hydrodynamic radius R_h and the radius of gyration R_g showed a slight decrease, especially at the beginning of the observation period. The mass-average molecular weight (M_w) of a particle decreases over the observed period. Since the most plausible explanation for this is chemical hydrolysis of the polymer structure, it can be assumed that the decrease in scattering intensity is caused by chemical cleavage of the polymer. The observations establish DLS as a suitable method for investigating the degradation kinetics of the particles. Due to time constraints, no further investigations could be carried out using MALS. However, more extensive investigations with the light-responsive derivatives oNB PPADK (**6**), the investigation of irradiated samples and a broader spectrum of physiologically relevant pH values could provide information on the degradation behavior of the particles.

3.1.6 Kinetics of particle degradation studied *via* DLS

PPADK NPs and oNB PPADK NPs were incubated in PVA stabilized citric-PBS buffer at 37 °C and characterized *via* DLS in intervals. Figure 3.18 shows the normalized scattering intensity of PPADK NPs incubated in citric-PBS buffered solution at 37 °C without prior irradiation determined by dynamic light scattering (DLS) and in Figure 3.19 their irradiated counterparts are shown.

The normalized count rate of PPADK NPs remained nearly constant at pH 7.4 over the observed time frame of 24 h and dropped only to about 90 % of the initial intensity. Samples at pH 6.0 and 5.0 showed surprisingly low count rates even after only several hours of degradation. After 8 h of degradation, only about 27 % and 14 % of the initial scattering intensity remained, dropping even lower after 24 h. The samples incubated at pH 3.0 showed the fastest degradation, after 8 h of incubation, only 5 % scattering intensity remained, after 24 h no measurable scattering intensity could be detected. Upon irradiation with UV-light prior to incubation in citric-PBS buffers no alteration of the degradation behavior could be noted.
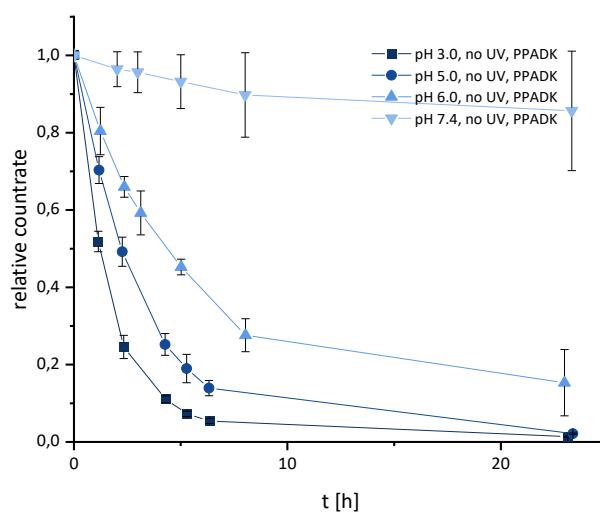
Figure 3.18 Normalized scattering intensity of PPADK (**5**) NPs incubated in citric-PBS buffered solution at 37 °C without irradiation determined by dynamic light scattering (DLS).
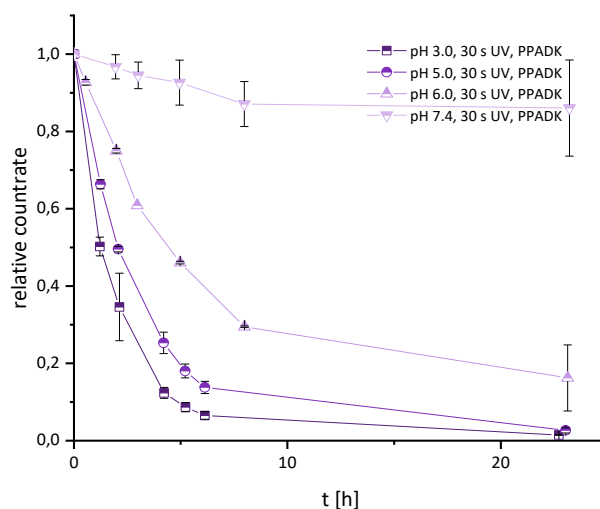

Figure 3.19 Normalized scattering intensity of PPADK NPs incubated in citric-PBS buffered solution at 37 °C with prior irradiation with UV-light determined by dynamic light scattering (DLS).

This strong correlation between the decline of the count rate and the pH value supports the assumption that scattering intensities are linked to the degree of degradation of polymeric nanoparticles. As pointed out in Chapter 3.1.4, the particle degradation is faster at lower pH values compared to higher pH values.

However, in comparison to the NMR degradation experiments carried out before, decline to half of the initial measured intensity occurred within a few hours at the DLS measurements, whereas in the NMR experiments weeks would be required to reach comparable decrease in the measured intensity. This deviation in the time scales could possibly be explained by the different experimental setups. The concentration in the NMR degradation experiments in Chapter 3.1.4 have a 500-fold higher concentration and no additional stabilization by addition

of PVA was applied. For this reason, coagulation could have occurred, and erosion of larger particles would take a longer time. Lastly the buffering systems were identical in their calculated pH value and osmolarity but differed in their composition and most notably the NMR degradation experiments were carried out in D_2O, which affects the acidity of the solution. However, the results also allow for further interpretation. The degradation of short-chain oligomers to low-molecular substances is perceived as progressive degradation in the NMR experiment. However, oligomers contribute significantly less to the scattering intensity than polymers with a higher molecular weight. Considering the different contributions of the degradation steps in the measured variables of the respective experiments, it appears that degradation involves a rapid decrease in molecular weight with only a small number of broken bonds. Accordingly, chain scission occurs mainly in the middle of the chain and not preferentially at the chain end.

The irradiation of the PPADK particles did not change the course of the scattering intensity. This is consistent with previous observations and shows that the PPADK NPs do not exhibit any change in degradation behavior when irradiated with UV-light.

The oNB PPADK NPs with and without irradiation were characterized in the same way. Figure 3.21 shows the normalized scattering intensities during the first 24 h of the particle degradation.
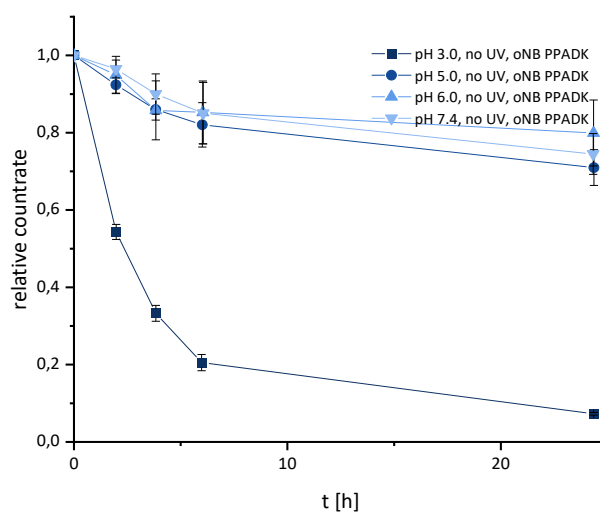
Figure 3.20 Normalized scattering intensity of oNB PPADK NPs incubated in citric-PBS buffered solution at 37 °C without irradiation determined by dynamic light scattering (DLS).
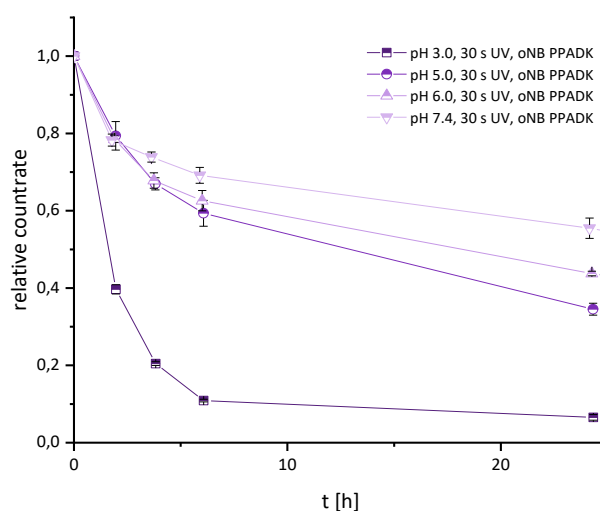

Figure 3.21 Normalized scattering intensity of oNB PPADK NPs incubated in citric-PBS buffered solution at 37 °C after irradiation with UV-light determined by dynamic light scattering (DLS).

In all cases the count rate decreases in the observed timeframe, which is recognized to be caused by particle degradation. The samples at pH 3.0 showed the fastest and most vigorous signs of erosion. However, in the case of the native particles at pH 5.0, 6.0 and 7.4 no significant differences in the erosion rate could be observed considering the relatively large measurement errors. The degradation of irradiated oNB PPADK particles occurred noticeably faster. After 8 h at pH 3.0, the normalized count rate was at 10 % while in case of the native particles 21 % of the initial intensity remained. After 24 h both, the native and the irradiated particles have almost fully degraded at pH 3.0. After 24 h at pH 5.0, 70 % of the initial intensity of the native particles remained, while irradiated particles only showed 34 % of the initial scattering intensity. This trend continues also for the other samples at pH 6.0 and 7.4. Since

52

particle degradation of the oNB PPADK particles did not progress very far after 24 h, the characterization of the degradation process was extended. In Chapter 0 the degradation curves over the extended duration of 50 h are shown. It becomes obvious that after an initial fast drop in the count rate, declining rates slowed down moderately but continued the trend they showed during the first 24 h of degradation. Scattering intensities, and therefore indications of particle integrity, declined in dependency of the pH value. Particles degraded faster the lower the pH value and prior irradiation with UV-light accelerated the degradation.

The results of the DLS measurements of the native and irradiated PPADK and oNB PPADK particles give a clear indication that the polyketals lacking the light-responsive group show no acceleration of the degradation while light-responsive polyketals degraded faster after a single irradiation event corresponding to their non-irradiated counterpart. Although degradation rates between the two polymer systems differed, the trends are clearly recognizable and agree with the results of the NMR degradation experiments.

3.1.7 oNB PPADK (**6**) based DDS *in vitro* applications

The research discussed in this chapter were conducted by Lisa Sophie Hönscheid at University of Münster in the working group of Prof. Dr. Klaus Langer and published in her master thesis: "*Entwickelung und Analyse von pH-responsiven nanopartikulären Arzneistoffträgersystemen*".[254] It was examined weather NPs could be formulated reproducibly in different procedures with varying polymer concentrations, oNB PPADK (**6**) and also a blend of the responsive polymer with PLGA. This was followed by embedding the model dye Lumogen® Red into a colloidal drug delivery system. Particularly promising formulations were examined cell biologically for their cytotoxic potential and cellular uptake.

First of all, colloidal drug delivery systems were developed from oNB PPADK (**6**) with concentrations of 2.5 mg/mL, 5 mg/mL and 10 mg/mL of polymer in THF, getting injected into 10 mL of 2 % PVA solution. Altering the polymer concentration allowed modification of the particle diameter and polydispersity. With the lower concentration yielding in smaller particles with lower polydispersities.

Table 3.3 Physicochemical properties of oNB PPADK nano particles with different formulations.

batch	$d_{h,app}$ in nm	PDI	ζ-potential in mV
10-oNB-PPADK-NP	285.7 ± 9.5	0,222 ± 0,013	- 4,0 ± 1,6
5-oNB-PPADK-NP	206.5 ± 6,0	0,127 ± 0,014	- 3,7 ± 0,2
2.5-oNB-PPADK-NP	173,6 ± 9,4	0,094 ± 0,010	- 3,3 ± 0,6

The spherical shape of the particles has been verified by atomic force microscopy (AFM) as

shown in Figure 3.22. The measurement shows spherical shapes with an average particle diameter of approximately 200 nm.
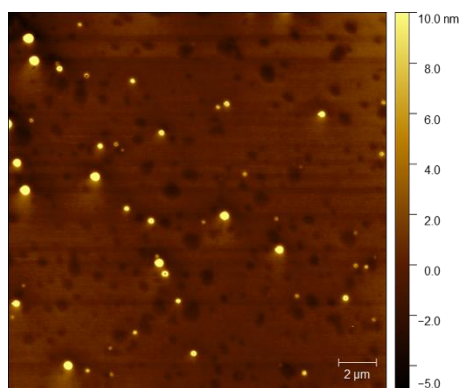

Figure 3.22 Visualization of oNB PPADK NPs measured by AFM to confirm size and shape of the nanoparticles.

The degradation of the different nanoparticle formulations has been characterized by DLS measurements during degradation in citric PBS buffer in the same setup as shown in Chapter 3.1.6. Results showed that the degradation behavior described previously could be reproduced. Further, slight differences in degradation speed between the different formulations could be observed. The 10- and 5-oNB-PPADK-NPs did not reveal any significant differences in degradation tempo, but the 2.5-oNB-PPADK-NPs degraded significantly faster at pH 3.0, which might be due to the lower hydrodynamic diameter. Since the smaller particles showed a faster degradation, this formulation method was chosen for further examinations.

Blend of the stimuli-responsive oNB-PPADK and PLGA have been formulated in two different compositions, one with 75 % oNB-PPADK and 25 % PLGA and vice versa. Both had smaller particle diameters compared to the pure oNB-PPADK NPs and lower zeta potentials of - 10 mV and - 9 mV respectively. The oNB-PPADK[25]-PLGA[75]-NPs did not show a pH dependent decrease of the count rate, for this reason the oNB-PPADK[75]-PLGA[25]-NPs were chosen for further formulations, since they showed comparable degradation kinetics to the 2.5-oNB-PPADK-NPs while having superior physicochemical properties.

Lumogen® Red (LR) was successfully loaded into 2.5-oNB-PPADK-NPs and oNB-PPADK[75]-PLGA[25]-NPs as well as in pure PLGA-NPs as non-responsive comparison sample. Their physicochemical properties and degradation behavior were characterized and subsequently used in *in vitro* cell culture studies. Loading the nanoparticles with the fluorescence dye had an influence on the hydrodynamic diameter. The determined diameter of oNB-PPADK[75]-PLGA[25]-NPs went down from 167 nm to 134 nm. Diameter of 2.5-oNB-PPADK-NPs went down from 173 nm to 164 nm, which is a less significant change. However, the diameter of LR loaded PLGA nanoparticles was 83 nm compared to 113 nm in case of unloaded particles. During incubation in aqueous buffered solutions the degradation rate of the particles was determined by DLS measurements. No significant differences compared to the unloaded NPs could be observed except for the LR loaded oNB-PPADK[75]-PLGA[25]-NPs, which seem to degrade faster at

pH 4.5 and 3.0. After 6 h of degradation the unloaded NPs had 30 % of remaining scattering intensity while the LR-loaded, smaller NPs had only 10 % of their initials scattering intensity left, which might be due to the smaller particle size.

To determine the biological safety of the responsive oNB-PPADK (**6**), a WST-1-assay (water soluble tetrazolium – assay) and an NRT-assay (*Neutralrot* assay) with exposure of the degraded polymer towards MCF-7 Cells, which is a cell-line of breast cancer cells. The polymer was degraded in an acidic environment and neutralized subsequently. MCF-7 cells were incubated with different concentrations of the degraded polymer and the cell viability was tested as shown in Figure 3.23.
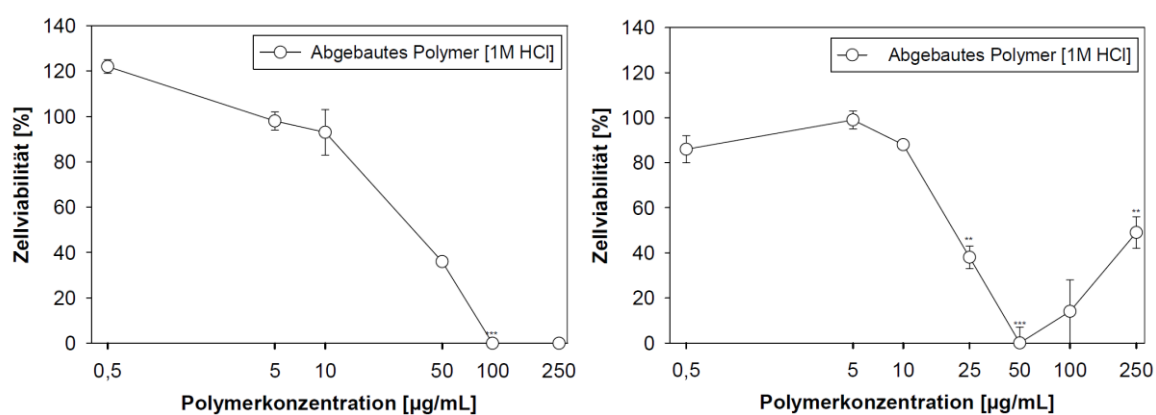

Figure 3.23 Cytotoxic potential in dependence the concentration of the degraded polymer oNB-PPADK determined in a WST-assay (left) and an NRT-assay (right) after 24 h of incubation. Reprinted with permission from ref. [254]

Both results show high cell viability at low concentrations of the polymer debris and decline of cell viability at higher concentrations. The WST-assay shows an effective concentration (EC$_{50}$) value of 30 µg/mL, which is the concentration where 50 % of the cells get effected by the substance under investigation. The NRT-assay shows an EC$_{50}$ of 22 µg/mL. However, detected cell viability started rising again at concentrations higher than 50 µg/mL, which could not be explained. It cannot be stated beyond doubt that polymer **6** was completely neutralized after the degradation step. Residual acidity could have strongly interfered with the results and decreased cell viability significantly, which could explain this surprisingly high cytotoxicity of the oNB-PPADK debris. The NRT-assay depends on NRT (*Neutralrot*) as a pH-indicator with pK$_s$ 5.89, which is yellow and permeable to membranes in its neutral form and enters the lysosome of vital cells to then get protonated by the acid environment and shows its characteristic color. This could also explain the seemingly increase of cell viability at higher concentrations of the toxicant, because residual acidity from polymer degradation would cause a change of color of the *Neutralrot*.

To further determine information about possible toxicologic effects, the Lumogen® Red (LR) loaded nanoparticles (LR)-2.5-oNB-PPADK-NP, (LR)-oNB-PPADK[75]-PLGA[25]-NP and (LR)-PLGA-NP were incubated with MCF-7 cells and cell viability was tested in an WST-assay and an NRT-assay again.
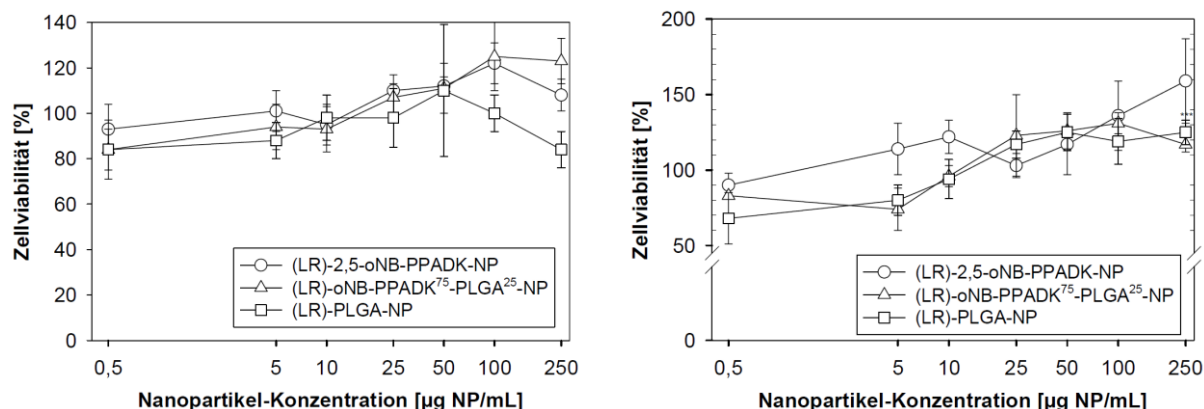

Figure 3.24 Cytotoxic potential in dependence the concentration of three different Lumogen® Red (LR) loaded nanoparticle formulations determined in a WST-assay (left) and an NRT-assay (right) after 24 h of incubation. Reprinted with permission from ref. [254]

In both experiments there was no cell toxicological effect on the MCF-7 cells observed up to the highest concentration of 250 µm/mL. These results suggest that the nanoparticle formulations are not cytotoxic and could be safe for application *in vivo*.

The cell interaction with the LR loaded drug delivery systems was characterized by live-cell imaging and the intracellular enrichment was determined using HPLC analysis. Adherent MCF-7 cells were incubated with 2 nmol/well LR loaded nanoparticles while the total red object area was measured. After an initialization phase where the total red object area raised, it remained constant during the whole 24 h of incubation. Subsequently the supernatant particles were removed, and the cells were washed with PBS. After the washing step, no total red object area could be observed. This indicates that during the incubation period none of the drug delivery systems were taken up by the MCF-7 cells. In addition, the intracellular enrichment of LR in the MCF-7 cells was determined by HPLC-FLD (high performance liquid chromatography with fluorescence detector) after prior cell lysis. Of the initial 2 nmol/well, the cells incubated with (LR)-2.5-oNB-PPADK-NP had a measured uptake into the cells of 0.0025 nmol/well of Lumogen® Red, the cells incubated with (LR)-oNB-PPADK[75]-PLGA[25]-NP had 0.0016 nmol/well and cells incubated with (LR)-PLGA-NP showed an uptake of 0,0014 nmol/well of the model drug. In all cases the measured concentration of LR that was taken up into the cells was by factor 1 000 lower than the initial concentration of LR. The results of the HPLC analysis coincided with the observations of the live cell imaging, so that it can be assumed that all nanoparticles loaded with active substances were not taken up into the cells.

Lastly, the cellular uptake and distribution inside of the cells should be visualized by fluorescence microscopy, which is shown in Table 3.4.

Table 3.4 Fluorescence microscopy images of MCF-7 cells after 48-hour incubation with (LR)-2.5-oNB-PPADK-NP, (LR)-oNB-PPADK75-PLGA25-NP and (LR)-PLGA-NP without NP degradation (left column) and after NPs were degraded in 1M HCl (right column). Incubation was carried out according to a concentration of 2 nmol Lumogen® Red (LR). LR is characterized by a red autofluorescence, lysosomes, cell nuclei and membranes are visualized by a green fluorescence after staining with 4',6-diamidino-2-phenylindole (DAPI) or Bio Tracker® 400 Blue Cytoplasmatic Membrane Dye.
Reprinted with permission from ref. [254]
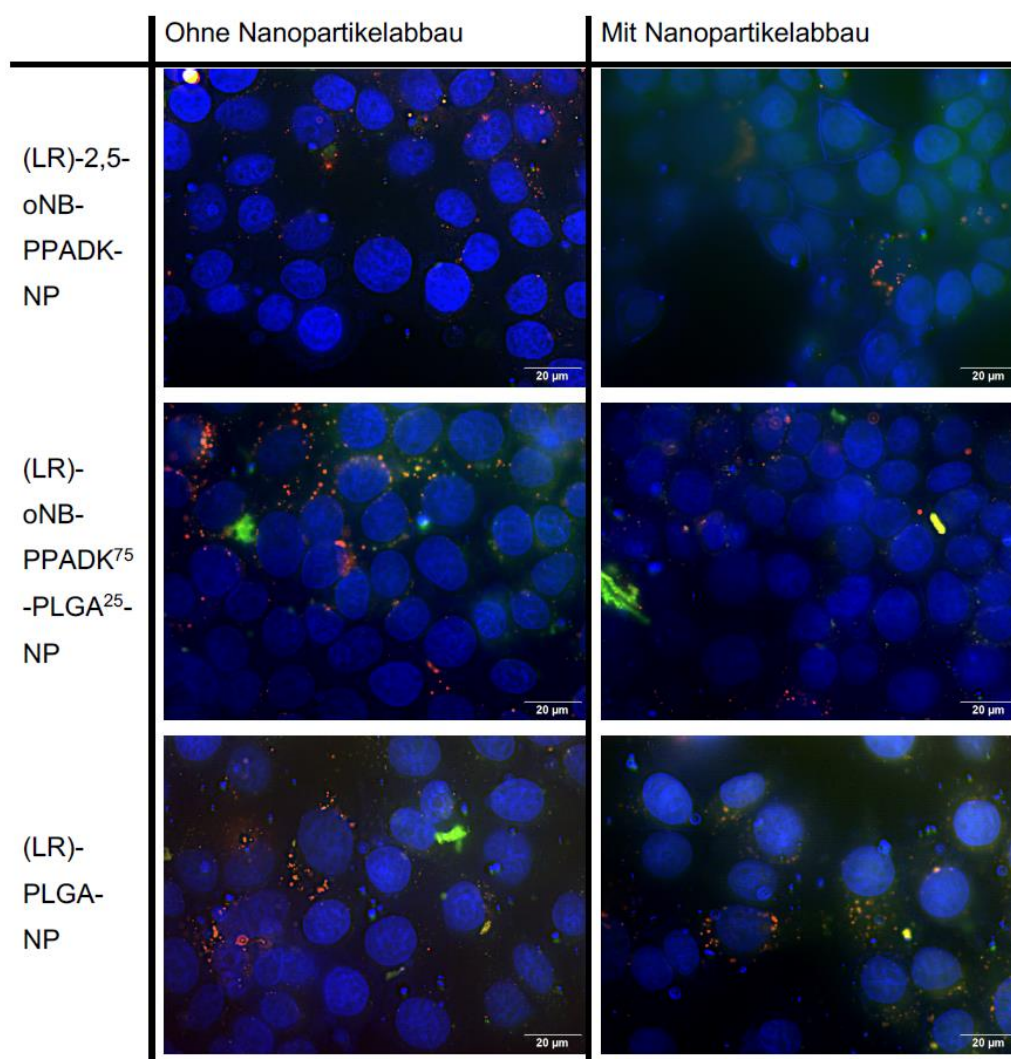
The left column in Table 3.4 shows the fluorescence microscopy images of MCF-7 cells, that have been incubated with Lumongen® Red carrying nanoparticles. The right column shows the cells incubated with nanoparticle formulations previously treated for 24 h with 1 M HCl. Treatment with HCl is expected to dissolve the pH responsive oNB-PPADK nanocarriers and as a reference the (LR)-PLGA-NPs, which are not expected to change upon treatment with acid. The LR can be seen as a red color in the images. Some cell compartments were made visible by staining, the cell nuclei and membranes can be recognized in blue by the use of Bio Tracker® 400 Blue Cytoplasmatic Membrane Dye. The green fluorescence dye DAPI (4',6-diamidino-2-phenylindole) is supposed to stain lysosomes, cell nuclei and membranes, but this stain did

not work correctly, resulting in strong aggregations in some areas. Nevertheless, several conclusions can be drawn from the cell imaging observations.

In the images with intact nanoparticle formulations (left column), the cell nuclei are clearly visible as blue areas. Punctual signals indicating structures that accumulated LR were detected in all images. However, the observed circular shapes are not the nanoparticles themselves, which are not observable at this resolution. Colocalization with lysosomes (green fluorescence) was partially confirmed. The amount of particles taken up by the cells can be classified as fairly low and they mainly accumulate around the cell nuclei. Intracellular accumulation of (LR)-2,5-oNB-PPADK-NP, (LR)-oNB-PPADK^{75}-PLGA^{25}-NP and (LR)-PLGA-NP was thus visually confirmed.

Fluorescence images of the same formulations were also taken, but the particles were treated with 1 M HCl for 24 h before incubation (right column). The (LR)-2,5-oNB-PPADK-NP and (LR)-oNB-PPADK^{75}-PLGA^{25}-NP showed a lower intracellular accumulation compared to the formulations without prior degradation of the particles. This was in line with the expected result, as treatment with hydrochloric acid was expected to cause particle decomposition, resulting in less NP. In the case of (LR)-PLGA-NP, the formulation that was also treated with 1 M HCl and then neutralized with 1 M NaOH hardly showed any difference to the formulation without incubation. This was also consistent with the assumption that the matrix polymer PLGA, of which the particles are made, has only very low sensitivity towards low pH values and therefore the NPs should not disintegrate when incubated with diluted HCl. The images after 48 h from Table 3.4 showed the same observations that could already be made after 24 h of incubation. However, the amount of the red areas was more pronounced after 48 h, so that it can be assumed that the cells continued to accumulate nanoparticles over a longer period of time.

In summary, it can be said that the development of a pH-responsive NP system was achieved with the polymer oNB-PPADK. It could be shown that the concentration used and the mixing ratios of oNB-PPADK and PLGA led to different hydrodynamic diameters and are decisive for the pH-dependent decomposition. All NP systems tested showed no cytotoxic effects and were found to a small extent in the lysosomes of MCF-7 cells after incubation.

3.1.8 Conclusions

The synthesis and characterization of the polyketal PPADK (**5**) and the oNB diol (**2**) was successfully carried out. The novel light- and pH-responsive oNB PPADK (**6**) was synthesized with 10 % of oNB bearing monomer units, which were copolymerized statistically. The developed polymer was characterized by NMR spectroscopy, SEC and DSC measurements. The

added light-responsiveness of the oNB PPADK (**6**) was shown in comparison with the PPADK polymer by irradiation and characterization of irradiated and non-irradiated samples by SEC and UV-VIS spectroscopy. While PPADK polymer showed no sign of photocleavage, oNB PPADK underwent a photoreaction that caused distinct degradation of the polymer. Well low disperse nanoparticles with hydrodynamic diameters ranging from 160 nm to 190 nm could be reproducibly formulated by nanoprecipitation from THF into PVA-solution easily with a yield of 72 %. Degradation properties of the formulated nanoparticles were characterized by NMR spectroscopy and DLS measurements. With both methods, it could be shown that even a short irradiation of the particle dispersion can significantly accelerate the degradation rate. This acceleration was only achieved by incorporation of an oNB functionality into the polymeric backbone. Based on the NMR data an estimate could be made that an acceleration of the hydrolyzation reaction of the ketal functionalities by the factor 34 could be achieved.

It was demonstrated by cooperation partners from University of Münster, that stimuli-responsive nanoparticles could be formulated with PLGA blended into the formulation, that were capable of bearing the model drug Lumogen® Red. The formulated drug delivery systems did not show any toxicity towards living MCF-7 cells and it was demonstrated that in principle the formulation gets taken up into the cell, however the determined cellular uptake into the MCF-7 cells was rather low.[254]

To summarize, a dually stimuli responsive polymeric nanoparticle system was developed, that offers the unique property to degrade faster in aqueous environment after a short irradiation. Such a mechanism enables light with its high spatiotemporal precision to be used as a trigger for the release of active ingredients from polymer drug delivery systems and avoids the extended irradiation times, that are required in solely light-responsive drug delivery systems. To gain a deeper understanding of the mechanism, this system could be transferred to other hydrolytically cleavable particulate systems. In principle, all polymer systems that work with diols as building blocks would be suitable in the first instance. PLGA polymers, in which diols can be used as initiators, could also be of particular interest. Furthermore, the concept could also be transferred to thioketals such as PPADT.[255]

3.2 Light degradable oNB polyurethanes

Photodegradable polymeric nanoparticles, which release their cargo by irradiation with light show high potential for application in nanomedicine. For their development a crucial factor is the hydrophilic/hydrophobic balance which influences the release of the cargo but also the disassembly, removal and extraction of remaining debris of the particles. Polyurethanes containing hydrophilic building blocks should be synthesized to provide delivery vehicles with high biocompatibility and easy clearance from the body.[140,256,257] The particles degradation behavior in aqueous dispersions should be characterized and studied.

3.2.1 Synthesis of low molecular compounds and light-responsive polymers

To achieve light cleavable polyurethane, at first a light-responsive monomer must be synthesized. Chromophore **9** was chosen as a cleavable light-responsive group. It offers two primary alcohol groups to form polyurethanes in an AA/BB type polyaddition with isocyanates. The phenol-ether as an electron donating group causes a bathochromic shift of the absorption maximum to 310 nm and it can be easily synthesized in a two-step process with good yields. The synthesis is based on literature known procedures.[233,251,258]

For the two-step synthesis 4-Nitrobenzaldehyde (**7**) was deprotonated by addition of potassium carbonate and etherification with bromoethanol to the intermediate aldehyde **8**. The structure of the crude product was confirmed by ^{1}H NMR spectroscopy and the purity was sufficient to be utilized as educt in the next step of the synthesis without further purification. Reduction of the aldehyde functional group was carried out with sodium borohydride in methanol and subsequent recrystallization in chloroform. The oNB diol **9** was isolated as colorless needles in a yield 70 % over two steps. Identity and purity of the product were confirmed by NMR spectroscopy and the absorption spectrum shows a maximum at 310 nm as described in the literature. However, in insufficient purified or aged batches a yellowish discoloration may appear. This is presumably due to photo-isomerized side products, which can easily be removed by recrystallization again.
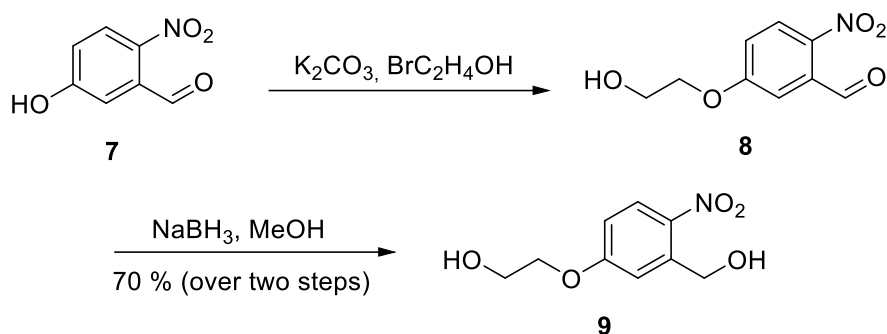
Scheme 3.4 Two-step synthesis of oNB diol **9** starting from commercially available 4-Nitrobenzaldehyde (**7**) *via* the intermediate aldehyde **8** in a two-step protocol.

To modify hydrophilicity of the final polymer, hydrophilic segments should be incorporated into the polymer backbone. The PEG-graft-comonomer Linker **12** is a diol with a pendent triethylenglycol monomethyl ether and was chosen to be copolymerized to increase the hydrophilicity. The synthesis was carried out according a procedure of SANTRA *et al.* and is shown in Scheme 3.5.[259]
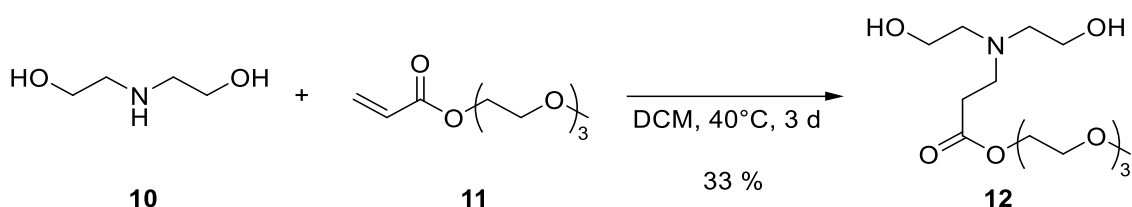
Scheme 3.5 Synthesis of PEG-graft-comonomer (**12**) from addition of the acryl ester **11** to diethanolamine (**12**) according to SANTRA *et al.*[259]

Diethanolamine (**10**) was stirred with acryl-TEG (**11**) for three days. Crude NMR data shows a conversion of 85 % but the majority of product gets lost during the workup and purification procedure. Since amines react preferentially with isocyanates compared to alcohols, even small quantities of diethanolamine (**10**) would cause crosslinking in the polymerization step. Due to this the challenging workup of the highly water-soluble diol **12** was carried out thoroughly, lowering the yield to 33 %. The structure was confirmed by NMR spectroscopy with a very particular attention to the absence of residual amine **10**.

In Scheme 3.6 the polymerization of diol **9** with the amino acid based diisocanate LDI (**13**) towards the light-responsive polyurethane lrPU 1 (**14**) is displayed. DBTL was used as a catalyst, it forms complexes with hydroxyl compounds as well as with isocyanate groups and therefore catalyzes the polyaddition reaction while preventing biuret and allophanate formation.[30,31] The efficient catalysis allowed to perform polymerization at mild conditions of 50 °C. In initial trials THF was evaluated as a solvent but due to solubility incompatibilities and high volatility at elevated temperatures, DMF was chosen as a solvent for all polymerization systems.
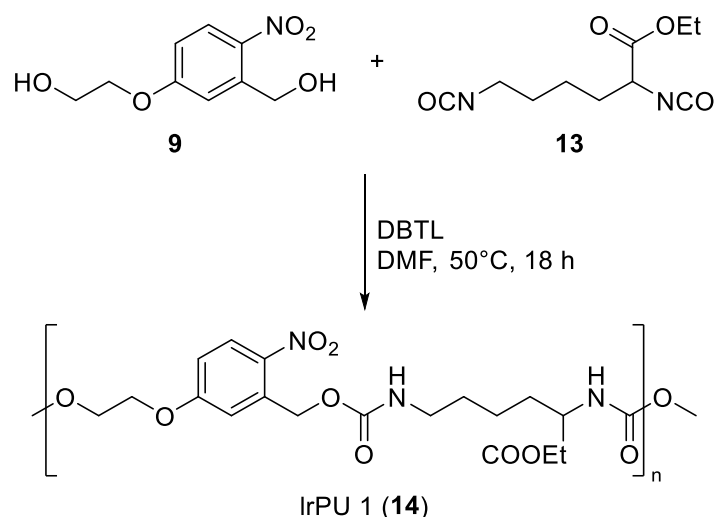
Scheme 3.6 Polymerization of oNB diol **9** and the diisocyanate **13** towards the light-responsive polyurethane 1 (**14**).

As introduced in Chapter 2.1 the molecular weight of the resulting polymer shows a high dependency on the molar ratio and the conversion of the monomers. To maintain a certain degree of control over the molecular weight and terminal groups of the polymer, a slight surplus of diisocyanate of 1.05 equivalents was chosen. According to the CAROTHERS-Equation shown in Figure 2.2, this molar ratio would lead to a molecular weight of 19 500 g/mol at 100 % conversion. To emphasize the strong dependency on the conversion, a conversion of 97 % would lead to a molecular weight of 9 000 g/mol. In previous works, this molar ratio also has proven to offer good control over terminal groups as well as providing molecular weights sufficient for drug delivery purposes.[137]

Molecular weights of isolated batches ranged around 5 000 and 15 000 g/mol, all molecular weight and yields are listed in Table 3.5. In one of the initial polymerizations, samples after 2 h, 3 h, 4 h and after 16 h were taken and analyzed *via* SEC. The results are shown in Figure 3.25. Opposing the idealized, schematic sketch in Figure 2.1. the molecular weight of the polyurethane was rising rapidly during the initial 2 h of the synthesis. After 3 h and 4 h molecular weight kept rising but the rate of molecular weight increase was diminishing. Overnight the reaction mass was kept stirring at 50 °C and only a slight increase of molecular weight was observed.
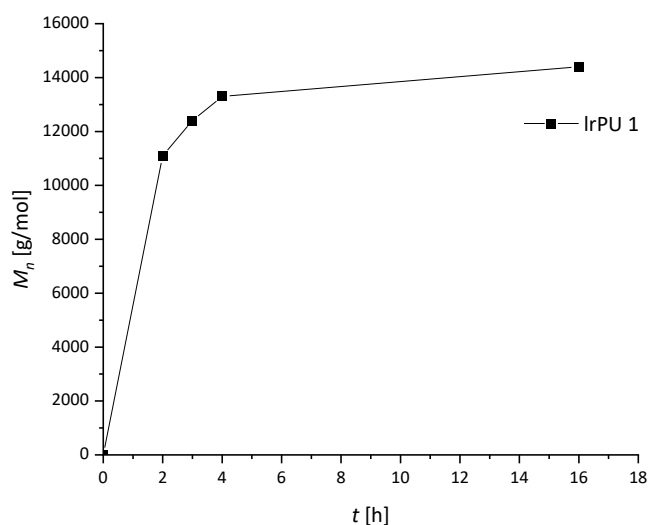
*Figure 3.25* Molecular weight of the polymerization of lrPU 1 after 2 h, 3 h, 4 h and 16 h.

The deviation from the ideal behavior may occur due to lower mobility of the terminal isocyanate groups compared to monomeric LDI (**13**) and coiling of the polymer chains. Probably a similar curve as shown in Figure 2.1 could be observed during the initial 2 h of the synthesis. To terminate the polymerization, methanol was added to form methoxy groups as terminal groups of the polymer chain. The structure of the final polymer was confirmed by ^{1}H-NMR spectroscopy. UV-VIS spectroscopic analysis of the polymer showed absorption maximum at 310 nm, indicating a successful incorporation of the photolabile group into the polymeric backbone. DSC analysis of the polymer indicated a glass transition temperature (T_g) of 65 °C.

Table 3.5 Molecular weights, polydispersities and yields of the different synthesized batches of the light-responsive polyurethanes lrPU 1.

Batch	M_n	Đ	yield
1	13 700	1.73	74 %
2	14 600	1.51	52 %
3	15 500	1.58	50 %
4	5 000	1.42	72 %
5	4 000	1.64	82 %

Two derivates of the lrPU 1 have been synthesized by copolymerization with PEG 200, and the hydrophilic linker **12**. The synthesis of lrPU 2 is shown in Scheme 3.7. Prior to polymerization the PEG 200 has to be dried in high vacuum. The molar ratio of the two diols was 1:1 and the diisocyanate LDI (**13**) was added in 1.05 eq.
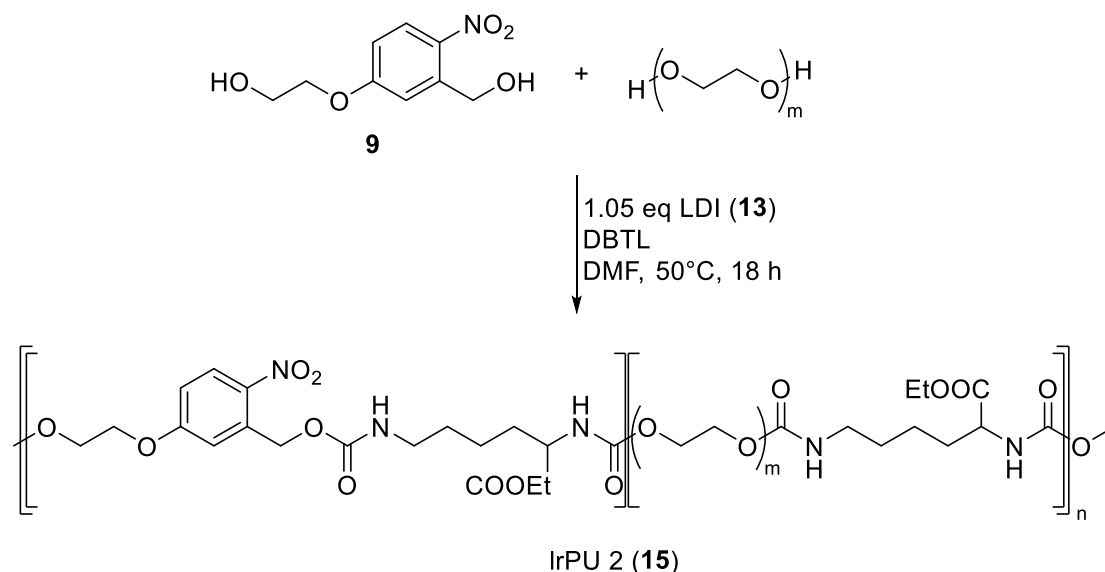
Scheme 3.7 Synthesis of lrPU 2 by copolymerization of oNB diol **9** and PEG 200 in equal equivalents with the diiscoyanate LDI (**13**).

Reaction was terminated by addition of MeOH, and the final polymer was precipitated into cold methanol and isolated in a yield of 49 - 71 %. Identity of the lrPU 2 was confirmed by ^{1}H-NMR and UV-VIS spectroscopy and SEC analysis. The polymerized ratio of the two diols could be estimated based on the ^{1}H-NMR data. The two benzylic protons [9]CH_2 at 5.36 ppm showed a relative integral of 0.776 and the [22]CH_2-[23]CH_2 group of the PEG 200 at 3.50 ppm shows a relative integral of 3.665. Under the assumption that PEG 200 has an average degree of polymerization of 2.78, one PEG 200 block has an average of 11.1 C-H protons. This leads to PEG 200:oNB **9** ratio of 1.18:1, which is close to the targeted ratio of 1:1, considering PEG is a technical product with only limited reliability of its molecular weight and the inherent error of NMR spectroscopy. DSC analysis of the polymer indicated a glass transition temperature of 23 °C. The reaction was carried out several times, the molecular weights, polydispersities and yields are listed in Table 3.6.

Table 3.6 Molecular weights, polydispersities and yields of the different synthesized batches of the light-responsive polyurethanes lrPU 2.

Batch	M_n	Đ	yield
1	9 400	1.64	49 %
2	7 800	1.57	71 %
3	3 100	1.38	70 %
4	8 400	1.69	59 %

The third light-responsive polymer lrPU 3 was synthesized by the copolymerization of a 1:1 ratio of oNB diol **9** and the hydrophilic linker **11** with 1.05 eq of LDI (**16**). As shown in Scheme

3.8 reaction parameters did not deviate from the other two polymerizations. In the first attempt, gel formation was observed. This was explained by trace impurities of diethanolamine (**10**), which were observed in the NMR spectrum of the educt on close inspection. The precipitation of lrPU 3 had to be carried out in diethylether, since its solubility in methanol at 0 °C was too high. At lower temperatures precipitation of the polymer could be accomplished, but impurities also precipitated, and no purification took place.
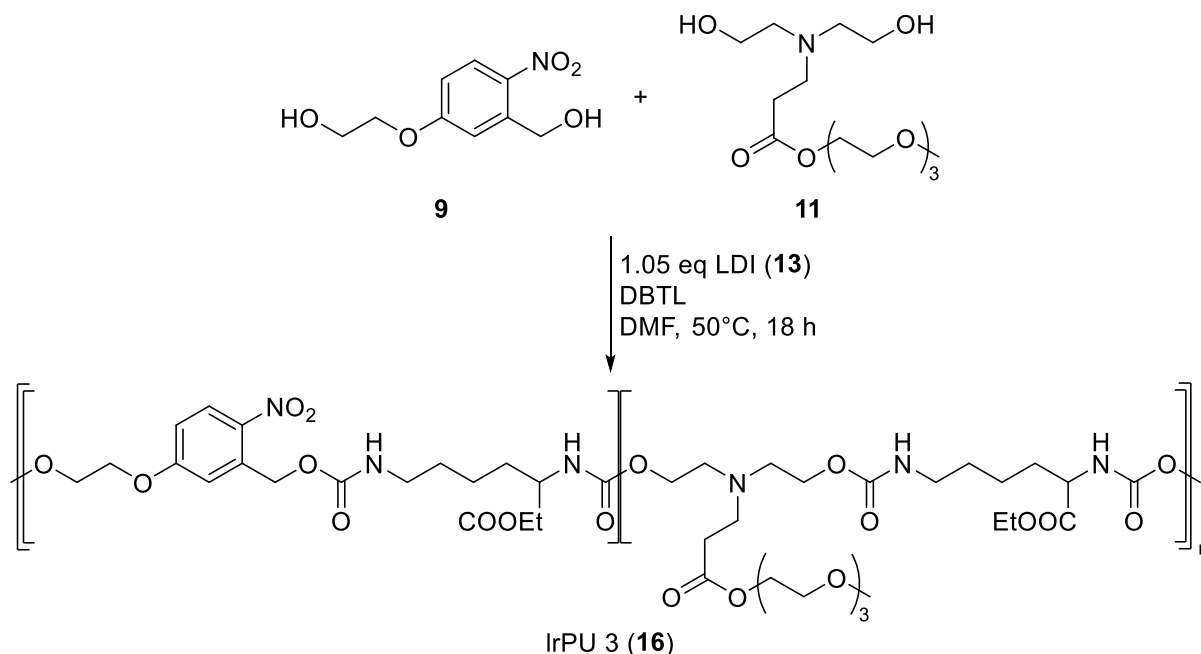
Scheme 3.8 Synthesis of lrPU 3 by copolymerization of oNB diol **9** and hydrophilic linker **11**
in equal equivalents with the diisocyanate LDI (**13**).

The successful incorporation of the hydrophilic linker was confirmed by NMR spectroscopy. The molar ratio of the two copolymerized diols **9** and **11** could be estimated based on the NMR spectral data. The comparison of the benzylic $^9CH_2$ of the oNB monomer **9** at 5.36 ppm to the $^{25}CH_2$ in α-position of the carboxylic group of the linker **11** at 2.41 ppm shows a ratio of the relative integrals of 1.08:1. Within the expected divergence, this corresponds to the targeted ratio of 1:1. The polymerization was carried out three times. The yields ranged from 56 % to 77 % and are listed in Table 3.7 with their respective molecular weight and polydispersity. The UV-VIS absorption maximum was identified at 310 nm, proving that the oNB functionalized monomer has been incorporated into the polymer backbone.

Table 3.7 Molecular weights, polydispersities and yields of the different synthesized batches of the light-responsive polyurethanes lrPU 3.

Batch	M_n	Đ	yield
1	11 200	2.13	77 %
2	12 800	2.34	65 %
3	16 000	2.71	56 %

Three polyurethanes containing oNB were synthesized through step-growth polymerization using the lysine-based diisocyanate LDI. The precise overlay of the UV-VIS and RI detector elution curves in SEC analysis revealed uniform copolymerization of the oNB monomer across all chain lengths. The incorporation of the hydrophilic linkers in the polyurethanes, lrPU 2 and lrPU 3 caused a significant decrease of the glass transition temperature compared to lrPU 1. However, it was observed that the step-growth polymerization technique used in this study provided limited control over the molecular weight of the resulting polymers.

3.2.2 Degradation of polymer

The intended release mechanism of the drug delivery systems used here is based on stimuli-responsive degradation of the polymeric backbone. In order to confirm the responsiveness to the stimulus UV-light, the photoisomerization of the oNB group is investigated below using UV-VIS spectroscopy and the degradation of the polymer using SEC.
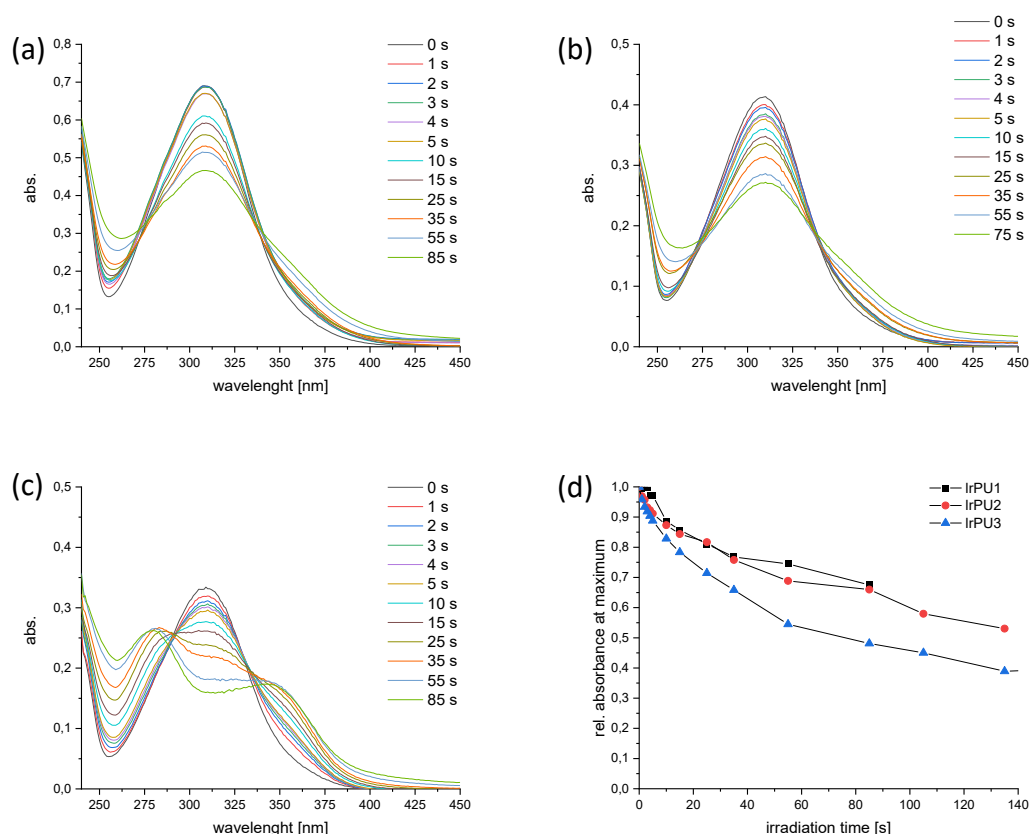

Figure 3.26 UV-VIS spectral data of 40 mg/L solutions of lrPU 1 (a), lrPU 2 (b) and lrPU 3 (c) in chloroform upon irradiation with 300 mW/cm² UV-light and a plot of the normalized absorbances at their maximum (310 nm).

Before irradiation (0 s), all three polymers show a global maximum at 310 nm, which originates from the oNB functionality. The initial absorbance of lrPU 1 at 310 nm is higher compared to its hydrophilic counterparts (Figure 3.26 (a-c)). This corresponds to the higher

oNB concentration at the same mass concentrations of the polymer. Upon irradiation, in all three samples, the absorbance at 310 nm decreased significantly. In the case of lrPU 1 and lrPU 2, the absorbance at 260 nm as well as the absorbance in a broad area from 350 – 450 nm increased slightly. This general course aligns with previous observations of oNB photo-isomerization.[251] Interestingly the course of the absorbance of lrPU 3 differs from the other samples. The absorbance at 310 nm showed a slightly faster decline than in the other polymers and the absorbance at 280 nm and 345 nm showed a rapid increase and formed local maxima after 30 s of irradiation. Since the increasing absorbance arises from the photo-isomerization product, this observation may indicate that the decomposition of the exited state may take another reaction pathway. Since most of the polymeric backbone of lrPU 2 and lrPU 3 were similar, the most likely candidate would be a tertiary amino group. Further investigation of the exact mechanism could offer insightful information into the mechanism of the photo-isomerization and probably an alternative decay of the *aci*-nitro compound.

To confirm that the photoisomerization of the oNB groups lead to a degradation of the polymeric backbone, SEC studies of irradiated polymers had been carried out. Figure 3.27 shows the normalized average number molecular weights es of the light-responsive polymers, irradiated for 0 – 240 s with UV-light in an intensity of 300 mW/cm².
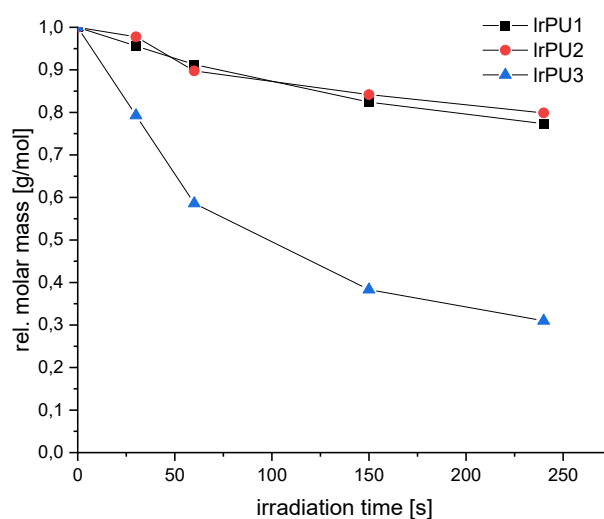

Figure 3.27 Normalized average *number molecular weights of* three light-degradable polyurethanes measured by THF-SEC (PS-calibration) after UV-irradiation for 0 – 240 s.

lrPU 1 and lrPU 2 showed the same relative decline of the number average molecular weight, although their concentration of oNB groups differs from each other. The polymer lrPU 3 on the other hand showed a much steeper decrease of the relative number average molecular weight compared to the other two polymers.

3.2.3 Formation and degradation of nanoparticles

Nanoparticles were formed by nanoprecipitation of the light-degradable polyurethanes into aqueous PVA solution. 10 mg of polymers lrPU 1, lrPU 2 and lrPU 3 were dissolved in DMSO and rapidly injected through a submerged canular into 10 mL of 2 % PVA solution. NP formation was confirmed by a DLS measurement of highly diluted crude NPs. For purification the crude dispersion centrifuged at 12 000 RCF for 10 min, supernatant was decanted off and the centrifugate was redispersed in water. In a typical NP formation procedure, the purification step was carried out three times. Batches with prolonged centrifugation times resulted in NP dispersions with a higher count rate in the DLS measurement, hence a higher yield of NPs. However, in some cases it was not possible to redisperse the longer centrifuged NPs again. This was especially the case for NPs formulated from the lrPU 3, where this observation could be made in the third purification step. Due to this the lrPU 3 NPs were centrifuged only two times. After the purification, the NP dispersions were replenished to 10 mL with deionized water. The fresh formulated and purified nanoparticles were diluted 1:50 in water to obtain an appropriate concentration for DLS measurements.

The diameter of the formulated nanoparticles was between 125 nm and 195 nm with low polydispersities of 0.05 and 0.15 in case of lrPU 3, showing that well defined particles have been formed. The preferred particle diameter of drug delivery systems is very individual for each material and each application. A frequently targeted mark is a diameter of 100 nm. Although the particles in this study exceed this particle diameter, this result can be considered satisfactory at this point. For the investigation of the degradation behavior, it is sufficient that the particle sizes are in a biologically relevant range. For the investigation of biodistribution and cellular uptake as a dependency of the particle size, more sophisticated methods than nanoprecipitation could be helpful.
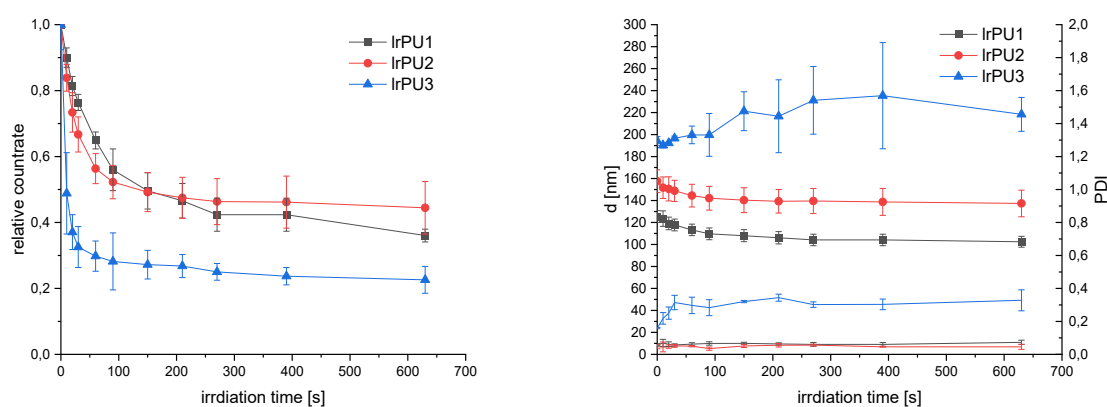

Figure 3.28 Normalized count rate (left) and particle diameter and PDI (right) of light degradable polyurethane nanoparticles determined by DLS measurements.

The stability of the NP dispersion was confirmed by repeated DLS measurements over a 24 h period without homogenizing the sample, indicating that no coagulation or sedimentation took place. Zeta-Potential measurements showed low negative potential of - 3.6 mV to - 14,3 mV. To achieve electrostatic stabilization of nanoparticles, zeta-potentials with an absolute value above 30 mV are required. Apparently, the particle dispersions are stabilized by kinetic repulsion of hydrophilic blocks, as it is known for amphiphilic structures. In the case of the lrPU 1, residual PVA, that is absorbed or embedded to the particles surface. In the case of the lrPU 2 and lrPU 3 stabilization could also be provided by the built-in hydrophilic structures.

The specified particle diameters are only apparent hydrodynamic diameters and do not represent the actual diameter of a solid particle. Measurement is based on the determination of the diffusion velocity; irregularities on the particle surface, for example, can influence the diffusion velocity and thus alter the determined diameter. Apart from the surface, the particle shape and nature of the polymer as well as the ionic concentration of the medium can influence the results of the measurement. For this reason, the diameters should be interpreted with a certain degree of caution. As the count rate (scattering intensity) is highly dependent on the particle diameter, the comparison of different scattering intensities is only possible to a limited extent. However, DLS has proven to be a practicable method for investigating the degradation behavior of NPs in past studies. The higher the chemical and physical relationship between the materials analyzed, the more reliable the direct comparisons are.

Irradiating the nanoparticles of the light degradable polyurethanes caused a decrease in the count rate in all cases. This corresponds to the disintegration of the internal structure due to the bond cleavage of the polymeric backbone. NPs formulated from the polymers lrPU 1 and lrPU 2 showed comparable degradation profile, both count rates decreased down to about 50 % of the initial intensity. The scattering intensity of lrPU 3 declined at a much faster rate and dropped down to about 20 % of the initial intensity before it remained constant at that intensity. This observation is in line with the faster and stronger decline of molecular weight and UV-VIS absorbance of lrPU 3 in Chapter 3.2.2. The hydrodynamic diameter of the light degradable NPs lrPU 1 and lrPU 2 was shrinking only marginally whereas the diameter of the lrPU 3 was rising slightly to a maximum of 240 nm. Remarkably the measurement of the diameter showed lower reproducibility, which is also reflected in the increased standard deviation. Also, the PDI rose up to about 0.4, making these nanoparticles overall less precisely defined and more polydisperse after irradiation.

The following results were determined by Prof. Dr. Albena Lederer and Dr. Susanne Boye at the Leibniz Institute for Polymer Research in Dresden. In order to investigate the relationship between the particle degradation observed in the DLS studies and the associated physical

changes in the particle structure, non-irradiated and irradiated particles were analyzed using asymmetric flow flied-flow fractionation (AF4) with UV- (280 nm), RI- and MALS-detection.

AF4 is a rather new separation method for the fractionation and analysis of high molecular weight substances and particles. In certain molar mass ranges (1 kDa – 10 MDa) AF4 is complementary to size exclusion chromatography (SEC), but whereas in SEC the separation is based on molecular size-dependent interactions with a porous stationary phase, AF4 contains one permeable wall, so a cross-flow is caused relatively to the cannel. This makes it possible to analyze charged and uncharged polymers, as well as larger analytes such as aggregates or proteins and offers a high separation range of around 1 nm to 100 µm.

To investigate the photochemical degradation of lrPU 1, 60 mg of the polymer was dissolved in 50 mL of THF and 10 mL of water and exposed in portions in UV-cuvettes with a layer thickness of 1 cm for 240 s with an irradiation intensity of 300 mW/cm². The combined fractions were then freeze-dried for transportation. To characterize the degradation, an analysis was performed using SEC. This showed a decrease in the number-average molar mass from 23 800 to 13 900 g/mol (42 %), while the polydispersity decreased from 1.89 to 1.44. For quantitative evaluation of the AF4 fractograms, the specific refractive index increments (dn/dc) were determined, which were 0.112 mL/g (non-irradiated) and 0.118 mL/g (irradiated), respectively. Nanoparticles were formulated from the polymer lrPU 1 identical to the procedure described previously in this chapter. A portion of this sample was irradiated in a cuvette with a layer thickness of 1 cm for 240 s at 300 mW/cm². The non-irradiated and irradiated lrPU 1 NPs were then analyzed using AF4 as a quadruple determination (triple determination with 250 µL injection volume and a control measurement with 500 µL injection volume). A long channel with a channel height of 490 µm, a membrane made of regenerated cellulose, and a cut-off of 10 kDa was used and 10 mM PBS buffer with a pH of 7.4 and a flow rate of 0.7 mL/min was used as the eluent.

Figure 3.29 shows the fractograms of the non-irradiated nanoparticles. The traces of the refractive index detector (RI), the UV-detector at 245 nm, and the intensity of the light scattering detector (LS) can be seen. The maximum of the RI-, UV-, and LS-traces are not identical. The RI-trace indicates the total concentration of the polymer, the UV-trace indicates the concentration of chromophore, and the intensity of the light detector depends on both the concentration and the size of the detected particles. In addition, diagram a) shows the radius of gyration (R_g) and diagram b) shows the hydrodynamic radius (R_h) of the respective eluted fraction.
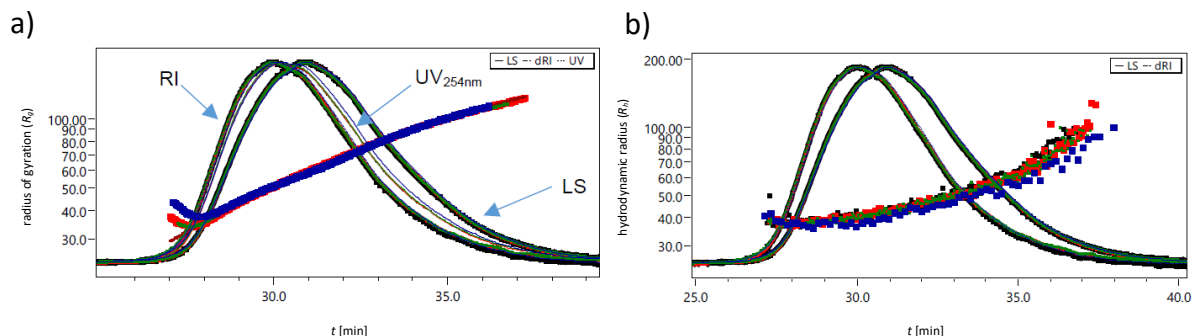
Figure 3.29 Fractograms of non-irradiated NPs formulated form IrPU 1 recorded by RI-, UV- and light scattering (LS) detectors. The left diagram (a) displays the radius of gyration (R_g), the right diagram (b) shows the hydrodynamic radii (R_h).

Both values for the radii, the radius of gyration and the hydrodynamic radius, increase with a longer elution time, which is a plausible result of fractionation according to particle size. Based on the data obtained, additional information about the nature of the particles can be gained using further evaluation methods. In the conformation plot, the logarithmic radius of gyration (log R_g) is plotted against the logarithmic molecular weights (log M_w). The slope of the line (v, Flory exponent) provides information about the nature of the nanostructure under investigation. The Flory exponent determined was v = 0.52, which is characteristic of tangled, well-flushed structures (0.5 – 0.7). Hard spheres usually have a value of 0.33, while a value of 1.0 indicates a rigid rod.
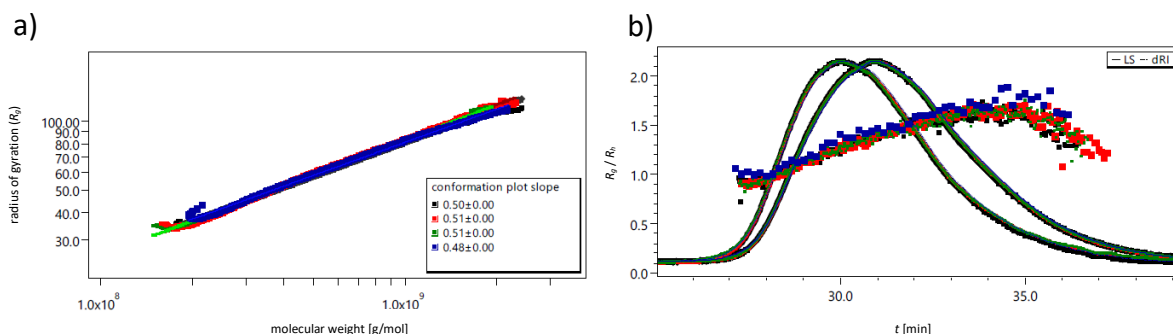
Figure 3.30 Scaling Plot (a) and Burchard-Stockmayer plot (b) of non-irradiated IrPU 1 nanoparticles.

As a final evaluation step, the quotient of R_g/R_h was plotted against the elution time, shown in Figure 3.30 (right). This so-called Burchard-Stockmayer plot shows the shape parameter as a function of particle size. This value increases over the entire elution time of the particles, indicating that not only one conformation is present, but that somewhat inhomogeneous structures coexist. At the elution maximum, the value is 1.25, which is typical for highly branched, compact structures.

In the case of irradiated nanoparticles, similar observations were made as with non-irradiated particles. Figure 3.31 shows the fractograms of the non-irradiated nanoparticles. As before, the traces of the refractive index detector (RI), the UV-detector at 245 nm, and the intensity of the light scattering detector (LS) are displayed as well as the radius of gyration (left) and the hydrodynamic radius (right).
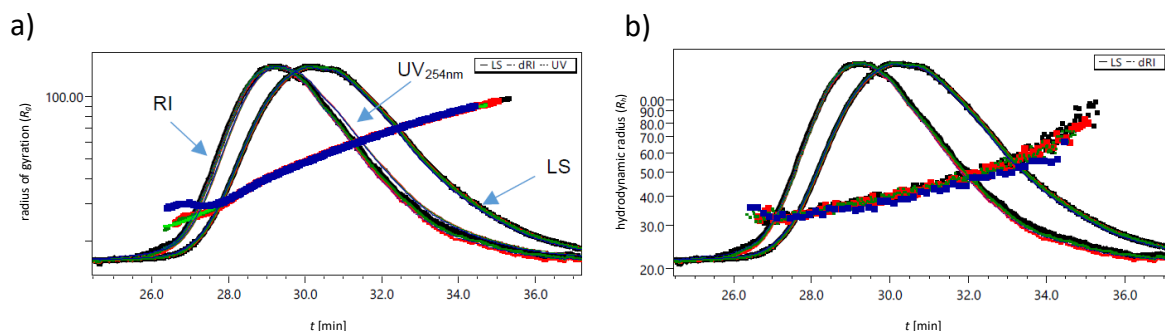

Figure 3.31 Fractograms of irradiated NPs formulated form lrPU 1 recorded by RI-, UV- and light scattering (LS) detectors. The left diagram (a) displays the radius of gyration (R_g), the right diagram (b) shows the hydrodynamic radii (R_h).

The conformation plot reveals a FLORY exponent is 0.47 in case of the irradiated particles, which is slightly lower compared to the irradiated particles. The BURCHARD-STOCKMAYER plot of the irradiated particles also increases over the elution time of the particles. As their non-irradiated counterparts, not only one conformation is present, but inhomogeneous structures coexist.
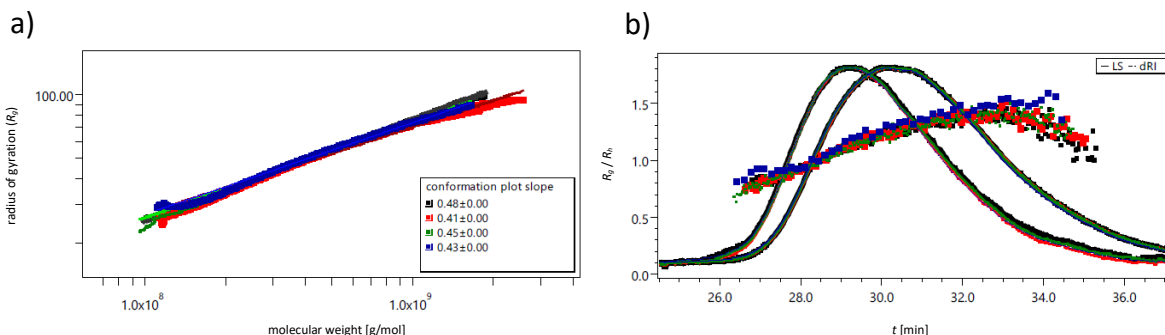

Figure 3.32 Scaling Plot (left) and BURCHARD-STOCKMAYER plot (right) of irradiated lrPU 1 nanoparticles.

The apparent density can be calculated based on the determined molecular weight and particle diameter. All determined values and the apparent density are listed in Table 3.8 for both, non-irradiated and irradiated particles.

Table 3.8 Comparison of the physical parameters of non-irradiated and irradiated lrPU 1 NPs. The radius of gyration (R_g), Berry fit 1ˢᵗ order), the hydrodynamic radius (R_h), the mean density (ρ), the density at the elution maximum (ρ^{*2}), and the Flory coefficient (v).

sample	$R_g{}^{*1}$	R_h	ρ	ρ^{*2}	v
non-irradiated lrPU 1 NPs	78.0	49.2	1.59	1.26	0.52
irradiated lrPU 1 NPs	66.3	47.4	1.40	1.10	0.47

Irradiation causes the radius distribution of both the radius of gyration and the hydrodynamic radius to shift slightly to lower values. This is consistent with previous observations made using batch DLS. In addition, the Flory coefficient decreases from 0.52 to 0.47. Both values are characteristic of clumped, well-flushed structures. The slight decrease in *v* can be interpreted as a slightly more compact conformation. The apparent density of the non-irradiated particles at the elution maximum of 1.26 is typical for highly branched or compact structures, while the density of 1.1 after irradiation is more typical for hollow structures. The data clearly show that the constitution of the particles has changed significantly as a result of irradiation. However, neither before nor after irradiation were there any uniform, homogeneous particles; instead, several inhomogeneous structures coexisted. Accordingly, it is not possible to detect a clear shift from one structure to another.

3.2.4 Conclusions

Despite the inclusion of considerable amounts of hydrophilic PEG segments, the particles of lrPU 2 did only show a slight increase of particle degradation speed in aqueous media compared to particles formulated from lrPU 1. Particles formulated from lrPU 3 however showed drastically increased degradation of the particles. This increased degradation kinetics of the particles can be attributed not only to the higher polarity of the oligomeric degradation products, but also to an increased degradation rate of the polymer backbone, as demonstrated by the results of the UV-VIS analysis and SEC measurements. Furthermore, the UV-VIS spectra during the irradiation shows shifted absorption bands compared to the other samples despite using the same chromophore. This data indicates that the decay of the excited *aci*-nitro state of the oNB chromophore might take place, presumably by the attendance of the tertiary amino group. It is beyond the scope of this work to investigate in depth the underlying chemical process for the accelerated decrease in molecular weight.

3.3 Light cleavable bromocoumarine polyurethanes

The following chapter is dedicated to the synthesis and characterization of the degradation of bromohydroxycoumarin (BHC) derived monomers and polymers. The aim is to synthesize a hydroxy bearing derivate of bromocoumarin and extend it with a linker to form a BHC based diol-monomer that can easily be built into the backbone of polymers by polyaddition. A hydrophobic homopolymer and an amphiphilic block co-polymer should be synthesized and used for nanoparticle formulation. Polymers and their respective nanoparticle formulations are then to be studied regarding their degradational behavior in response to UV-light irradiation.

3.3.1 Synthesis low molecular compounds

The synthesis started with a PECHMANN-Condensation of 4-bromoresorcin (**17**) and methyl 4-chloro-3-oxobutanoate (**18**) in methanesufonic acid and was carried out in a 10 g scale according to a protocol by MÜLLER *et al.*[138] With a crude yield of 96 % and a purity of about 80 % (based on ^{1}H-NMR spectral data), the reaction took place with a satisfying conversion. Elongation of the reaction time led to discoloration of the reaction mixture and formation of complex side product mixtures. However, the workup of the first synthesis step turned out to be challenging. The intermediate product **19** has bad solubilities in a variety of common solvents. Purification by column chromatography, using a gradient solvent system of *iso*-hexane/THF in a ratio of 1:2 to 1:5 could be carried out, but was accompanied by precipitation during the column process. A recrystallization procedure by solving in hot THF and precipitation by addition of *iso*-hexane was the most convenient method to purify the product but led to a decrease in yield. The high losses of product in this step were accepted since this was only the first synthesis step and educts are cheap and readily available. To streamline the whole synthesis sequence, the purification process of the first step offers the most potential for a yield increase.
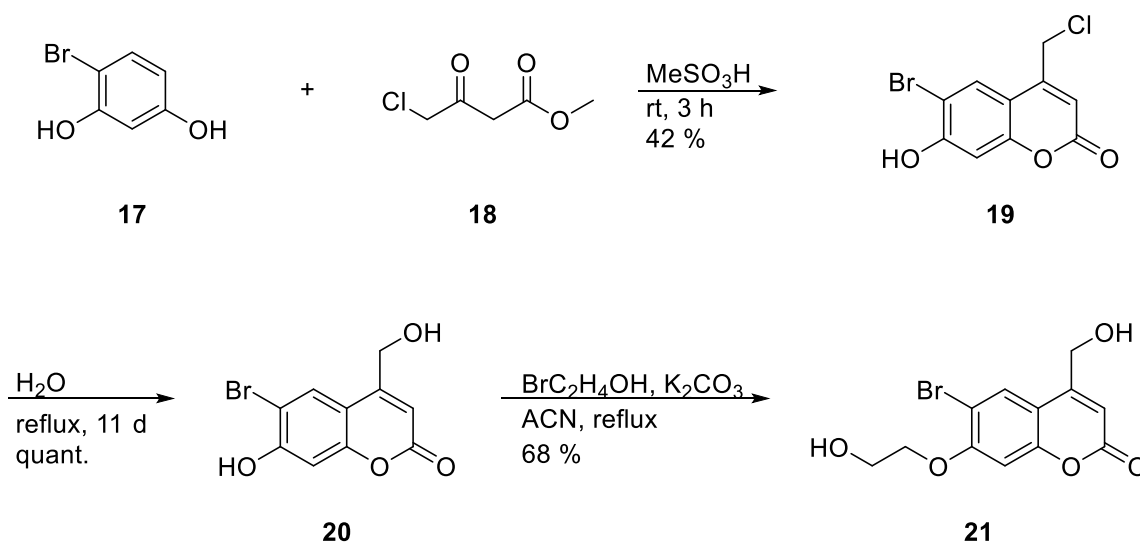
Scheme 3.9 The synthesis to from the light-responsive diol **21** in a yield of 29 % over three steps.

The second synthesis step was a nucleophilic substitution of the chlorine group of **19** by refluxing in water for 5 d and was carried out according to a protocol by MÜLLER *et al*. The reaction was tracked by TLC, and after 5 d the conversion was determined by ^{1}H-NMR and turned out to be only 70 %. Only after 11 d of reaction time the quantitative yield mentioned in the literature could be achieved in the first attempt. Since in other batches reaction time differed, it was assumed, that minor impurities influenced the reaction time of this synthesis step. As an attempt to accelerate the reaction, NaHCO$_3$ was added to the reaction mixture, to remove the formed HCl from the reaction faster. However, this did not speed up the reaction and led to formation of a complex mixture of side products. Since it is assumed that the varying reaction rate is related to trace impurities from acid from the previous synthesis. Probably filtration through a basic filter pad in the purification procedure of the first step, or addition of base in the second step, could accelerate the reaction. Furthermore, the addition of more water could lead to an acceleration of the reaction, since during the synthesis a large part of the material is in a solid phase and is therefore not available for a reaction without hindrance. Increasing the amount of water would proportionally dissolve a higher percentage of the product, making it freely available for the reaction. However, the quantitative yield was satisfactory despite the long reaction time, and since the reaction was carried out on a multigram scale, there was no need to repeat the synthesis. Also, the workup of this step was very simple under the given reaction conditions, as the product precipitates when the water cools down and can be isolated by filtration.

The third step of the synthesis was a nucleophilic substitution to derivatize the phenol function of **20** with a hydroxy ethoxy ether to get the final bromohydroxycoumarin (BHC) chromophore **21**. By this derivatization, the light-cleavable group has two primary hydroxy functionalities to enable copolymerization into polyurethane backbones. A comparable derivatization was already carried out in the previous section for the derivatization of **7** to **8**

and is shown in Scheme 3.4. However, educt **20** was not completely soluble under the same reaction conditions as in the previous section, so different solvents and reaction conditions were tested, which are listed in Table 3.9. Despite the extensive testing, the best conversion and yield was achieved under the initial reaction conditions (batch 11). The educt **20** showed bad solubility in a lot of different solvents, which is why a set of different solvents, bases and temperatures have been screened (Table 3.9). It was remarkable that increased reaction temperatures of 120°C in DMF and DMSO did not lead to any formation of the main product and a complex mixture of by-products was formed. Best conversions and yields could be observed at around 80°C. Varying the used base between NaOH and K_2CO_3 made no difference, presumably because sufficient time for full deprotonation of the phenol was given in both cases. Using an organic base (Et$_3$N) proved to be disadvantageous despite the better solubility. The addition of 18-crown-6 ether (18-c-6) to raise solubility and reactivity of the K_2CO_3 did not lead to improvement of the conversion, also the microwave assisted synthesis, following a literature procedure, only lead to very low conversion. At the best reaction conditions, a conversion of 84 % and a final yield of 68 % of pure product **5** was accomplished.

Table 3.9 Listing of performed variations of the substitution of bromoethanol with phenol **20** to form BHC-diol **21**.

Batch	base	solvent	temperature	conversion*	yield
1	K_2CO_3	DMF	120°C	-	-
2	K_2CO_3	DMSO	120°C	-	-
3	K_2CO_3	ACN	40°C	81 %*	-
4	K_2CO_3	ACN	80°C	75 %**	40 %
5	Et$_3$N	ACN	40°C	20 %**	
6	K_2CO_3, 18-c-6, microwave	acetone	55°C	6 %**	-
7	K_2CO_3, 18-c-6	acetone	55°C	20 %**	-
8	NaOH	ACN	80°C	52 %**	-
9	K_2CO_3	ACN	80°C	52 %**	50 %
10	K_2CO_3, 18-c-6	ACN	80°C	51 %**	-
11	K_2CO_3	ACN	reflux (~82°C)	84 %*	68 %

* based on ^{1}H-NMR data of crude product
** based on ^{1}H-NMR data of reaction mixture

Purification of the final product could be carried out using column chromatography but also recrystallization from THF/*iso*-hexane was a convenient and feasible method for upscaled reactions. To test out an alternative synthesis procedure, surplus ethylene glycol has been monofunctionalized with a tosyl group, to convert the hydroxy group into a good leaving group. This reagent was used as a substitute for bromoethanol in the final synthesis step of

the synthesis of the chromophore **21**. The derivatization step had a good conversion of 84 % (based on NMR data of the isolated crude product).
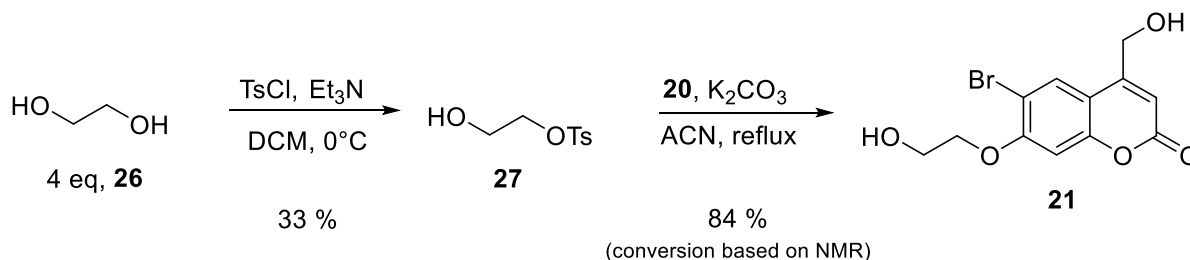

Scheme 3.10 Alternative synthesis protocol for the derivatization of **20** to form the chromophore **21**.

However, this yield was identical to the protocol with bromoethanol. But the required activation step of the glycol with its bad atom economy and additional effort provided no advantage over the synthesis with bromoethanol.

3.3.2 Synthesis of bromocoumarin based polyurethanes

Starting from the chromophore BHC-diol **21** three polyurethanes have been synthesized, each with hexamethylene diisocyanate (HDI), isophorone diisocyanate (IPDI) and *L*-lysine diisocyanate (LDI) as the reactive counterpart.
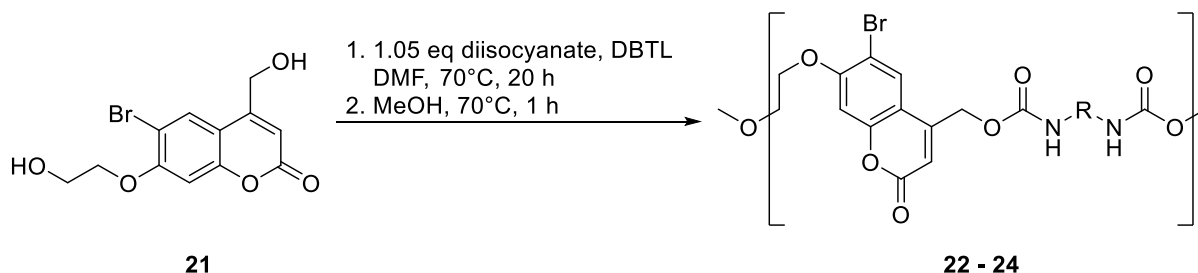
Scheme 3.11 Synthesis of the stimuli responsive bromocoumarin based polyurethanes **22**, **23** and **24** by DBTL polyaddition.

Scheme 3.11 shows the standard polyurethane synthesis protocol with DBTL as a catalyst, the polymerizations could be carried out in THF as well as in DMF. However, due to its volatility, huge proportion of the THF evaporated over the long synthesis duration of 18 – 20 h. Since the synthesis in DMF was equally effective, DMF was chosen as the preferred solvent. The final polymers were isolated by precipitation followed by centrifugation. SEC analysis showed number-average molecular weights of 5 700 – 10 300 g/mol. Procedures with all used diisocyanates, HDI, IPDI as well as LDI, were successful and lead to yields of 69 – 93 %. Deviations can most likely be attributed to random, small deviations in the execution of the synthesis and do not allow any conclusions to be drawn about systematic differences, since only slight variations in the equivalents of polyadditions cause vastly different molar masses.

Table 3.10 Average number molar mass (M_n), polydispersities ($Đ$) and yield of the synthesis of BHC-diol (**21**) based polyurethanes.

Batch	Polymer	M_n	Đ	yield
1	BHC-HDI (**22**)	8 900	1.98	74 %
2	BHC-IPDI (**23**)	10 300	2.41	93 %
3	BHC-LDI (**24**)	4 600	1.84	95 %
4	BHC-LDI (**24**)	5 700	1.54	69 %
5	BHC-LDI (**24**)	7 600	1.77	77 %
6	mPEG-BHC-LDI (**25**)	7 200	1.52	22 %

As a synthesis with all every isocyanate was possible, LDI was chosen for the synthesis of an amphiphilic triblock copolymer since LDI is an amino acid based diisocyanate and is expected to form lysin as a degradation product under physiological conditions and therefore offer a higher biocompatibility. Analogous to the synthesis of homopolymers, amphiphilic triblock copolymers with terminal PEG chains should be synthesized as hydrophilic blocks.
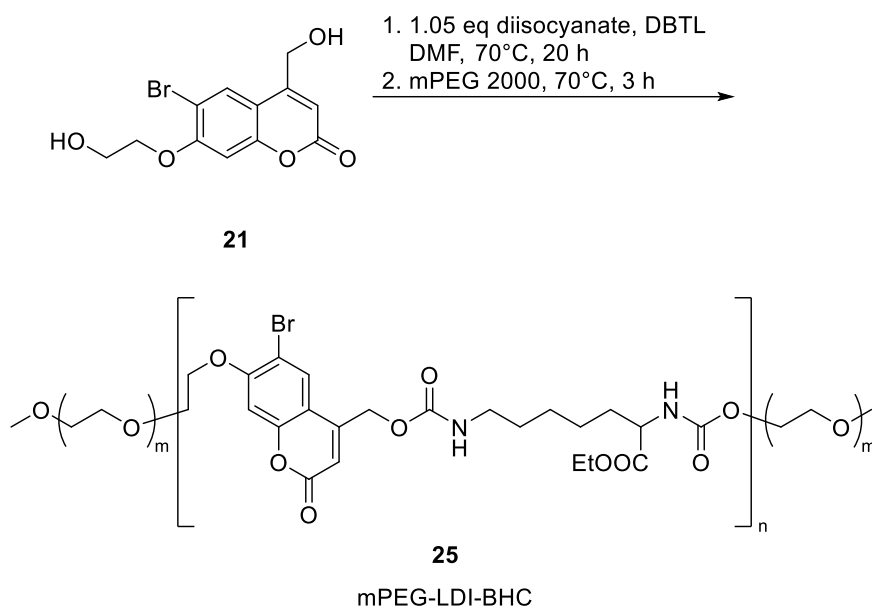
Figure 3.33 Synthesis of the amphiphilic triblock copolymer mPEG-LDI-BHC (**25**) by termination of the polyurethane synthesis with mPEG 2000.

The synthesis was carried out analogously to the synthesis of the homopolymers, with the difference that the end groups were terminated with the monofunctional alcohol mPEG 2000 instead of methanol. **25** was isolated with a relatively low yield of only 22 %, because it had to be precipitated from THF in diethyl ether four times, to purify the polymer from access mPEG. Another derivative of the triblock copolymer was synthesized in which the hydrophilic blocks were formed by termination with mPEG 5000. The polarity of the resulting polymer was so high that no suitable solvent system for selective precipitation could be found. Due to the high molecular weight of the mPEG, purification by dialysis was also not possible. For this reason, only the mPEG 2000 based triblock copolymer was further characterized.

3.3.3 Light induced polymer degradation

First, the photoisomerization of the BHC group was characterized by irradiation of a BHC containing polymer with UV-light. For this purpose, a solution of BHC-LDI (**24**) was prepared in DCM and the UV-VIS spectrum was measured after different lengths of irradiation with UV-light.
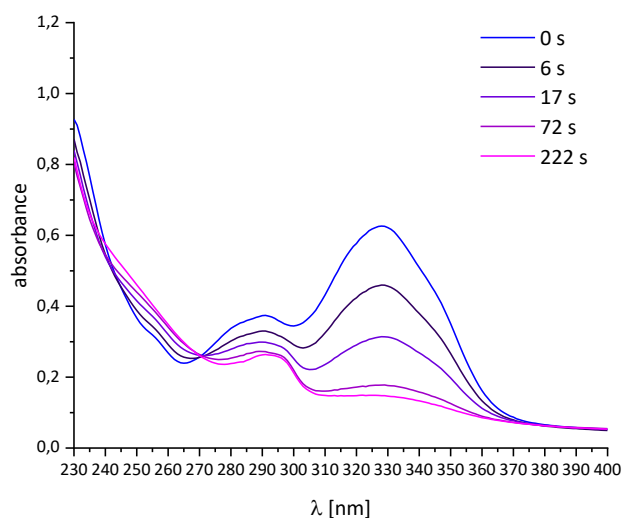

Figure 3.34 UV-VIS spectra of BHC-LDI (**24**) in DCM during irradiation with UV-light.

Figure 3.34 shows the UV-VIS spectra of the polymer BHC-LDI (**24**) after each irradiation step. The spectra of the polymer before irradiation shows two maxima around 290 nm and 320 nm, during irradiation both of the maxima decline in intensity, while absorbance at 240 nm to 270 nm is rising slightly. At 270 nm the isosbestic point can be observed. Figure 3.35 shows the absorbance of the spectra at the maximum at 320 nm after each iteration of irradiation.
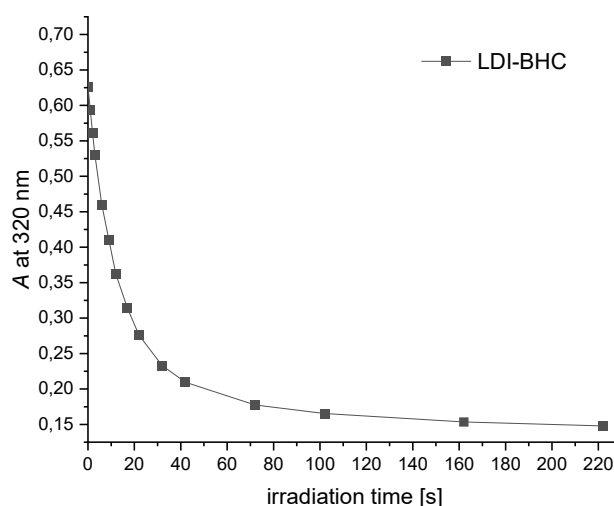
Figure 3.35 Decline of absorbance of the polymer BHC-LDI at the absorbance maxima at 320 nm
after each irradiation step of the polymer BHC-LDI (**26**) with UV-light.

The solved polymer degrades rapidly under the selected irradiation conditions. The half-life of the reaction is only about 6 s and the chromophore seems almost fully degraded after 100 s. This is exceptionally fast, especially compared to the photoreactions of the oNB polymers in the previous chapter shown in Figure 3.26.

Furthermore, the polymer BHC-LDI (**22**) was dissolved in THF and irradiated with UV-light for different time intervals from 0 s to 240 s to check how the photo reaction translates into a decrease in molar mass. The polymers irradiated for different times were characterized by THF SEC (with PS standard). The determined number-average molar mass (M_n) decreased from 4 600 g/mol to 3 700 g/mol over the irradiation period, which is only a decrease of about 20 %. Irradiation and SEC measurement repeated in HFIP (hexafluoro isopropanol) as a solvent, almost identical molecular weights and relative decrease were observed. The large difference between the rapid photoreaction and the only slight decrease in molecular weight shows that the photoreaction of the chromophore does not completely translate into a splitting of the polymer. One possible explanation is that the photoreaction chooses a different reaction path and only partial cleavage of the O-N bond takes place. This could be favored in particular by the fact that only traces of water are present in the organic solvents, but it is necessary for the hydrolytic cleavage of the urethane group. Another possible explanation could be that cross-linking also takes place in parallel to the photolytic cleavage of the polymer chain, as it is known from coumarin structures, that they can perform a [2+2] cycloadditions.[260]

3.3.4 Determination of critical micelle concentration

The formation of nanostructures by self-assembly above the critical micelle formation concentration as well as the nanoprecipitation by dripping of polymer solution into a precipitant were considered as feasible methods of particle formation.

To determine whether the formation of nanostructures by self-assembly is an efficient method of nanoparticle formation, the critical micelle formation concentration (CMC) was first determined by plotting the derivative count rate measured *via* DLS against the logarithmized mass concentration of the polymer concentration series. Above the CMC, there is a stronger increase in the count rate compared to below the threshold. The CMC can be determined at the intersection of the two straight lines in the linear areas of the application.[261,262]
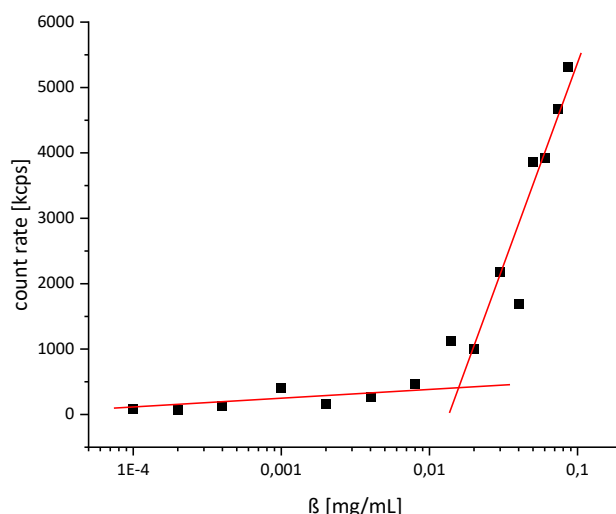
Figure 3.36 Plot of the count rate against the logarithmic mass concentration (*ß*) of mPEG-BHC-LDI (**25**) with two approximately linear ranges. The intersection point indicates the critical micelle concentration (CMC).

From stock solutions of mPEG-BHC-LDI (**25**) in THF, a solution of the required mass of polymer was prepared in 1 mL THF for each data point and added to 2 mL double-distilled water. The solutions were stirred for at least 24 h to allow the THF to evaporate and the polymers to assemble into nanoparticles. The particles formed in this way were measured using DLS in order to examine the solution for nanoparticles and characterize them if applicable. Figure 3.36 shows the plot of the count rate against the mass concentration of amphiphilic triblock copolymer mPEG-BHC-LDI (**25**) in water. It can be observed that the scattering intensity increases with increasing concentration. In the very low concentration ranges it increases almost none at all, but from about 0.01 mg/mL it increases strongly. This effect is emphasized by adding trend lines in red to the assumed linear range. The intersection point, at which the CMC is assumed, is around 0.015 mg/mL. However, as the interpretation of the linear ranges is purely subjective and the measured values deviate

more strongly from the trend lines in the area of the intersection point, a large error must be assumed for this value. For a qualitatively comparable, mPEG-terminated polycaprolactone, CMCs in the range of $5.1 \cdot 10^{-4}$ mg/mL and $5.6 \cdot 10^{-3}$ mg/mL were determined by fluorescence measurements.[263] Another amphiphilic triblock polymer with polyethylene glycol termini yielded a CMC of 0.04 mg/ml using the above method.[262] The measured hydrodynamic diameters of the particles at the individual measuring points were between 53.1 nm and 100.9 nm, which is in the ideal range for use as nanocarriers for drug delivery systems. The polydispersities of the particle formulations were between 0.056 and 0.159 and are therefore well-defined nanoparticles with a narrow particle size distribution.

3.3.5 Formulation and degradation of loaded nanoparticles

Nanoparticles were formulated from the amphiphilic triblock copolymer mPEG-BHC-LDI (**25**), which are loaded with the fluorescent dye nile red (NR) as a payload. Nile red is a dye that is used as a model drug in many applications. It fluoresces in the red range and has a maximum emission at around 650 nm. Both the emission maximum and the quantum yield are strongly dependent on its chemical environment, such as the solvent. In *n*-heptane, the maximum emission is around 520 nm, whereas in acetone it is 600 nm. Its fluorescence activity rapidly quenches in the presence of water, making it an ideal model substance for the indication of potential drug releases from hydrophobic carriers to aqueous media.[264,265] Although the formulation of nanoparticles *via* self-assembly leads to very well-defined and small nanoparticles, the formulation of loaded particles was carried out *via* nanoprecipitation, as this process in combination with the loading of particles is very convenient, fast and efficient and has led to good results in previous experiments.

The polymer **25** and NR were dissolved in 1 mL THF, whereby the dye caused an intense red coloration. When injected into 10 mL of 2 % PVA solution, a drastic color change to violet could be observed immediately. This is already an indicator that the environment-sensitive dye is in an altered chemical media. Stirring continued to evaporate the THF and then the particles were purified by multiple iterations of centrifugation, decantation and redispersion in water. The DLS measurement shows nanoparticles with a hydrodynamic diameter of 230 nm. The PDI was 0.067, so the particles have a narrow size distribution. The NR-loaded mPEG-BHC-LDI (**25**). NPs were also measured by fluorescence spectroscopy at an excitation wavelength of 485 nm, where an intense fluorescence with an emission maximum at 645 nm was measured.
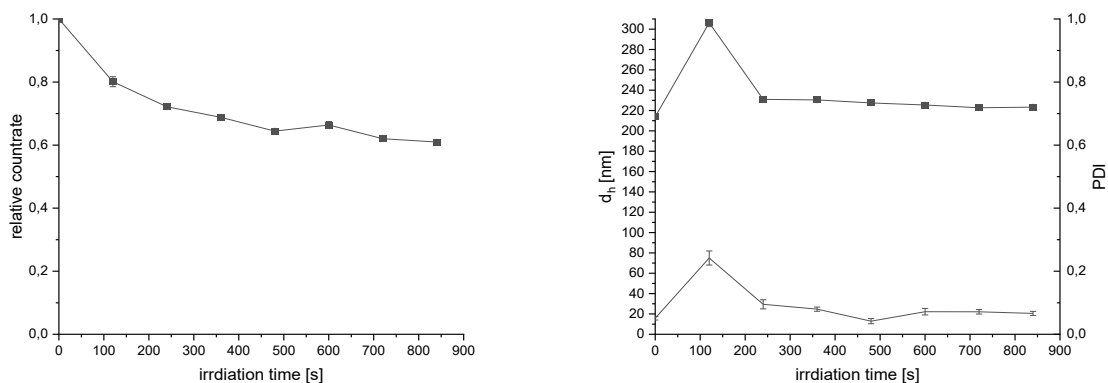
Figure 3.37 Progression of the relative scattering intensity (left) and the determined hydrodynamic diameter and PDI in the DLS measurement of NR-loaded mPEG-BHC-LDI (**25**) particles with increasing irradiation time.

The diluted particle dispersion was irradiated stepwise in a quartz cuvette with UV-light in the wavelength range 320 – 480 nm and a strength of 300 mW/cm². The scattering intensity of the irradiated particles was measured after each irradiation step using DLS and is displayed in Figure 3.37. The course of the scattering intensity decreases rapidly at the beginning but finally runs asymptotically towards a limit value that corresponds to about 60 % of the original intensity. In comparable experiments, the decrease in scattering intensity is associated with a degradation of the nanoparticle structure, which is why it can also be assumed here that the structural integrity of the particle is attacked by the photoreaction of the chromophore. These observations are consistent with the observations from the previous chapter and earlier investigations.

The emitted fluorescence spectra can be seen in Figure 3.38. The irradiation of the particles has two effects: firstly, the fluorescence intensity drops sharply and secondly, the emission maxima shift to lower wavelengths. Both are indicators that the chemical environment of the dye is changing. In particular, the strong decrease in intensity can be observed when NR is exposed to an aqueous environment and the fluorescence activity is quenched. Both observations can therefore be interpreted as signs that the model active substance is released from the particles and enters an aqueous environment.
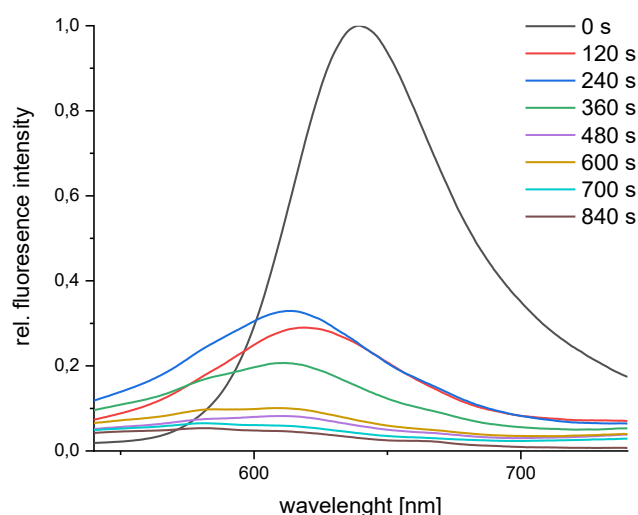
Figure 3.38 Fluorescence emission spectra of NR-loaded mPEG-BHC-LDI (**25**) after different exposure times of the particles with UV-light. The excitation frequency was 485 nm.

3.3.6 Conclusions

In summary, the chromophore BHC (**21**) was synthesized in three steps with a yield of 29 %. The light-cleavable building block has two primary diols and could be polymerized to a polyurethane in a selection of commercially available diisocyanates. Polymers synthesized from this can be degraded to lower molecular weight oligomers by irradiation with UV-light. However, complete degradation cannot be achieved. By terminating the reaction with the monofunctional polyethylene glycol mPEG 2000, an amphiphilic triblock copolymer could be synthesized, which can be formulated into nanoparticles by self-assembly and nanoprecipitation. Furthermore, the model drug nil red (NR) could be included into the particles as cargo. When irradiated with UV-light, the nanoparticles showed clear signs of structural degradation due to a reduction in scattering intensity. The course of the fluorescence activity of the NR also indicates that irradiation led to the release of the model drug.

This exciting sub-project shows promising and interesting results that offer a large number of further possibilities for additional investigations.

First of all, the work-up step of the monomer synthesis offers great potential for optimizing the work-up in order to obtain a large amount of pure product from the already high crude yield. Furthermore, it would be interesting to observe whether the presence of water during degradation of the polymer dissolved in organic solvent would cause a greater reduction in molecular weight. In addition, the particles formulated *via* self-assembly show a very promising particle size, whereas the particle sizes from nanoprecipitation are above the ideal range for drug delivery purposes. It would therefore be interesting to test different methods

of NP formulation *via* self-assembly, in which a drug can be loaded in. For this approach an incubation-based method was carried out in initial trials, but this was not successful, which is why this method was not pursued further.

In addition to these direct questions, more in-depth issues can also be addressed. First of all, an extension of the substrate scope would be interesting. The variation of the mPEG block length has already been demonstrated as a proof-of-concept with mPEG 5000, however it could not be isolated in pure form and led to triblock copolymers that were soluble in water. Therefore, an investigation of mPEG derivatives with chain lengths below 5 000 g/mol would probably be of interest. In addition, the influence of the chain length of the hydrophobic block should be investigated. The hydrophilic/hydrophobic ratio has a major influence on the morphology of the aggregates such as the particle size. In addition, a shorter chain length of the degraded fragments, which are still attached to the long mPEG chain, could become water-soluble by their small mass ratio compared to the long mPEG chain. This could lead to an amplified disintegration of the particle fragments after irradiation. Such an effect would presumably be reflected in a greater decrease in the scattering intensity in the DLS.

It could also be of interest to carry out in-depth studies of the core-shell structure in order to gain a more concrete idea of the composition of the nanoparticles. Finally, a more extensive investigation of the frequency required for the decomposition of bromocoumarin structures could be of interest. The penetration depth of light into human tissue is highly dependent on the wavelength, so it would be of interest to know which wavelength is necessary to cleave bromocoumarin. In addition, there are known examples of bromocoumarin in the literature in which it has been shown that it can be cleaved by means of two photon absorption and whether this effect is also sufficient to cause release into particles.

4 Experimentals

4.1 Materials

Chemicals	Purity	Supplier
1,4-Benzenedimethanol	> 99.0 %	TCI
18-c-6 ether	99 %	Sigma-Aldrich
2,2-dimethoxy propane	> 98.0 %	TCI
2-[2-(2-Methoxyethoxy)ethoxy]ethyl acrylate	> 90.0 %	TCI
2-Bromoethanol	> 95 %	TCI
3,5-Di-*tert*-butyl-4-hydroxytoluene (BHT)	99 %	Fluka
4-Bromoresorcinol	98 %	Acros Organics
5-Hydroxy-2-nitrobenzaldehyde	> 98.0 %	TCI
Acetone	technical grade	Stockmeier Chemie
Acetonitril (ACN)	> 99.9 %	Carl Roth
Benzene	99.9 %, dry	Acros Organics
Borane–tetrahydrofuran 1 M in THF	-	Sigma-Aldrich
Chloroform	distilled	Stockmeier Chemie
D_2O	99.9 %	Deutero
DCl (38 %) in D_2O	99.5 %	Deutero
Dibutyltin dilaurate	95 %	Sigma-Aldrich
Dichlormethane (DCM)	HPLC grade	Carl Roth
Diethanolamine	> 99 %	Carl Roth
Diethyl ether (Et_2O, tech.)	technical grade	Stockmeier Chemie
Dimethyl sulfoxide-d_6 (DMSO-d_6)	99.8 %	Deutero
Ethyl acetate (tech.)	technical grade	Stockmeier Chemie
Ethyl chloroformate	98 %	Fluka Analytical
H_2O	deionzied	-
Hexamethylene diisocyanate	98 %	Sigma-Aldrich
Hydrochlorid acid	38 %	Stockmeier Chemie
iso-Hexane (tech.)	technical grade	Stockmeier Chemie
Isophorone diisocyanate	95 %	Acros Organics
L-Lysine diisocyanate	96.0 %	Thermo Fisher
Methanesulfonic acid	> 99.0 %	Sigma-Aldrich
Methanol	99.5 %	Grüssing
N,N-Dimethylformamide (DMF, dry)	99.9 %, dry	Thermo Fisher
Nitroterephthalic ccid	> 98 %	TCI
Polyvinyl alcohol (Mowiol 4-88)	-	Carl Roth
Potassium carbonate	technical grade	Stockmeier Chemie
p-Toluenesulfonic acid	98.5 %	Sigma-Alrich
Sodium borohydride	99 %	Sigma-Aldrich
Sodium hydroxid	technical grade	Stockmeier Chemie
Sodiumbicarbonate	technical grade	Stockmeier Chemie
Sodiumcarbonate	technical grade	Stockmeier Chemie

Sodiumsulfate	technical grade	Stockmeier Chemie
Tetrahydrofurane (THF)	99.5 %	Grüssing
Tetrahydrofurane (THF, dry)	99.9 %, dry	Thermo Fisher
Tetrahydrofurane (THF, tech.)	technical	Stockmeier Chemie
Triethylamine	> 99.0 %	TCI

4.2 Methods

UV-VIS spectroscopy

UV-VIS spectra were recorded on an Analytik Jena Specord 50 PLUS UV-VIS spectrophotometer, with the software Aspect UV and processed and visualized with OriginPro 2021.

NMR spectroscopy

A Bruker Avance 500 and a Bruker Ascent 700 spectrometer were used to record the ^{1}H NMR spectra at 500 MHz and 700 MHz and ^{13}C NMR spectra at 125 MHz and 176 MHz respectively. The kinetic degradation studies were carried out using a Bruker Avance 300, the ^{1}H NMR spectra were measured at 300 MHz. As a solvent for measurements, dimethylsulfoxide-d_6 (DMSO-d_6, 99.8 % D), deuterium oxide (D$_2$O, 99.9 % D) and chloroform-d (CDCl$_3$, 99.8 % D) were used. TopSpin 4.3.0 (*Bruker*) was used for calculation and analysis of the data.

Dynamic light scattering (DLS)

DLS Measurements were performed using a Zetasizer Nano ZS from Malvin Panalytical at an angle of 173°. Zetasizer Nano software 3.30 was used to perform the measurements and process the data. Calculation and visualization of the data was carried out using OriginPro2021.

Time-resolved multi angle light scattering (TR-MALS)

Time-resolved light scattering experiments were carried out with the multi-detection laser light scattering system ALV/CGS-3/MD-8. A He–Ne laser with a wavelength of 632.8 nm was used as a light source. The system provides eight detectors positioned at angular increments of 8°, which allows simultaneous time-resolved SLS and DLS. An angular range of 30° ≤ ϑ ≤ 86° was measured.

Size exclusion chromatography (SEC)

The SEC measurements were performed in THF as a solvent. A system operating at 1 mL/min equipped with two consecutive columns (PSS-SDV, 10^5 Å and 10^3 Å) was employed. For detection, a Knauer RI detector and a Merck L4200 UV-detector were used. The set wavelength was 280 nm, unless otherwise specified. The molecular weight determination was substance-specific on the basis of narrowly distributed polystyrene standards, and the WinGPC Unity software from PSS was used to record and analyze the measurement results. Visualization of the data was carried out using OriginPro2021.

Asymmetric flow field flow fractionation (AF4)

An AF4 System Eclipse DUALTEC (Wyatt Technologies Europe) with Agilent pump system (1260er Series) was used with a long channel (490 µm channel height) and a regenerated cellulose membrane (cut-off: 10 kDa). 10 mM PBS-Puffer (pH = 7.4) was used as an Eluent. The LS detector was a DAWN HELEOS-II (Wyatt) with a wavelength of 660 nm, the RI detector was an Optilab T-rEX (Wyatt) with a wavelength of 660 nm and the UV detector was an SPD-M20 (Shimadzu) with 254 nm, 280 nm, 400 nm and 500 nm wavelength. A flowrate of 0.7 mL/min at 25°C was applied. A cross-flow of 2 mL/min was applied for 3 min followed by an exponential decrease of cross-flow from 2 mL/min to 0 mL/min and finally a cross-flow of 0 mL/min was held for 20 min. Three samples with 250 µL and one sample with 500 µL volume were injected.

Differential scanning calorimetry (DSC)

Glass transition temperature (T_g) was measured with a Netzsch DSC 204 F1 Phönix at a heating rate of 10 K/min under nitrogen atmosphere.

Melting Point

The melting point (T_m) was measured with a Melting Point B-545 from Büchi with a heating gradient of 1 °C/min.

Column chromatography

The stationary phase was silica gel 60 (0.040 – 0.063 mm). All solvents used were prior cleaned by rotary evaporation and eluent ratios are given in synthesis procedures.

ESI-ToF-mass spectrometry (MS)

ESI-ToF-MS measurements were performed on the mass spectrometer SYNAPT-G2 HDMS™ from Waters. Following parameters were set: capillary voltage: 2.5 kV; sampling cone voltage: 50 V; extraction cone voltage: 3 V.

UV-irradiation

Irradiation of samples was performed by an Exceltias Technology OmniCure S1500 UV-lamp with a wavelength of 320 – 480 nm. Irradiation of samples was carried out in a 3 mL quartz cuvette at a distance of 5.2 cm, intensity was adjusted to be 300 mW/cm^2 at the surface of the cuvette. Irradiation intensity was measured with an OmniCure R2000 Radiometer.

Fluorescence spectroscopy

The fluorescence spectra were recorded on a Jasco FP8300 spectrometer. Data processing was carried out using Spectramanager software. Excitation wavelength was set to 485 nm and emission spectra was detected in a 90° angle in the range of 540 – 750 nm.

Formulation of nanoparticles

5 mg of polymer sample were dissolved in 1.0 mL of THF and get fast injected through a cannula into 10 mL of 2 % PVA solution and stirred for 30 min. The crude nanoparticles were divided into six fractions, centrifuged at 12 kRCF for 2 h and two times for 1 h, decanted and redisperse in water.

Citrate-phosphate buffer solution

Based on a literature known citrate-phosphate buffer (McILVANE buffer) the composition of isotonic buffers with an osmotic concentration of 280 mosmol/L at pH 3.0, 5.0, 6.0 and 7.4 was calculated according to equation (5) and (1). The formula for calculating the composition is derived in 3.1.4.

Table 4.1 Composition of isotonic citrate-phosphate buffer solution with an osmotic concentration of 280 mosmol/L.

pH	$c(Na_2HPO_4)$ in mol/L	c(citric acid) in mol/L
3.0	0.064	0.123
5.0	0.099	0.047
6.0	0.107	0.031
7.4	0.118	0.006

4.3 Syntheses

4.3.1 Synthesis of (2-nitro-1,4-phenylene)dimethanol (**2**)

2
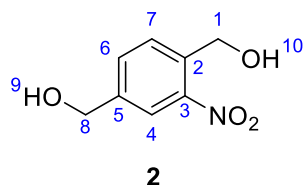
Nitroterephthalic acid (**1**, 2.11 g, 10.0 mmol) was dissolved in 10 mL anhydrous THF in a dry SCHLENK flask under argon atmosphere and cooled to 0 °C in an ice bath. $BH_3 \cdot THF$ (1M, 50 mL, 5 eq, 50 mmol) was added carefully. The reaction was allowed to warm up to room temperature and then stirred at 40 °C for 16 h. The reaction was stopped by addition of water and the volume was reduced to 1/10 by rotary evaporation. The mixture was transferred to a separating funnel and 50 mL of water was added. The aqueous phase was extracted three times with 50 mL of Et_2O. Combined organic layers were washed with saturated $NaHCO_3$ solution and brine respectively and dried over Na_2SO_3. The solvent was removed by rotary evaporation and the crude product was recrystallized from $CHCl_3$. Product **2** was isolated as colorless needles in a yield of 74 % (1.35 g).

^{1}H NMR (DMSO-d_6) δ [ppm]: 4.59 (d, $^3J_{HH}$ = 5.7 Hz, 2H, $^1CH_2$), 4.80 (d, $^3J_{HH}$ = 5.6 Hz, 2H, $^8CH_2$), 5.43 (t, $^3J_{HH}$ = 5.7 Hz, 1H, ^9OH), 5.48 (t, $^3J_{HH}$ = 5.7 Hz, 1H, ^{10}OH), 7.68 (dd, $^4J_{HH}$ = 1.7 Hz, $^3J_{HH}$ = 8.0 Hz, 1H, ^6CH) 7.97 (d, $^3J_{HH}$ = 8.0 Hz, 1H, ^7CH) 7.97 (s, 1H, ^4CH)

HR-MS (ESI) [M + H$^+$]: calc.: 183.0532, found: 183,0558

R_f (DCM:MeOH = 9:1) = 0.30

T_m = 90.5 °C

$\lambda_{abs.,max}$ = 260 nm

4.3.2 Synthesis of PPADK (**3**)

3
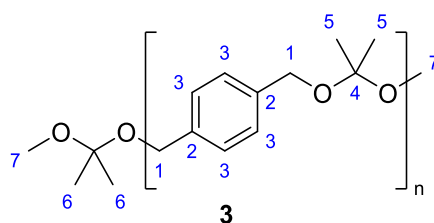
In a 25 mL round bottom flask with VIGREUX column and micro distill, 1,4-benzenedimethanol (**1**, 1.00 g, 1 eq, 7.30 mmol), PTSA (7 mg, 0.05 eq, 0.037 mmol) and 15 mL dry benzene were heated to 80 °C. Dimethoxy propane (0.9 mL, 1 eq, 7.30 mmol) was added and temperature

was risen to slowly distill of methanol. Dimethoxy propane (0.2 mL, 0.22 eq, 1.62 mmol) and 2 mL of dry benzene were added every hour for 6 h. The reaction mixture was cooled down and 0.1 mL of Et_3N was added to stop the reaction. The residual oil was diluted with 3 mL of THF and precipitated into 50 mL MeOH. The precipitate was dissolved in THF and precipitated in methanol twice. The product was dried in high vacuum and 1.05 g **3** was isolated as a white powder in a yield of 82 %.

^{1}H NMR (CDCl₃, Et₃N) δ [ppm]: 1.43 (s, 6H, [6]CH₃), 1.52 (s, 6H, [5]CH₃)₂), 3.26 (s, 3H, [7]CH₃), 4.57 (s, 4H, [1]CH₂), 7.33 (s, 4H, [3]CH)

M_n (THF-SEC, PS-calib.): 5 000 g/mol ($Đ$ = 1.59)

M_n (^{1}H NMR, CDCl₃) = 4 450 g/mol

$\lambda_{abs.,max}$ = 265 nm

4.3.3 Synthesis of oNB PPADK (**4**)

4
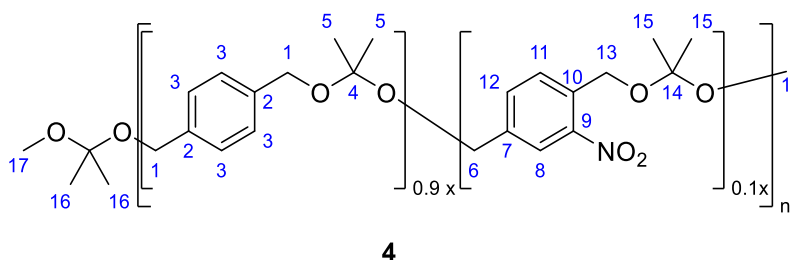
In a 25 mL round bottom flask with VIGREUX column and micro distill, oNB monomer **2** (0.134 g, 0.1 eq, 0.73 mmol), 1,4-benzenedimethanol (**1**, 0.957 g, 0.9 eq, 6.57 mmol), PTSA (7 mg, 0.05 eq, 0.037 mmol) and 15 mL dry benzene were heated to 80 °C. Dimethoxy propane (0.9 mL, 1 eq, 7.30 mmol) was added and temperature was risen to slowly distill of methanol. Dimethoxy propane (0.2 mL, 0.22 eq, 1.62 mmol) and 2 mL of dry benzene were added hourly for 6 h. The reaction mixture was cooled down and 0.1 mL of Et_3N was added to stop the reaction. The residual oil was diluted with 3 mL of THF and precipitated into 50 mL MeOH. The precipitate was dissolved in THF and precipitated in methanol twice. The product was dried in high vacuum and product **4** was isolated as a white powder in a yield of 79 % (1.03 g).

^{1}H NMR (CDCl₃, Et₃N) δ [ppm]: 1.41 (s, 6H, [16]CH₃), 1.50 (s, 6H, [5]CH₃), 1.51 (s, 6H, [15]CH₃), 3.24 (s, 3H, [17]CH₃), 4.50 – 4.73 (m, 4H, [1]CH, [6]CH, [13]CH), 7.31 (m, 4H, [3]CH), 7.57 (d, [3]J_{HH} = 8.1 Hz, 1H, [12]CH), 7.79 (d, [3]J_{HH} = 8.0 Hz, 1H, [11]CH), 8.03 (s, 1H, [8]CH)

M_n (THF-SEC, PS-calib.): 4 800 g/mol ($Đ$ = 1.56)

M_n (^{1}H NMR, CDCl$_3$) = 5 300 g/mol

$\lambda_{abs.,max}$ = 265 nm; $\lambda_{abs,local}$ = 320 nm

4.3.4 Synthesis of 5-(2-hydroxyethoxy)-2-nitrobenzaldehyde (**6**)

6
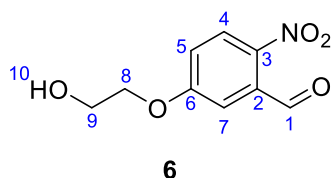
2-Hydroxy-6-nitrobenzaldehyde (**5**, 3.00 g, 18.0 mmol) was dissolved in anhydrous ACN and deprotonated by addition of potassium carbonate (2.76 g, 1.2 eq, 21.6 mmol) and refluxed for 1 h. 2-Bromoethanol (1.91 mL, 1.5 eq, 27.0 mmol) was added to the orange suspension and the reaction was stirred for 16 h at 70 °C. After the reaction cooled down, the mixture was filtered, and the filter cake was rinsed with EtOAc three times. ACN was removed by rotary evaporation and the residual oil was solved in ethyl acetate. The organic phase was washed with 1M HCl, twice with water and once with brine and dried over Na$_2$SO$_4$. The solvent was removed by rotary evaporation. 4.93 g of the crude product **6** was isolated as a yellow oil and used in the next step without further purification.

^{1}H NMR (DMSO-d_6) δ [ppm]: 3.75 (q, $^3J_{HH}$ = 5.0 Hz, 2H, ^{9}CH$_2$), 4.20 (t, $^3J_{HH}$ = 4.8 Hz, 2H, ^{8}CH$_2$), 4.95 (t, $^3J_{HH}$ = 5.5 Hz, 1H, ^{10}OH), 7.26 (d, $^4J_{HH}$ = 2.9 Hz, 1H, ^{7}CH$_2$), 7.36 (dd, $^4J_{HH}$ = 2.9 Hz, $^3J_{HH}$ = 9.1 Hz, 1H, ^{5}CH$_2$), 8.17 (d, $^3J_{HH}$ = 9.0 Hz, 1H, ^{4}CH$_2$), 10.29 (s, 1H, ^{1}CHO)

R_f (EtOAc:iHex = 2:1) = 0.27

4.3.5 Synthesis of 2-(3-(hydroxymethyl)-4-nitrophenoxy)ethan-1-ol (**7**)

7
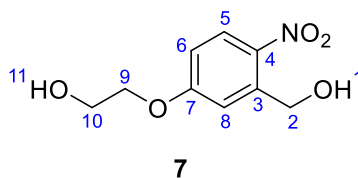
5-(2-hydroxyethoxy)-2-nitrobenzaldehyde (**6**, 4.90 g) as crude product from the previous reaction was solved in 115 mL dry MeOH and cooled in an ice bath. Under strong stirring NaBH$_4$ (1.79 g, 43.6 mmol, 2 eq) was added in small portions. The reaction was stirred at 0 °C for 1 h and then allowed to warm up to room temperature. After 2 h, the excess reducing agent was quenched by addition of 1M HCl. Methanol was removed by rotary evaporation and EtOAc was added. The organic layer was washed with water, saturated NaHCO$_3$ and brine solution. The organic layer was dried with Na$_2$SO$_4$ and solvent was removed by rotary

evaporation. The crude product was purified by column chromatography using a DCM:MeOH gradient 100:1 -> 10:1. 2.66 g of pure product **7** was isolated in a yield of 70 % over two steps as colorless needles.

¹H NMR (DMSO-d_6) δ [ppm]: 3.75 (q, $^3J_{HH}$ = 5.1 Hz, 2H, $^{10}CH_2$), 4.13 (t, $^3J_{HH}$ = 4.9 Hz, 2H, $^9CH_2$), 4.85 (d, $^3J_{HH}$ = 5.6 Hz, 2H, $^2CH_2$),4.92 (t, $^3J_{HH}$ = 5.5 Hz, 1H, ^{11}OH), 5.55 (t, $^3J_{HH}$ = 5.6 Hz, 1H, ^1OH), 7.03 (dd, $^4J_{HH}$ = 2.9 Hz, $^3J_{HH}$ = 9.4 Hz, 1H, $^6CH_2$), 7.35 (d, $^3J_{HH}$ = 2.9 Hz, 1H, $^8CH_2$), 8.12 (d, $^3J_{HH}$ = 9.0 Hz, 1H, $^5CH_2$)

R_f (DCM:MeOH = 10:1) = 0.32

$\lambda_{abs.,max}$ = 310 nm

4.3.6 Synthesis of 2-(2-(2-methoxyethoxy)ethoxy)ethyl-3-(bis(2-hydroxyethyl)amino)propanoate (**11**)

11
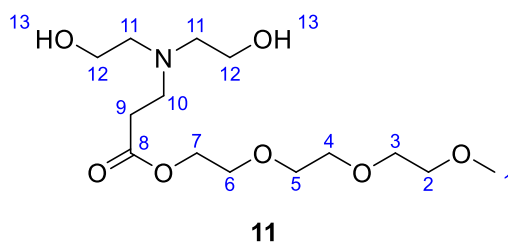
Diethanolamine (**8**, 700 mg, 1 eq, 6.66 mmol) were solved in 20 mL dry DCM in a dry SCHLENK tube under argon atmosphere. 2-[2-(2-Methoxyethoxy)ethoxy]ethyl acrylate (**9**, 1.60 g, 1.51 mL, 1.1 eq, 7.32 mmol) were added and the reaction was stirred at 40 °C for 3 d. The ACN was removed by rotary evaporation and 50 mL of DCM was added. The organic layer was washed with brine and dried over MgSO$_4$. Organic solvent was removed by rotary evaporation. The crude product was purified by column chromatography (MeOH:DCM:Et$_3$N = 5:89:1). Product **11** (0.70 g) was isolated as a yellow oil in a yield of 33 %.

¹H NMR (DMSO-d_6) δ [ppm]: 2.43 (t, $^3J_{HH}$ = 7.0 Hz, 2H, $^9CH_2$), 2.52 (t, $^3J_{HH}$ = 6.2 Hz, 4H, $^{11}CH_2$), 2.78 (t, $^3J_{HH}$ = 7.0 Hz, 2H, $^{10}CH_2$), 3.24 (s, 3H, $^1CH_3$), 3.37 – 3.45 (m, 6H, $^2CH_2$, $^{12}CH_2$), 3.49 – 3.55 (m, 6H, $^3CH_2$, $^4CH_2$, $^5CH_2$), 3.59 (m, 2H, $^6CH_2$), 4.11 (m, 2H, $^7CH_2$), 4.26 (br, 2H, ^{13}OH)

¹³C NMR (DMSO-d_6) δ [ppm]: 32.6 ($^9CH_2$), 50.6 ($^{10}CH_2$), 56.7 ($^{11}CH_2$), 58.5 ($^1CH_2$), 59.7 ($^{12}CH_2$), 63.6 ($^7CH_2$), 68.8 ($^6CH_2$), 70.1 ($^5CH_2$), 70.2 ($^4CH_2$), 70.3 ($^3CH_2$), 71.8 ($^2CH_2$), 172.6 ($^8CH_2$)
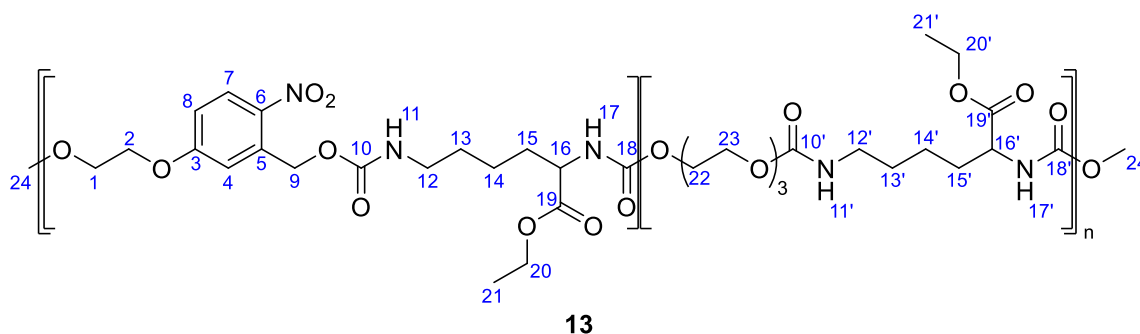
4.3.7 Synthesis of lrPU 1 (**12**)
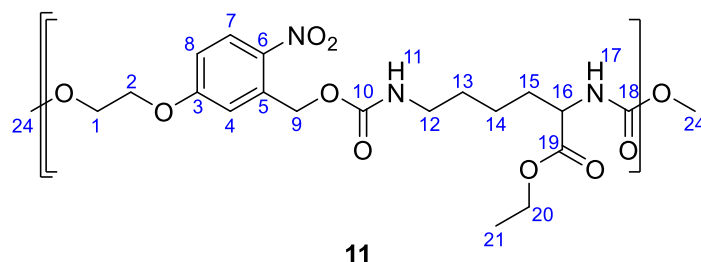
11

In a dry SCHLENK tube under argon atmosphere 213.2 mg fresh recrystallized oNB monomer **7** (1 eq, 1 mmol) were solved in 2.1 mL dry DMF. LDI (237.7 mg, 1.05 eq, 1.05 mmol) and DBTL (6 mol%, 36.8 mg, 0.058 mmol) were added and the reaction was stirred at 50 °C for 18 h. 1 mL of dry MeOH was added and the reaction was stirred for 1 h. The reaction mixture was cooled down and precipitated into cold methanol. Supernatant was removed by centrifugation and precipitation from THF into MeOH was carried out twice. The precipitate was dried in high vacuum and 332.8 mg of polymer **11** was isolated in a yield of 74 %.

¹H NMR (DMSO-d_6) δ [ppm]: 1.03-1.20 (br, $^{21}CH_3$), 1.21-1.48 (br, $^{13}CH_2$, $^{14}CH_2$), 1.48-1.80 (br, $^{15}CH_2$), 2.86-3.07 (br, $^{12}CH_2$), 3.87-4.15 (br, ^{16}CH, $^{20}CH_2$), 4.20-4.42 (br, $^{1}CH_2$, $^{2}CH_2$), 5.15-5.55 (br, $^{9}CH_2$), 5.06-8.30 (br, ^{7}CH, ^{8}CH, ^{11}NH, ^{17}NH, ^{4}CH)

M_n (THF-SEC, PS-calib.): 5 900 g/mol ($Đ$ = 1.33)

$\lambda_{abs.,max}$ = 310 nm

4.3.8 Synthesis of lrPU 2 (**13**)

13

In a dry SCHLENK tube under argon atmosphere 213.2 mg fresh recrystallized oNB monomer **7** (1 eq, 1 mmol) were solved in 2.1 mL dry DMF. LDI (237.7 mg, 1.05 eq, 1.05 mmol) and DBTL (6 mol%, 36.8 mg, 0.058 mmol) were added and the reaction was stirred at 50 °C for 18 h. 1 mL of dry MeOH was added and the reaction was stirred for 1 h. The reaction mixture was cooled down and precipitated into cold methanol. Supernatant was removed by centrifugation and precipitation from THF into MeOH was carried out twice. The precipitate was dried in high vacuum and 248.9 mg of polymer **13** was isolated in a yield of 74 %.

¹H NMR (DMSO-d_6) δ [ppm]: 1.03-1.20 (br, $^{21}CH_3$, $^{21'}CH_3$), 1.21-1.48 (br, $^{13}CH_2$, $^{14}CH_2$, $^{13'}CH_2$, $^{14'}CH_2$), 1.48-1.74 (br, $^{15}CH_2$, $^{15'}CH_2$), 2.90-3.07 (br, $^{12}CH_2$, $^{12'}CH_2$), 3.44-3.48 (br, $^{22}CH_2$, $^{23}CH_2$), 3.87-4.15 (br, ^{16}CH, $^{20}CH_2$, $^{16'}CH$, $^{20'}CH_2$), 4.20-4.42 (br, $^{1}CH_2$, $^{2}CH_2$), 5.29-5.52 (br, $^{9}CH_2$), 5.06-8.30 (br, ^{7}CH, ^{8}CH, ^{11}NH, ^{17}NH, ^{11}NH, ^{17}NH)

M_n (THF-SEC, PS-calib.): 8 400 g/mol (Đ = 1.69)

$\lambda_{abs.,max}$ = 310 nm

4.3.9 Synthesis of lrPU 3 (**14**)

14
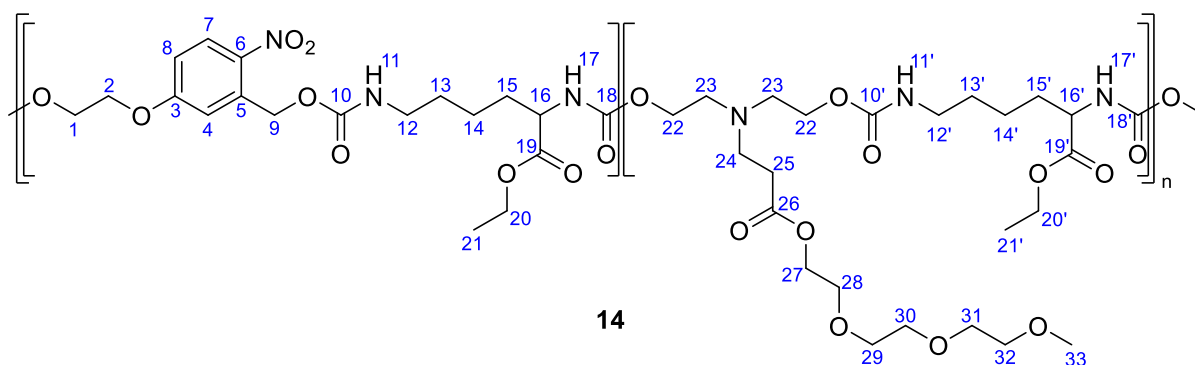
In a dry schlenk tube under argon atmosphere fresh recrystallized oNB monomer **7** (213.2 mg, 0.5 eq, 0.5 mmol), linker **11** (0.5 eq, 0.5 mmol) were solved in 2.05 mL dry DMF. 237.5 mg LDI (237.5 mg, 1.05 eq, 1.05 mmol) and DBTL (6 mol%, 36.5mg, 0.058 mmol) were added and the reaction was stirred at 50 °C for 18 h. 1 mL of dry MeOH was added and the reaction was stirred for 1 h. The reaction mixture was cooled down and precipitated into cold diethylether. Supernatant was removed by centrifugation and precipitation from THF into diethylether was carried out twice. The precipitate was dried in high vacuum and 328.8 mg of polymer **14** was isolated in a yield of 65 %.

¹H NMR (DMSO-d_6) δ [ppm]: 1.03-1.20 (br, $^{21}CH_3$, $^{21'}CH_3$), 1.21-1.48 (br, $^{13}CH_2$, $^{14}CH_2$, $^{13'}CH_2$, $^{14'}CH_2$), 1.48-1.80 (br, $^{15}CH_2$, $^{15'}CH_2$), 2.34-2.46 (br, $^{25}CH_2$), 2.60-2.72 (br, $^{23}CH_2$), 2.74-2.83 (br, $^{24}CH_2$), 2.90-3.06 (br, $^{12}CH_2$, $^{12'}CH_2$), 3.20-3.26 (br, $^{33}CH_3$), 3.39-3.46 (br, $^{22}CH_2$, $^{32}CH_2$), 3.46-3.55 (br, $^{29}CH_2$, $^{30}CH_2$, $^{31}CH_2$), 3.55-3.66 (br, $^{28}CH_2$), 3.84-4.20 (br, ^{16}CH, $^{20}CH_2$, $^{16'}CH$, $^{20'}CH_2$, $^{27}CH_2$), 4.20-4.38 (br, $^{1}CH_2$, $^{2}CH_2$), 5.15-5.55 (br, $^{9}CH_2$), 5.66-8.30 (br, ^{7}CH, ^{8}CH, ^{11}NH, $^{11'}NH$, ^{17}NH, $^{17'}NH$, ^{4}CH)

M_n (THF-SEC, PS-calib.): 12 800 g/mol (Đ = 2.34)

$\lambda_{abs.,max}$ = 310 nm

## 4.3.10 Synthesis of 6-bromo-4-(chloromethyl)-7-hydroxy-2H-chromen-2-one (**19**)

19
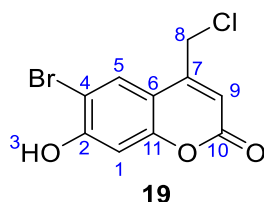
In a one-necked round bottom flask in a water bath, 10 g 4-bromoresorcin (52.9 mmol, 1 eq) were solved in 105 mL methanesufonic acid under strong stirring for 30 min. 9.2 mL methyl 4-chloro-3-oxobutanoate (12.0 g, 79.4 mmol, 1.5 eq) were added slowly and the reaction was stirred for 2 h at room temperature. The reaction mixture was poured onto 300 g of ice to precipitate the crude product. The pale lilac-coloured crude product was isolated by vacuum filtration, washed with ice cold water three times and solved in 300 mL of THF and Na_2SO_4 was added to remove residual water. The drying agent was filtered off and THF was removed by rota evaporation. The crude product **19** was isolated in a yield of 96 %.

¹H NMR (DMSO-d_6) δ [ppm]: 4.99 (d, 2 H, $^3J_{HH}$ = 5,5 Hz, $^8CH_2$), 6.47 (s, 1 H, ^9CH), 6.92 (s, 1 H, ^1CH), 7.99 (s, 1 H, ^5CH), 11.51 (s, 1 H, ^3OH)

R_f (*i*Hex:EE = 2:1) = 0.35

4.3.11 Synthesis of 6-bromo-7-hydroxy-4-(hydroxymethyl)-2H-chromen-2-one (**20**)


20
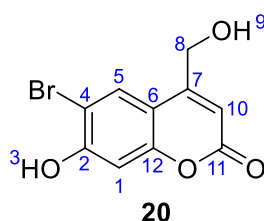
5.07 g 6-bromo-4-(chloromethyl)-7-hydroxy-2H-chromen-2-one (**19**, 17.5 mmol) were dispersed in in 580 mL of water and refluxed. Conversion was monitored by extraction of samples with ethyl acetate and ¹H-NMR spectroscopy. After 10 d full conversion was accomplished. The reaction was allowed to cool down and cooled in an ice bath. The precipitate was filtered of. 4.08 g product (**20**) were isolated in a yield of 80.4 %.

¹H NMR (DMSO-d_6) δ [ppm]: 4.69 (d, 2 H, $^3J_{HH}$ = 5,5 Hz, $^8CH_2$), 5.58 (t, 1 H, $^3J_{HH}$ = 5,5 Hz, ^9OH), 6.27 (s, 1 H, ^{10}CH), 6.89 (s, 1 H, ^1CH), 7.84 (s, 1 H, ^5CH), 11.35 (s, 1 H, ^3OH)

R_f (*i*Hex:EE = 1:1) = 0.24

4.3.12 Synthesis of 6-bromo-7-(2-hydroxyethoxy)-4-(hydroxymethyl)-2H-chromen-2-one (**21**)
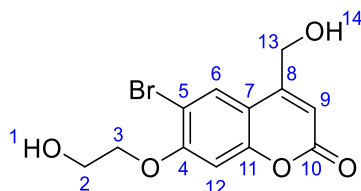

21

3.00 g 6-bromo-7-hydroxy-4-(hydroxymethyl)-2H-chromen-2-one (**20**, 11.1 mmol, 1 eq) and 1.84 g K_2CO_3 (13.3 mmol, 1.2 eq) in 55 mL ACN refluxed for 2 h. 2.4 mL 2-Bromethanol (4.15 g, 33.3 mmol, 3.00 eq) were added and the reaction was stirred for 20 h. After reaction cooled down, 150 mL 1 M HCl was added and the mixture was transferred to a separation funnel. 100 mL water and 500 mL ethyl acetate were added and the phases separated. The aqueous phase was extracted three times with 100 mL ethyl acetate. Combined organic phases were washed with a 1:1 mixture of water and brine once and washed with saturated $NaHCO_3$ solution. Organic phases were dried over $MgSO_4$ and solvent was removed *in vacuuo*. 3.63 g crude product were dissolved in 120 mL boiling THF. Addition of 200 mL *iso*-Hexane precipitated pure product **21** in a yield of 68 %. 2.43 g of the product were isolated as a white powder.

^{1}H NMR (DMSO-d_6) δ [ppm]: 3.77 (q, 2 H, $^3J_{HH}$ = 5,1 Hz, $^2CH_2$), 4.18 (t, 2 H, $^3J_{HH}$ = 4,9 Hz, $^3CH_2$), 4.71 (d, 2 H, $^3J_{HH}$ = 5,5 Hz, $^{13}CH_2$), 4.91 (t, 1 H, $^3J_{HH}$ = 5,5 ^1OH), 5.62 (t, 1 H, $^3J_{HH}$ = 5,5 ^{14}OH), 6.33 (s, 1 H, ^9CH), 7.20(s, 1 H, ^{12}CH), 7.89 (s, 1 H, ^6CH)

R_f (*i*Hex:EE = 1:1) = 0.31

$\lambda_{abs,max}$ = 310 nm

4.3.13   Synthesis of BHC homopolymers **22** – **24**

24
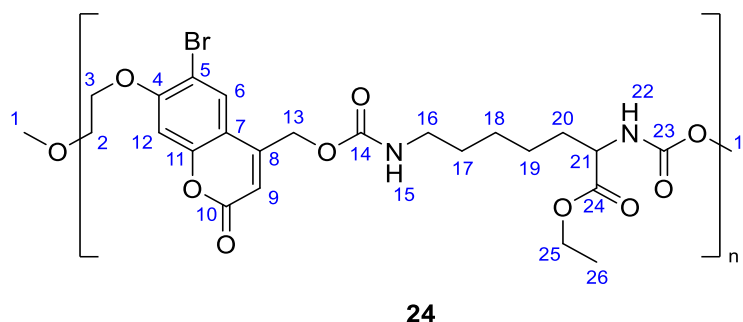
In a typical procedure, anhydrous THF or DMF (1 mL) was placed in a dry Schlenk flask under argon atmosphere. Enough solvent was added so that the concentration of diisocyanate in the reaction mixture was 0.2 mol/L or 0.5 mol/L. Diisocyanate (0.525 mmol, 1.05 eq) 158 mg bromocoumarin monomer **21** (0.500 mmol, 1 eq) and 22.0 mg DBTL catalyst (0.035 mmol, 7 mol%) were added and reaction mixture was stirred for 18 h at 70 °C. 1 mL of methanol was added and reaction was stirred for 1 h and then cooled down to room temperature. The polymer was precipitated into cold methanol, separated by centrifugation and decantation and dried in high vacuum. The isolated yields varied between 69 % and 93 % and the number average molecular weight were determined as 5 700 – 10 300 g/mol and are listed in Table 4.2.

Table 4.2 Average number molar mass (M_n), polydispersities ($Đ$) and yield of the synthesis of BHC-diol (**21**) based polyurethanes **22** – **24**.

Batch	Polymer	M_n	$Đ$	yield
1	BHC-HDI (**22**)	8 900	1.98	74 %
2	BHC-IPDI (**23**)	10 300	1.41	93 %
3	BHC-LDI (**24**)	4 600	1.84	95 %
4	BHC-LDI (**24**)	5 700	1.54	69 %
5	BHC-LDI (**24**)	7 600	1.77	77 %
6	mPEG-BHC-LDI (**25**)	7 200	1.52	22 %

^{1}H NMR BHC-LDI (24) (DMSO-d_6) δ [ppm]: 1.13-1.20 (m, $^{26}CH_3$), 1.20-1.49 (m, $^{18}CH_2$, $^{19}CH_2$), 1.49-1.74 (m, $^{20}CH_2$), 2.83-3.06 (m, $^{16}CH_2$), 3.92-4.14 (m, ^{21}CH, $^{25}CH2$), 4.28-4.42 (m, $^2CH_2$, $^3CH_2$), 5.19-5.39 (m, $^{13}CH_2$), 6.22-6.37 (m, ^9CH), 7.20-7.29 (m, ^{12}CH, ^{22}NH), 7.46-7.54 (m, ^{10}NH), 7.68-7.75 (m, ^{10}NH), 7.89-7.95 (m, ^6CH), 7.95-8.00 (m, ^{22}NH)

$λ_{abs,max}$ = 320 nm

4.3.14   Synthesis of mPEG-BHC-LDI (**25**)
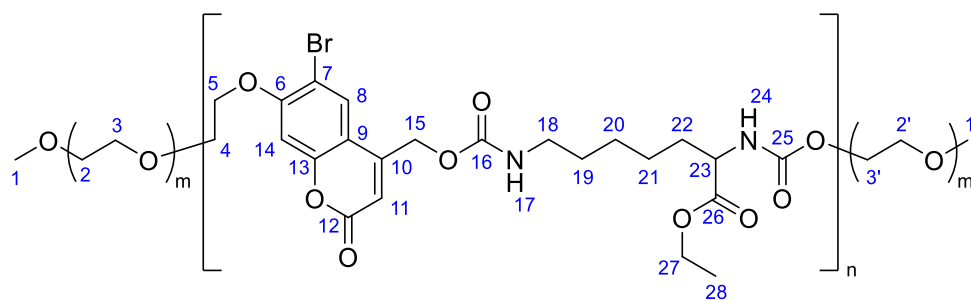
25

Anhydrous DMF (2.5 ml) was placed in a Schlenk flask under an argon atmosphere and the chromophore **21** (150.7 mg; 0.478 mmol) was dissolved in it. LDI (118.8 mg; 0.525 mmol) was then added to the reaction solution. The solution turned slightly brownish in colour. DBTL (16.8 mg; $2.67 \cdot 10^{-2}$ mmol; 2.6 mol%) was added dropwise as catalyst and the reaction solution was stirred for 19 h at 70 °C. 20 µL of the reaction mixture was terminated in 0.5 mL MeOH as a reference and precipitated. mPEG 2000 (239.9 mg; 0.12 mmol) was added to the reaction mixture and stirred for another 3 h. The solution was precipitated in 60 ml MeOH, centrifuged and then dissolved four times in 2.5 ml THF each and precipitated in 100 ml diethyl ether.

A white solid of 58.1 mg (21.5 %) was obtained. The number-average molecular weight was determined as M_n = 7 200 g/mol (Đ = 1.52)

^{1}H NMR (DMSO-d_6) δ [ppm]: 1.13-1.20 (m, ^{28}CH3), 1.20-1.49 (m, ^{19}CH$_2$, ^{20}CH$_2$), 1.49-1.74 (m, ^{22}CH$_2$), 2.83-3.06 (m, ^{18}CH$_2$), 3.51 (s, ^{2}CH$_2$, ^{3}CH$_2$), 3.92-4.14 (m, ^{23}CH, ^{27}CH$_2$), 4.28-4.42 (m, ^{4}CH$_2$, ^{5}CH$_2$), 5.19-5.39 (m, ^{15}CH$_2$), 6.22-6.37 (m, ^{11}CH), 7.20-7.29 (m, ^{14}CH, ^{24}NH), 7.46-7.54 (m, ^{17}NH), 7.68-7.75 (m, ^{17}NH), 7.89-7.95 (m, ^{8}CH), 7.95-8.00 (m, ^{24}NH)

$\lambda_{abs.,max}$ = 320 nm

5 Appendix

5.1 Abbreviations

|	
18-c-6	18-crown-6 ether
ACN	acetonitrile
AF4	asymmetric flow field-flow fractionation
AFM	Atomic force microscopy
API	active pharmaceutical ingredient
AROMP	alternating ring opening metathesis
BHC	bromohydroxycoumarin
CAM	choriollantoic membrane
CMC	critical micell concentration
DAPI	4',6-diamidino-2-phenylindole
DBTL	dibutyltin dilaurate
DCM	dichlormethane
DDS	drug delivery system
DMF	dimethylformamide
DMP	dimethoxypropane
DOPC	phosphatidylcholine lipids
DOPE	phosphatidylcholine lipids
DOX	doxorubicin
DSC	differntial scanning calorimeter
DSPE	phosphatidylcholine lipids
EC50	half maximal effective concentration
ECM	extracellular matrix
Et	ethyl-
EtOAc	ethyl acetate
FDA	food and drug administration
GSH	upper critical solution temperature
HDI	hexamethylene diisocyanate
HFIP	1,1,1,3,3,3-hexafluoropropan-2-ol

HPLC-FLD	high performance liquid chomatography fluresence light detection
HSPC	phosphatidylcholine lipids
*i*Hex	*iso*-hexane
IPDI	isophorone diisocyanate
kcps	kilo counts per second
LCST	lower critical solution temperature
LDI	*L*-lysine diisocyanate
LR	Lumogen® Red
LS	light scattering
MCF-7 cells	michigan cancer foundation - 7 cells
Me	methyl-
MeOH	methanol
mPEG	methoxypolyethylene glycol
NMR	nuclear magnetic resonance
NP	nanoparticle
NR	nile red
OAc	acetate
oNB	*o*-nitrobenzyl
PAH	polycyclic aromatic hydrocarbon
PBS	phosphate buffered saline
PCADK	poly(cyclohexane-1,4 diyl acetone dimethylene ketal)
PDT	photodynamic therapy
PEG	phosphatidylcholine lipids
PK	polyketal
PLA	polylactide
PLGA	poly(lactid-co-glycolid)
PNVP	polyvinylpyrrolidone
PPADK	poly(1,4-phenyleneacetone dimethylene ketal)
PPADT	poly-(1,4-phenyleneacetone dimethylene thioketal)
ppm	parts per million
PS	polystyrene
PTSA	p-toluenesulfonic acid

|	
PVA	polyvinyl alcohol
quant.	quantitative yield
rt	room temperature
SEC	size exclusion chromatography
SIP	selfimmolative polymer
SOD	superoxide dismutase
TEG	triethylenglycol
THF	tetrahydrofuran
TLC	thin layer chromatography
TR-MALS	time resolved multi angle light scattering
Ts	tosyl-
UCNP	upconverting nano particles
UV	ultraviolet
VIS	visible
WST assay	water-soluble tetrazolium assay

5.2 Spectroscopic Data

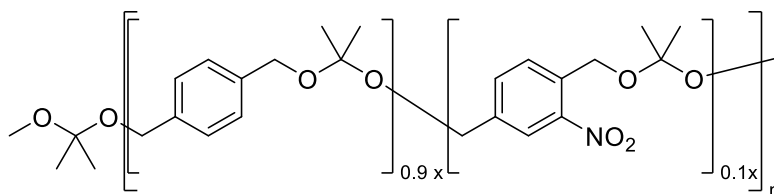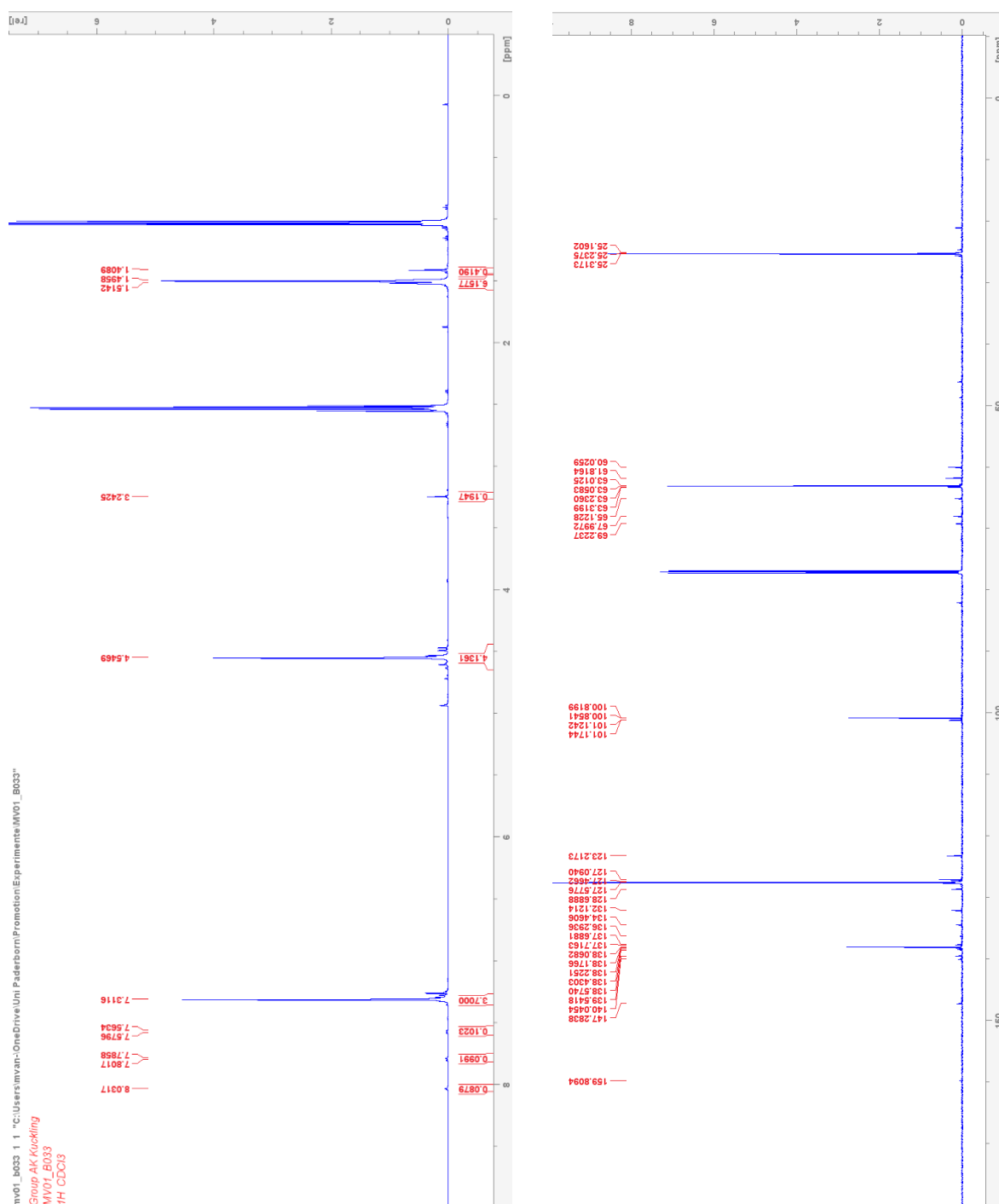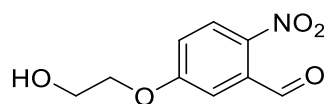## 5.2.1 (2-nitro-1,4-phenylene)dimethanol (**2**)
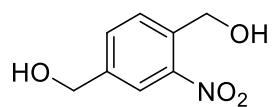
2
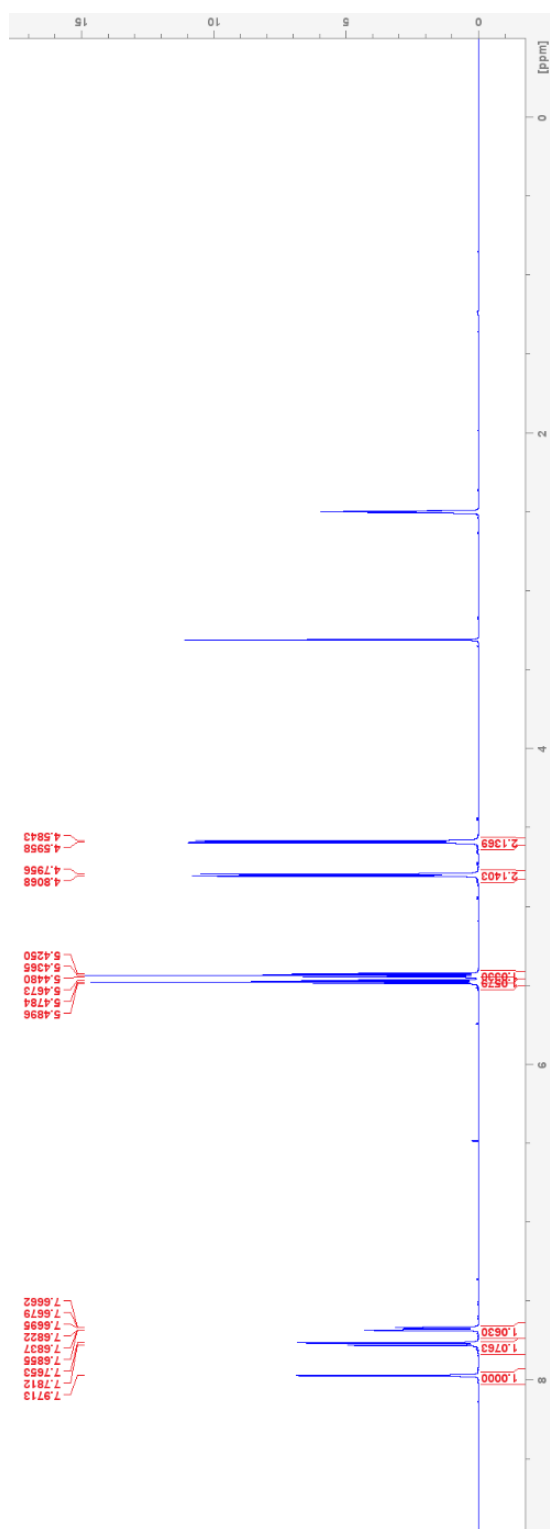
5.2.2 PPADK (**3**)
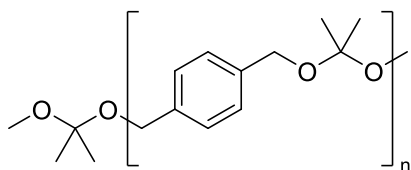
3
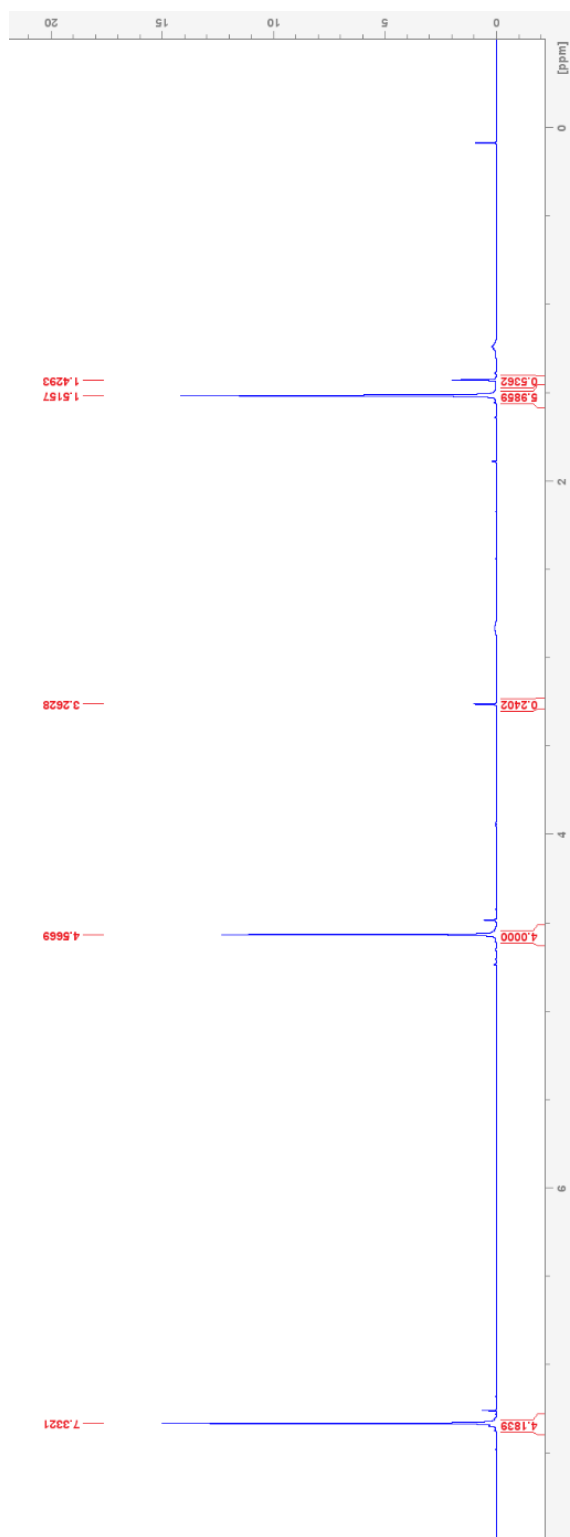
5.2.3 oNB PPADK (**4**)

4

5.2.4 5-(2-hydroxyethoxy)-2-nitrobenzaldehyde (**6**)

6
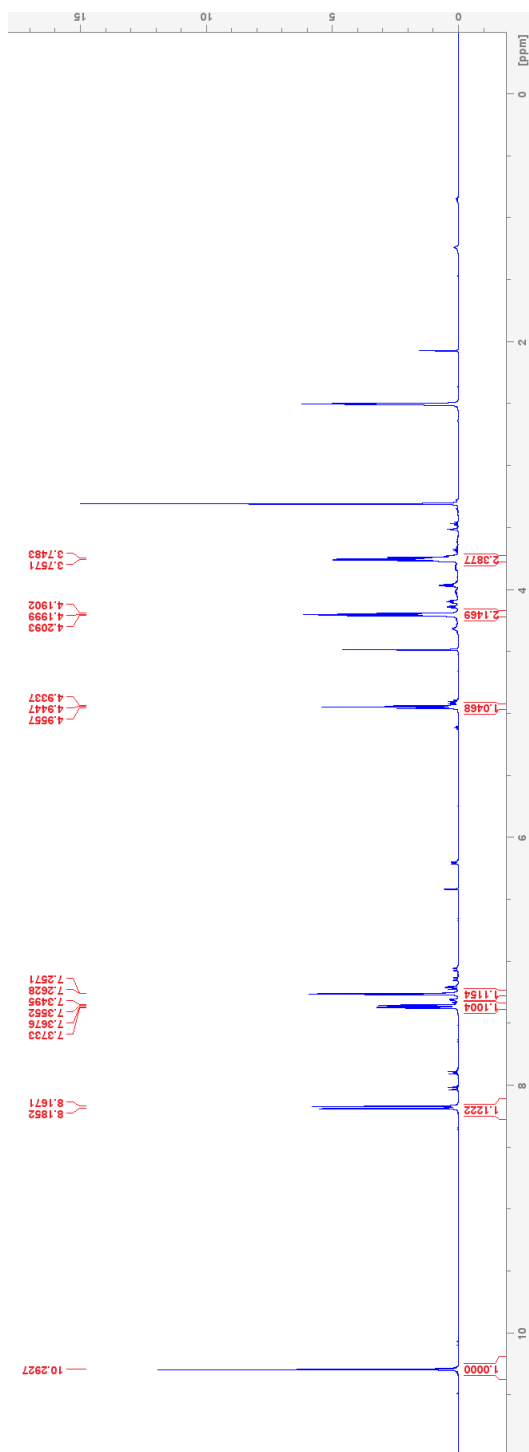
5.2.5 2-(3-(hydroxymethyl)-4-nitrophenoxy)ethan-1-ol (**7**)
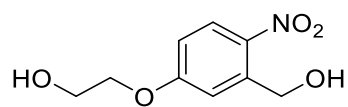
7
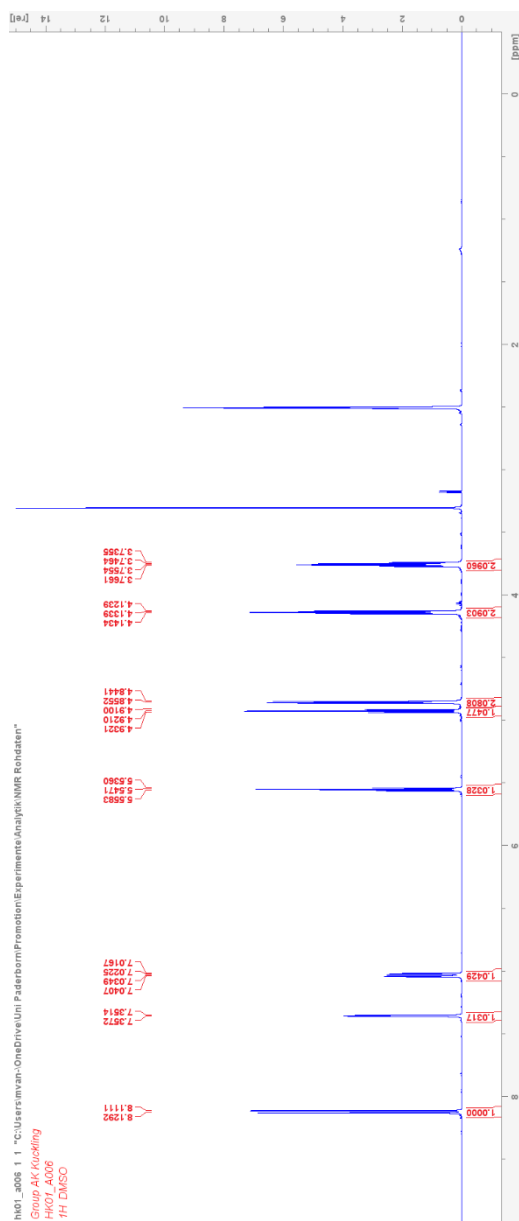
5.2.6 2-(2-(2-methoxyethoxy)ethoxy)ethyl-3-(bis(2-hydroxyethyl)amino)propanoate (**11**)

11

5.2.7 lrPU 1 (**12**)

12

5.2.8 lrPU 2 (**13**)

13
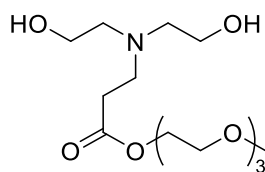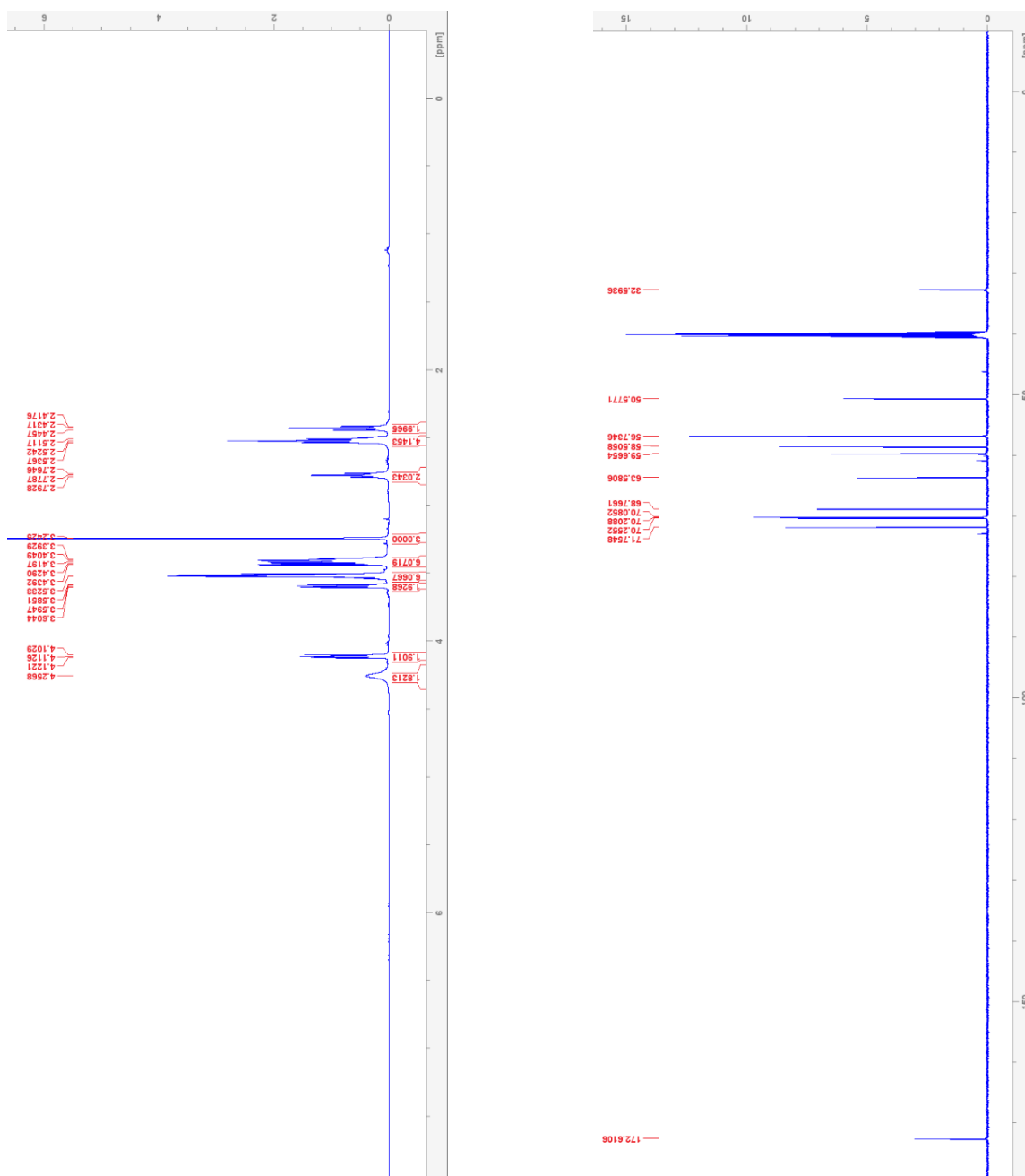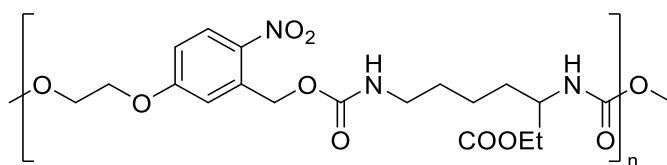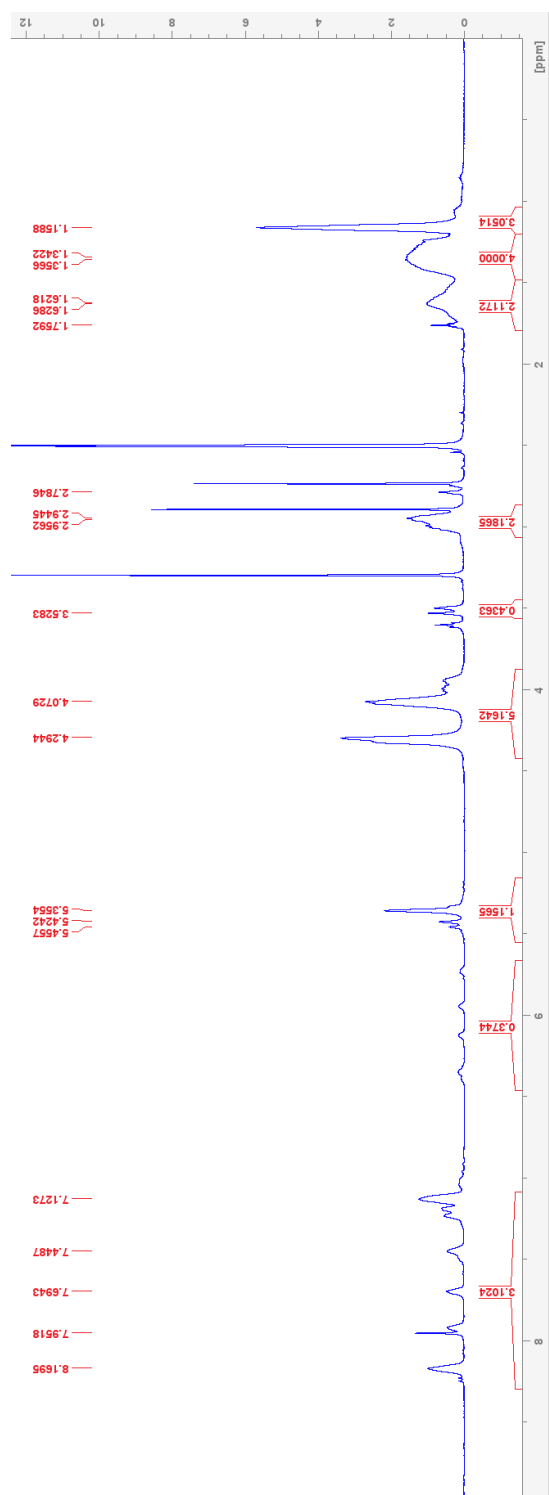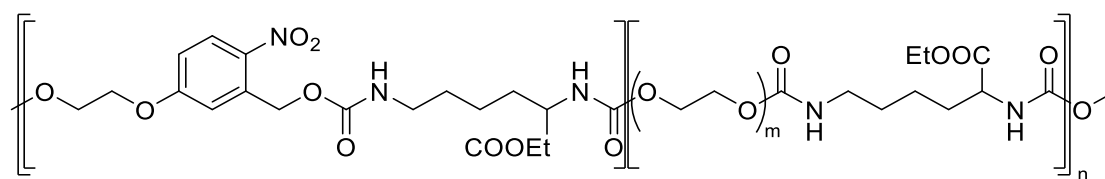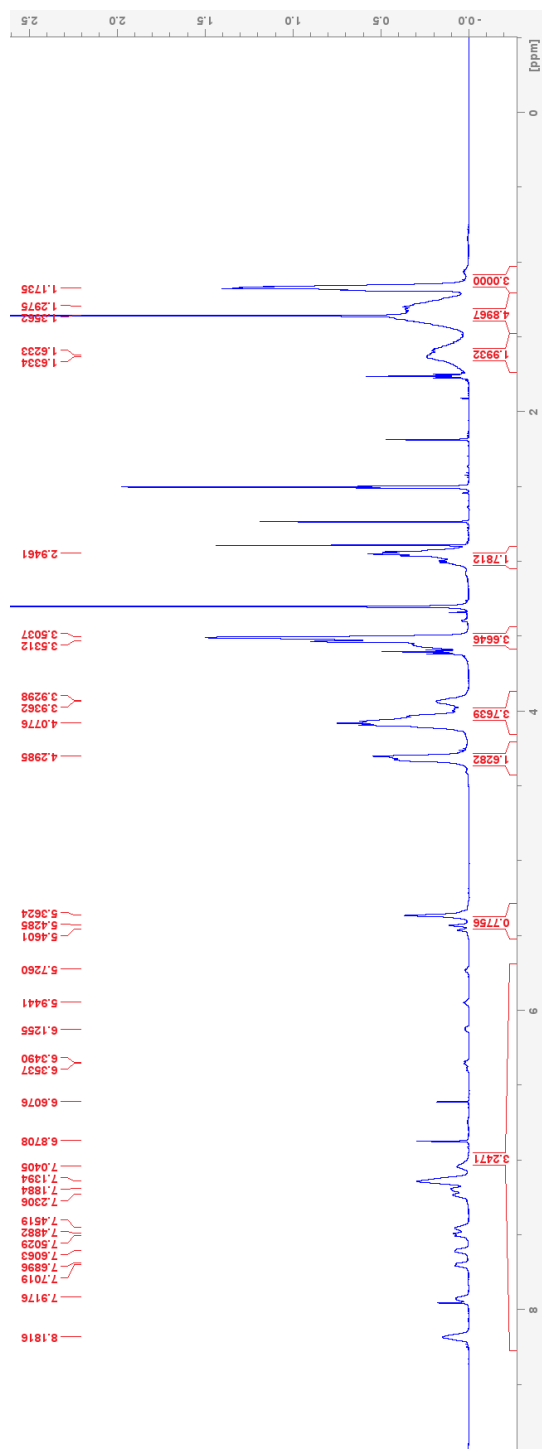
5.2.9 lrPU 3 (**14**)
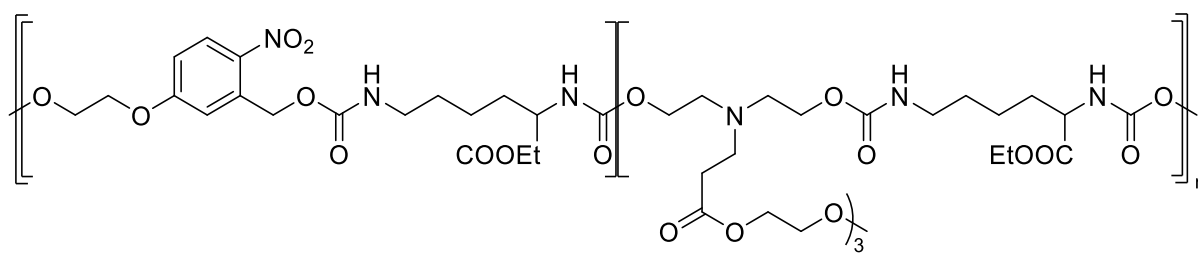
14
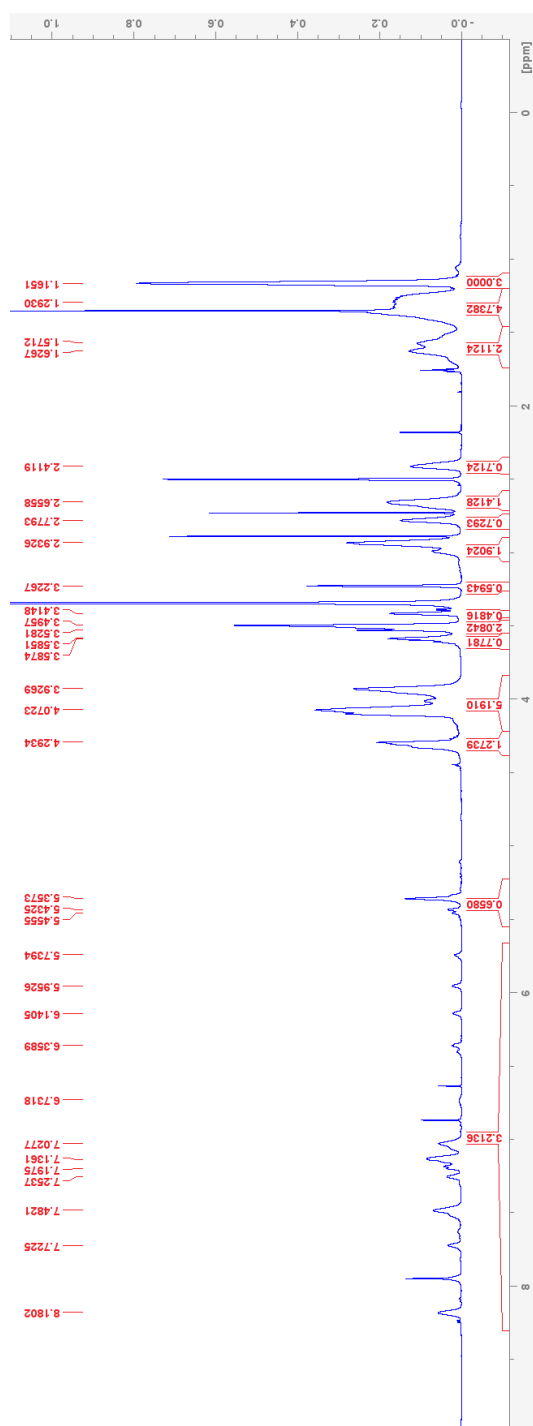
5.2.10   6-bromo-4-(chloromethyl)-7-hydroxy-2H-chromen-2-one (**19**)

19
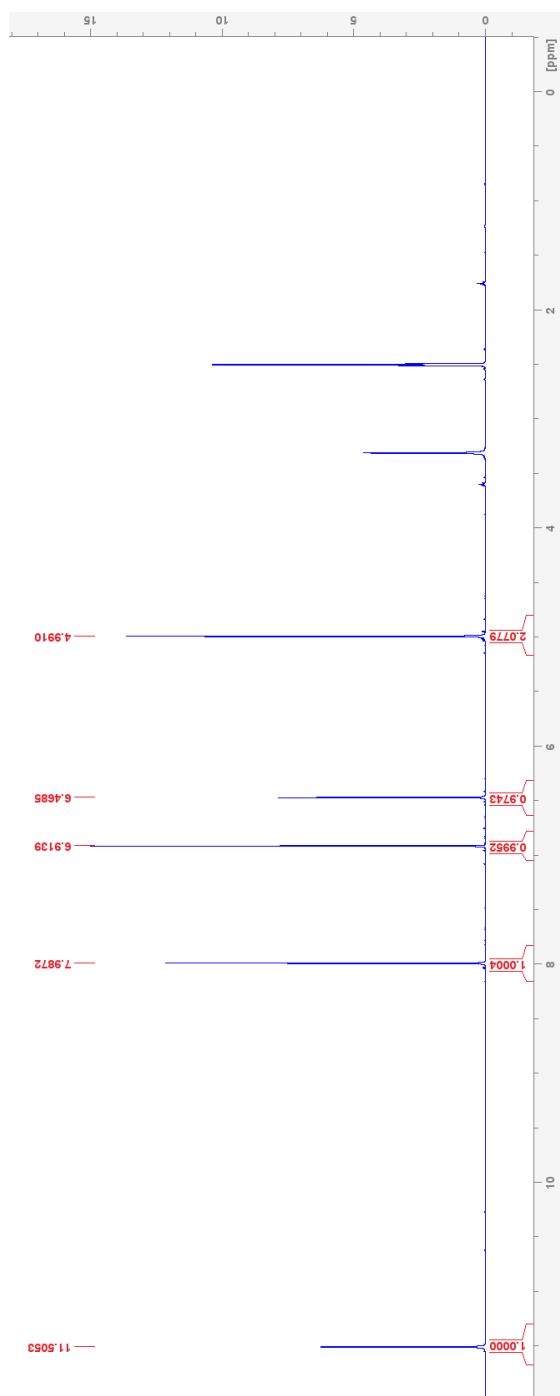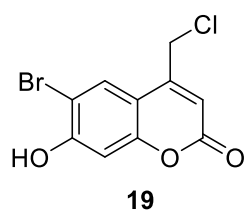
5.2.11 6-bromo-7-hydroxy-4-(hydroxymethyl)-2H-chromen-2-one (**20**)
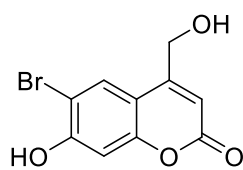
20
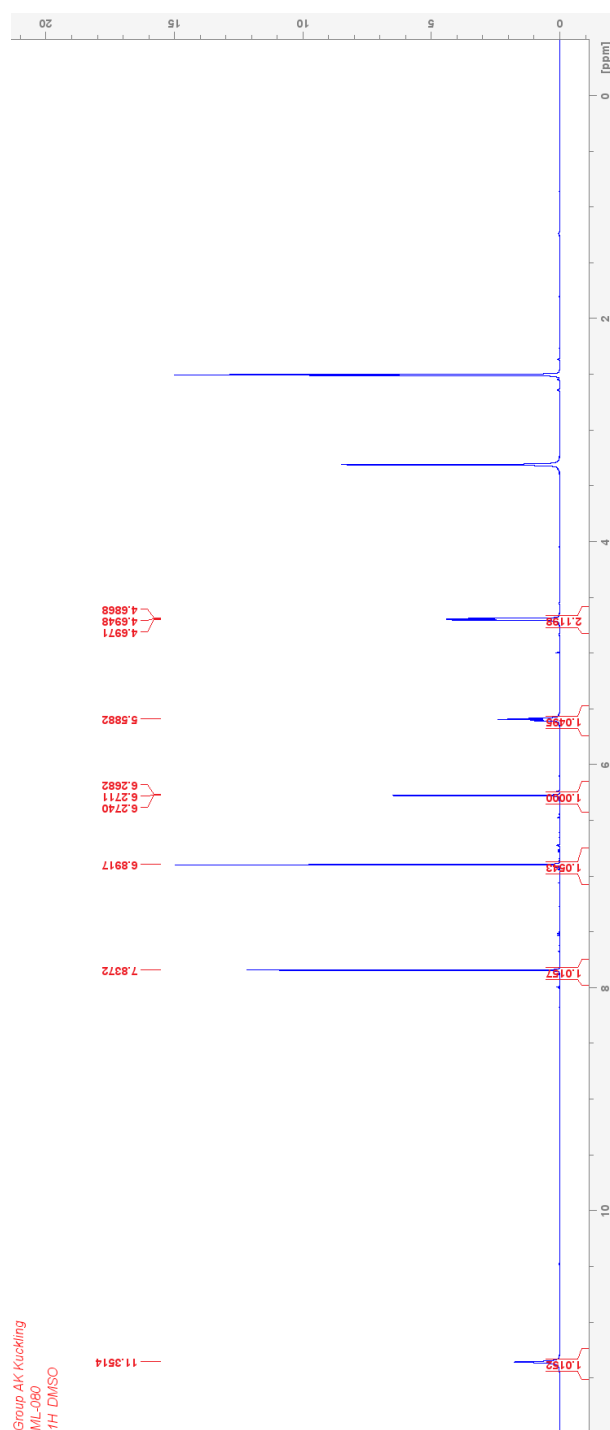
5.2.12   6-bromo-7-(2-hydroxyethoxy)-4-(hydroxymethyl)-2H-chromen-2-one (**21**)
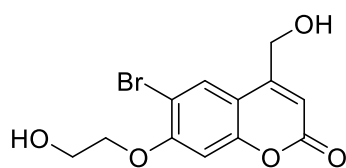
21
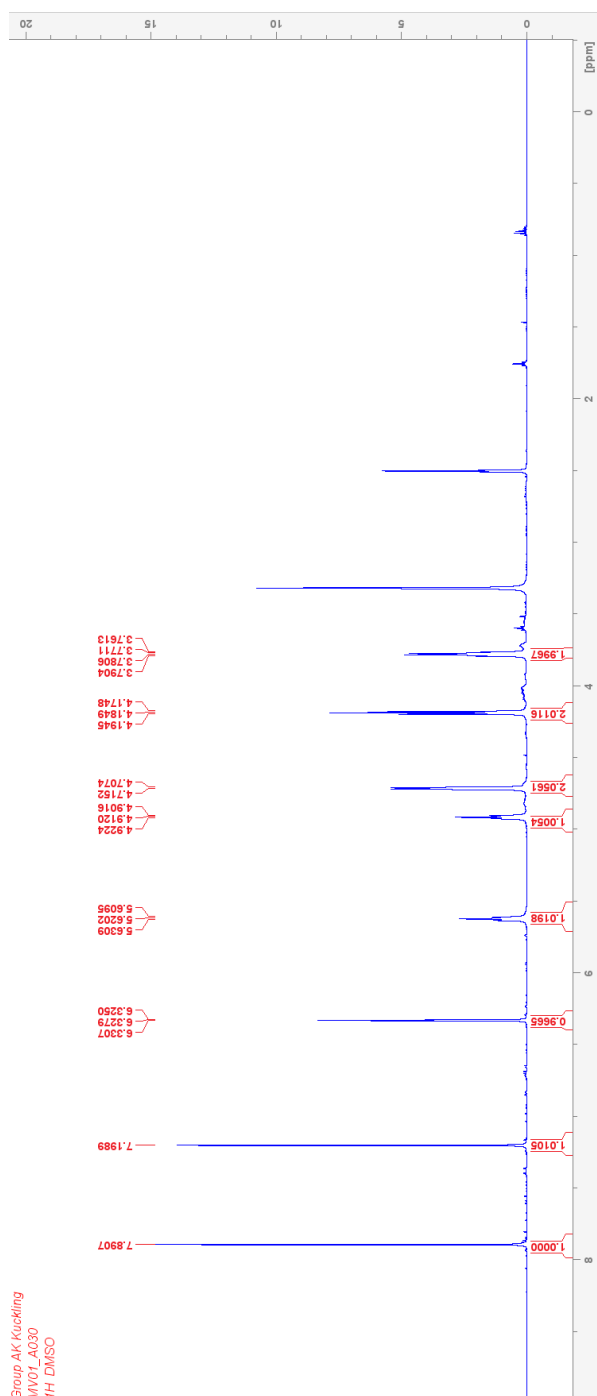
5.2.13   BHC-LDI (**24**)
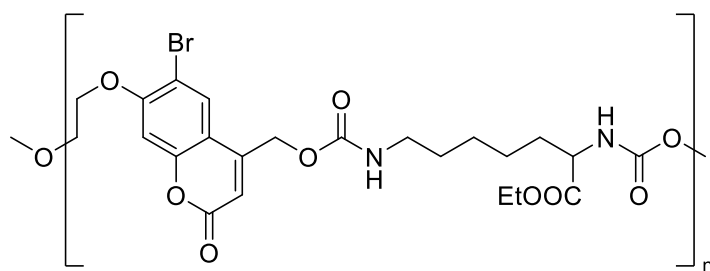
24
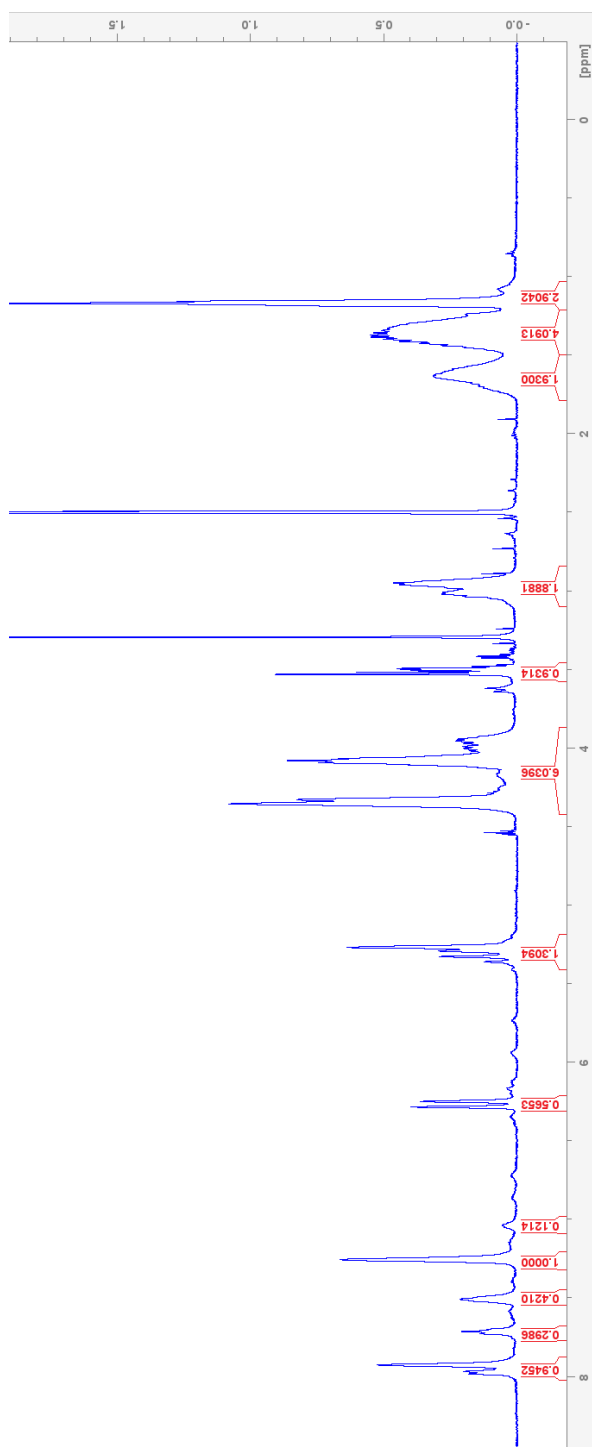
5.2.14 mPEG-BHC-LDI (**25**)

25

5.3 DSC-Data

5.3.1 lrPU 1 (**12**)

DSC /(mW/mg)　　　　　　　　　　　　　　　　　　　Durchfluss /(ml/min)

↓ exo

Run: T= -10°C to 240°C/ 10K/min

Kompl.Peakausw:
Fläche:　1.795 J/g
Peak*:　71.3 °C
Onset:　63.8 °C
Ende:　76.1 °C

Kompl.Peakausw:
Fläche:　0.03194 J/g
Peak*:　32.6 °C
Ende:　34.3 °C

Temperatur /°C

5.3.2 lrPU 2 (**13**)

DSC /(mW/mg)　　　　　　　　　　　　　　　　　　　Durchfluss /(ml/min)

↓ exo

-10°C to 240°C/ 10K/ min

Kompl.Peakausw:
Fläche:　-1.411 J/g
Peak*:　19.1 °C
Onset:　6.9 °C
Ende:　30.7 °C

Temperatur /°C

5.3.3 lrPU 3 (**14**)

DSC /(µV/mg)

Gasdurchfluss /(ml/min)

↓ Exo

-10°C to 220°/ 10K/ min

Kompl.Peak:
Fläche: 196.7 µVs/mg
Peak*: 113.4 °C
Onset: 104.9 °C
Ende: 117.1 °C
Breite: 15.0 °C(37.000 %)
Höhe: 2.4658 µV/mg

Temperatur /°C

5.4 DLS-Data

5.4.1 PPADK

5.4.2 oNB PPADK
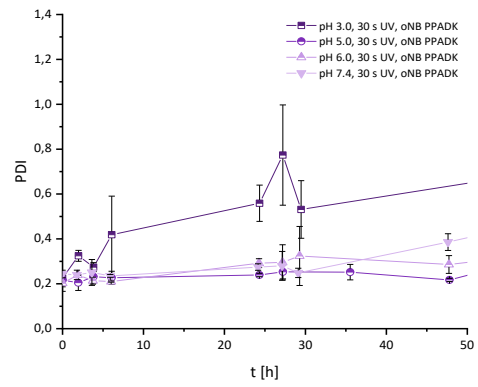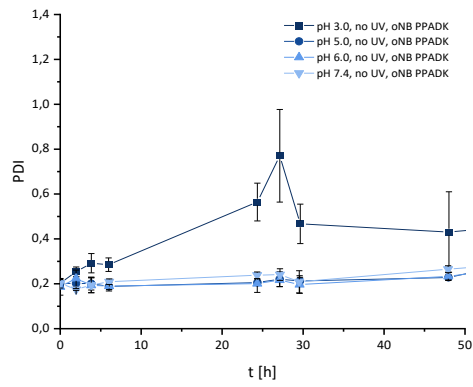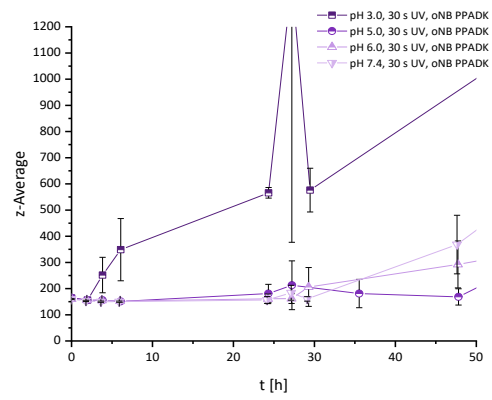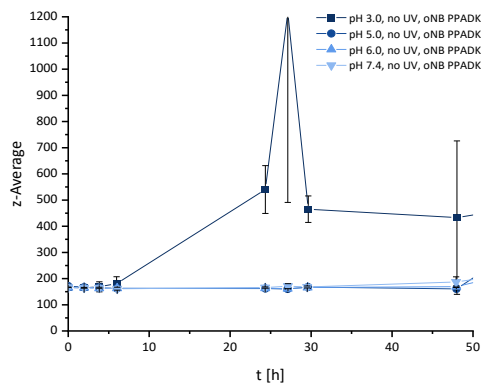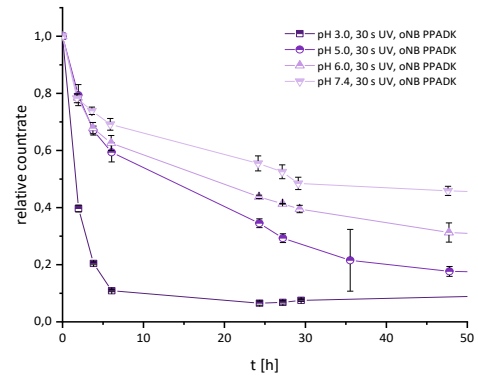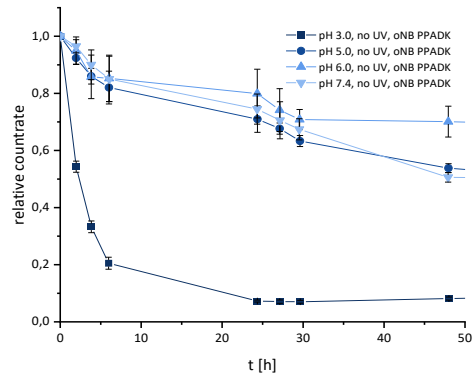
Danksagung

Diese Arbeit zu einem erfolgreichen Ende zu bringen war das Werk vieler Personen, die mich auf diesem Weg begleitet und unterstützt haben. Zunächst danke ich Herrn Prof. Dr. Dirk Kuckling, der mich mit diesem spannenden Thema betraut hat, mir die Freiheiten und das Vertrauen zum Erkunden neuer Ideen gab. Herrn Prof. Dr. Klaus Langer danke ich für die bereitwillige Übernahme des Zweitgutachtens.

Bei Prof. Dr. Sabine Fechner und PD Hans Egold bedanke ich mich dafür, dass sie sich bereiterklärt haben, das Ende dieser Promotion als Teilnehmer der Prüfungskommission zu begleiten. Ebenso möchte ich mich bei den Mitarbeitern der Uni Paderborn bedanken, die mich vor Ort unterstützt haben: bei Dr. Artjom Herberg, für seinen kritischen Blick und der Hilfestellung rund um die GPC, bei dem Team der Analytik, Herr PD Dr. Hans Egold, Karin Stolte, Andrea Harbath und Christiane Gloger. Annette Lefarth, Daniela Kästing, Claudia Berkemeier und Mariola Zukowski bedanke ich mich für den reibungslosen Betrieb rund ums Labor und der Verwaltung.

Des Weiteren möchte ich mich bei allen aktuellen und ehemaligen Mitarbeitern des AK Kuckling bedanken, die mich auf dem langen Weg begleitet und Freud und Leid mit mir geteilt haben. Insbesondere seien hier Dr. Rafael Methling, Katharina Völlmecke, Dr. Maksim Rodin, Dr. Naresh Killi, Dr. Carsten Schmiegel, Dr. Tarik Rust, Dr. Dimitri Jung, Dr. Sebastian Peschtrich, Oliver Dückmann, Sascha Bierbach, Sabith Saleem und Florian Dyck genannt. Silas Schwidessen und Yin Sun danke ich besonders für praktischen Beiträge in Form ihrer Bachelorarbeiten.

Außerdem möchte ich mich bei unseren interdisziplinären Kooperationspartnern bedanken. Bei Prof. Klaus Langer, Maurice Kramer und Lisa Hönscheid von der Universität Münster, bei Prof. Dr. Klaus Huber und Leon Koch von der Universität Paderborn, bei Prof. Dr. Albena Lederer und Dr. Susanne Boye vom IPF Dresden und bei Prof. Dr. Neetu Singh vom Indian Institute of Technology in Delhi.

Ein weiterer Dank gilt jenen, die Teile meines Weges seit dem ersten Reagenzglas begleitet haben und mich ermutigt haben meinen Weg fortzusetzen. Frau Birke, Frau Koop, Frau Bala, Herr Dr. Bollmann, Dr. Schulz, Dr. Dibbert, Prof. Kirschning und viele Weitere.

Zum Schluss gebührt ein Riesendank meinen engsten Begleitern. Meinen Eltern danke ich für die immense Unterstützung und dafür, dass sie immer an mich geglaubt haben, auch wenn ich ihre Geduld manchmal auf die Probe gestellt habe. Meiner Frau Gesina danke ich dafür, dass sie mir immer den Rücken freigehalten hat und meiner Tochter Thea für die Motivation, die sie mir in den letzten Monaten dieser Arbeit gegeben hat. Aber auch dem Rest meiner Familie und all meinen Freunden möchte ich danken. Ihr seid mir immer eine große Stützte im Leben.

Eidesstattliche Erklärung

Hiermit versichere ich, Matthias van der Linde, die vorliegende Arbeit selbstständig, ohne Hilfe Dritter und nur mit den angegebenen Quellen sowie Hilfsmitteln angefertigt zu haben. Alle Stellen, die ganz oder in Teilen anderen Quellen entnommen wurden, sind als solche kenntlich gemacht worden. Diese Arbeit wurde weder in dieser noch in ähnlicher Form einer Prüfungsbehörde des In- oder Auslands vorgelegt.

_____

Ort, Datum, Matthias van der Linde

Eidesstattliche Erklärung

Anerkennung der Promotionsordnung

Hiermit erkenne ich, Matthias van der Linde, die Promotionsordnung der Fakultät für Naturwissenschaften der Universität Paderborn, welche am 12. November 2012 durch die Universität erlassen wurde, zuletzt mit der Ausgabe 10.21 vom 31. März 2021 geändert wurde, an. Bisher wurde weder an der Universität Paderborn noch an einer anderen Hochschule im In- und Ausland ein Promotionsversuch unternommen.

_____

Ort, Datum, Matthias van der Linde

6 References

(1) Tenchov, R.; Bird, R.; Curtze, A. E.; Zhou, Q. Lipid Nanoparticles–From Liposomes to mRNA Vaccine Delivery, a Landscape of Research Diversity and Advancement. *ACS nano* **2021**, *15*, 16982–17015.

(2) Siegel, R. L.; Miller, K. D.; Wagle, N. S.; Jemal, A. Cancer statistics, 2023. *CA Cancer J Clin.* **2023**, *73*, 17–48.

(3) Allen, T. M.; Cullis, P. R. Liposomal drug delivery systems: from concept to clinical applications. *Adv. Drug Delivery Rev.* **2013**, *65*, 36–48.

(4) Allen, T. M.; Cullis, P. R. Drug delivery systems: entering the mainstream. *Science* **2004**, *303*, 1818–1822.

(5) Kamaly, N.; Yameen, B.; Wu, J.; Farokhzad, O. C. Degradable Controlled-Release Polymers and Polymeric Nanoparticles: Mechanisms of Controlling Drug Release. *Chem. Rev.* **2016**, *116*, 2602–2663.

(6) Zhang, M.; Li, D.; Shan, P.; Lian, X.; Qi, Y.; Du, K.; Ma, G.; Cai, L.; Li, Z.; Li, Z. Photo and acid dual degradable polymeric nanoparticles from an o -nitrobenzyl dithiol with thiol–ene click polymerization. *Polym. Chem.* **2023**, *14*, 3146–3150.

(7) Jäger, E.; Humajová, J.; Dölen, Y.; Kučka, J.; Jäger, A.; Konefał, R.; Pankrác, J.; Pavlova, E.; Heizer, T.; Šefc, L.*; et al.* Enhanced Antitumor Efficacy through an "AND gate" Reactive Oxygen-Species-Dependent pH-Responsive Nanomedicine Approach. *Adv. Healthcare Mater.* **2021**, *10*, e2100304.

(8) Anderski, J.; Mahlert, L.; Sun, J.; Birnbaum, W.; Mulac, D.; Schreiber, S.; Herrmann, F.; Kuckling, D.; Langer, K. Light-responsive nanoparticles based on new polycarbonate polymers as innovative drug delivery systems for photosensitizers in PDT. *Int. J. Pharm.* **2019**, *557*, 182–191.

(9) Muz, B.; La Puente, P. de; Azab, F.; Azab, A. K. The role of hypoxia in cancer progression, angiogenesis, metastasis, and resistance to therapy. *Hypoxia (Auckl.)* **2015**, *3*, 83–92.

(10) Xiao, Y.; Yu, D. Tumor microenvironment as a therapeutic target in cancer. *Pharmacol. Ther.* **2021**, *221*, 107753.

(11) Yang, S. C.; Bhide, M.; Crispe, I. N.; Pierce, R. H.; Murthy, N. Polyketal copolymers: a new acid-sensitive delivery vehicle for treating acute inflammatory diseases. *Bioconjugate Chem.* **2008**, *19*, 1164–1169.

(12) *The IUPAC Compendium of Chemical Terminology,* Blackwell Scientific Publications, 2nd ed.; International Union of Pure and Applied Chemistry (IUPAC): Research Triangle Park, NC, 2019.

(13) Lechner, M. D.; Gehrke, K.; Nordmeier, E. H. *Makromolekulare Chemie: Ein Lehrbuch für Chemiker, Physiker, Materialwissenschaftler und Verfahrenstechniker*, 4. überarbeitete und erweiterte Auflage; Birkhäuser Basel: Basel, 2010.

(14) Koltzenburg, S.; Maskos, M.; Nuyken, O.; Mülhaupt, R. *Polymere: Synthese, Eigenschaften und Anwendungen*; Springer Berlin Heidelberg; Imprint: Springer Spektrum: Berlin, Heidelberg, 2014.

(15) Colebatch, A. L.; Weller, A. S. Amine-Borane Dehydropolymerization: Challenges and Opportunities. *Chem. Eur. J.* **2019**, *25*, 1379–1390.

(16) Carothers, W. H. Polymers and polyfunctionality. *Trans. Faraday Soc.* **1936**, *32*, 39.

(17) Schamboeck, V.; Iedema, P. D.; Kryven, I. Dynamic Networks that Drive the Process of Irreversible Step-Growth Polymerization. *Sci. Rep.* **2019**, *9*, 2276.

(18) Berezkin, A. V.; Kudryavtsev, Y. V. Effect of Cross-Linking on the Structure and Growth of Polymer Films Prepared by Interfacial Polymerization. *Langmuir* **2015**, *31*, 12279–12290.

(19) polyaddition. *The IUPAC Compendium of Chemical Terminology,* 2nd ed.; International Union of Pure and Applied Chemistry (IUPAC): Research Triangle Park, NC, 2019.

(20) polycondensation. *The IUPAC Compendium of Chemical Terminology,* 2nd ed.; International Union of Pure and Applied Chemistry (IUPAC): Research Triangle Park, NC, 2019.

(21) Howard, G. T. Biodegradation of polyurethane: a review. *Int. Biodeterior. Biodegrad.* **2002**, *49*, 245–252.

(22) Phua, S. K.; Castillo, E.; Anderson, J. M.; Hiltner, A. Biodegradation of a polyurethane in vitro. *J. Biomed. Mater. Res.* **1987**, *21*, 231–246.

(23) Burke, A.; Hasirci, N. Polyurethanes in biomedical applications. *Adv. Exp. Med. Biol.* **2004**, *553*, 83–101.

(24) Agrawal, C. M.; Parr, J. E.; Lin, S. T. *Synthetic bioabsorbable polymers for implants*, Online-ausg; PA : American Society for Testing and Materials: West Conshohocken, 2000.

(25) Niesiobędzka, J.; Datta, J. Challenges and recent advances in bio-based isocyanate production. *Green Chem.* **2023**, *25*, 2482–2504.

(26) Zhang, J.-Y.; Beckman, E. J.; Hu, J.; Yang, G.-G.; Agarwal, S.; Hollinger, J. O. Synthesis, biodegradability, and biocompatibility of lysine diisocyanate-glucose polymers. *Tissue Eng.* **2002**, *8*, 771–785.

(27) Zhang, J. Y.; Beckman, E. J.; Piesco, N. P.; Agarwal, S. A new peptide-based urethane polymer: synthesis, biodegradation, and potential to support cell growth in vitro. *Biomat.* **2000**, *21*, 1247–1258.

(28) Zhou, L.; Yu, L.; Ding, M.; Li, J.; Tan, H.; Wang, Z.; Fu, Q. Synthesis and Characterization of pH-Sensitive Biodegradable Polyurethane for Potential Drug Delivery Applications. *Macromol. Chem. Phys.* **2011**, *44*, 857–864.

(29) Akindoyo, J. O.; Beg, M. D. H.; Ghazali, S.; Islam, M. R.; Jeyaratnam, N.; Yuvaraj, A. R. Polyurethane types, synthesis and applications – a review. *RSC Adv.* **2016**, *6*, 114453–114482.

(30) Reegen, S. L.; Frisch, K. C. Isocyanate–catalyst and hydroxyl–catalyst complex formation. *J. Polym. Sci., Part A:Polym. Chem.* **1970**, *8*, 2883–2891.

(31) Luo, S.-G.; Tan, H.-M.; Zhang, J.-G.; Wu, Y.-J.; Pei, F.-K.; Meng, X.-H. Catalytic mechanisms of triphenyl bismuth, dibutyltin dilaurate, and their combination in polyurethane-forming reaction. *J. Appl. Polym. Sci.* **1997**, *65*, 1217–1225.

(32) Braun, D. *Polymer synthesis: Theory and practice : fundamentals, methods, experiments*, 5th ed.; Springer: Berlin, 2013.

(33) Korshak, V. V.; Vinogradova, S. V. Non-equilibrium polycondensation (review). *Polymer Science U.S.S.R.* **1971**, *13*, 415–434.

(34) Rayaprolu, B. M.; Strawser, J. J.; Anyarambhatla, G. Excipients in parenteral formulations: selection considerations and effective utilization with small molecules and biologics. *Drug Dev. Ind. Pharm.* **2018**, *44*, 1565–1571.

(35) Adepu, S.; Ramakrishna, S. Controlled Drug Delivery Systems: Current Status and Future Directions. *Molecules* **2021**, *26*.

(36) LaVan, D. A.; McGuire, T.; Langer, R. Small-scale systems for in vivo drug delivery. *Nat. Biotechnol.* **2003**, *21*, 1184–1191.

(37) Jain, A. K.; Thareja, S. In vitro and in vivo characterization of pharmaceutical nanocarriers used for drug delivery. *Artif. Cells Nanomed. Biotechnol.* **2019**, *47*, 524–539.

(38) Kamaly, N.; Xiao, Z.; Valencia, P. M.; Radovic-Moreno, A. F.; Farokhzad, O. C. Targeted polymeric therapeutic nanoparticles: design, development and clinical translation. *Chem. Soc. Rev.* **2012**, *41*, 2971–3010.

(39) Langer, R. New methods of drug delivery. *Science* **1990**, *249*, 1527–1533.

(40) Bangham, A. D.; Standish, M. M.; Watkins, J. C. Diffusion of univalent ions across the lamellae of swollen phospholipids. *J. Mol. Biol.* **1965**, *13*, 238–252.

(41) Farokhzad, O. C.; Langer, R. Impact of nanotechnology on drug delivery. *ACS nano* **2009**, *3*, 16–20.

(42) BUHLEIER, E.; WEHNER, W.; VÖGTLE, F. "Cascade"- and "Nonskid-Chain-like" Syntheses of Molecular Cavity Topologies. *Synthesis* **1978**, *1978*, 155–158.

(43) Gref, R.; Minamitake, Y.; Peracchia, M. T.; Trubetskoy, V.; Torchilin, V.; Langer, R. Biodegradable long-circulating polymeric nanospheres. *Science* **1994**, *263*, 1600–1603.

(44) Allen, T. M.; Chonn, A. Large unilamellar liposomes with low uptake into the reticuloendothelial system. *FEBS Lett.* **1987**, *223*, 42–46.

(45) Barenholz, Y. Doxil®--the first FDA-approved nano-drug: lessons learned. *J. Controll Release* **2012**, *160*, 117–134.

(46) Zhang, P.; Sun, F.; Liu, S.; Jiang, S. Anti-PEG antibodies in the clinic: Current issues and beyond PEGylation. *J. Controlled Release* **2016**, *244*, 184–193.

(47) Pelosi, C.; Tinè, M. R.; Wurm, F. R. Main-chain water-soluble polyphosphoesters: Multifunctional polymers as degradable PEG-alternatives for biomedical applications. *Eur. Polym. J.* **2020**, *141*, 110079.

(48) Matsumura, Y.; Maeda, H. A New Concept for Macromolecular Therapeutics in Cancer Chemotherapy: Mechanism of Tumoritropic Accumulation of Proteins and the Antitumor Agent Smancs. *Mol. Cancer Ther.* **1986**, *46*, 6387–6392.

(49) Maeda, H.; Bharate, G. Y.; Daruwalla, J. Polymeric drugs for efficient tumor-targeted drug delivery based on EPR-effect. *Eur. J. Pharm. Biopharm.* **2009**, *71*, 409–419.

(50) Iyer, A. K.; Khaled, G.; Fang, J.; Maeda, H. Exploiting the enhanced permeability and retention effect for tumor targeting. *Drug Discov. Today* **2006**, *11*, 812–818.

(51) Maeda, H.; Matsumura, Y. Tumoritropic and lymphotropic principles of macromolecular drugs. *Crit. Rev. Ther. Drug Carrier Syst.* **1989**, *6*, 193–210.

(52) Xie, X.; Zhang, Y.; Li, F.; Lv, T.; Li, Z.; Chen, H.; Jia, L.; Gao, Y. Challenges and Opportunities from Basic Cancer Biology for Nanomedicine for Targeted Drug Delivery. *Curr. Cancer Drug Targets* **2019**, *19*, 257–276.

(53) Folkman, J. Angiogenesis in cancer, vascular, rheumatoid and other disease. *Nat. Med.* **1995**, *1*, 27–31.

(54) Skinner, S. A.; Tutton, P. J.; O'Brien, P. E. Microvascular architecture of experimental colon tumors in the rat. *Cancer Res.* **1990**, *50*, 2411–2417.

(55) Suzuki, M.; Hori, K.; Abe, I.; Saito, S.; Sato, H. A new approach to cancer chemotherapy: selective enhancement of tumor blood flow with angiotensin II. *JNCI* **1981**, *67*, 663–669.

(56) Iwai, K.; Maeda, H.; Konno, T. Use of oily contrast medium for selective drug targeting to tumor: enhanced therapeutic effect and X-ray image. *Cancer Res.* **1984**, *44*, 2115–2121.

(57) Sinha, R.; Kim, G. J.; Nie, S.; Shin, D. M. Nanotechnology in cancer therapeutics: bioconjugated nanoparticles for drug delivery. *Mol. Cancer Ther.* **2006**, *5*, 1909–1917.

(58) Heath, T. D.; Fraley, R. T.; Papahdjopoulos, D. Antibody targeting of liposomes: cell specificity obtained by conjugation of F(ab')2 to vesicle surface. *Science* **1980**, *210*, 539–541.

(59) Leserman, L. D.; Barbet, J.; Kourilsky, F.; Weinstein, J. N. Targeting to cells of fluorescent liposomes covalently coupled with monoclonal antibody or protein A. *Nature* **1980**, *288*, 602–604.

(60) Torchilin, V. P. Immunoliposomes and PEGylated immunoliposomes: possible use for targeted delivery of imaging agents. *ImmunoMethods* **1994**, *4*, 244–258.

(61) Das, M.; Mohanty, C.; Sahoo, S. K. Ligand-based targeted therapy for cancer tissue. *Expert Opin. Drug Deliv.* **2009**, *6*, 285–304.

(62) Gierlich, P.; Mata, A. I.; Donohoe, C.; Brito, R. M. M.; Senge, M. O.; Gomes-da-Silva, L. C. Ligand-Targeted Delivery of Photosensitizers for Cancer Treatment. *Molecules* **2020**, *25*.

(63) Chen, D.; Parayath, N.; Ganesh, S.; Wang, W.; Amiji, M. The role of apolipoprotein- and vitronectin-enriched protein corona on lipid nanoparticles for in vivo targeted delivery and transfection of oligonucleotides in murine tumor models. *Nanoscale* **2019**, *11*, 18806–18824.

(64) Alyautdin, R.; Khalin, I.; Nafeeza, M. I.; Haron, M. H.; Kuznetsov, D. Nanoscale drug delivery systems and the blood-brain barrier. *Int. J. Nanomed.* **2014**, *9*, 795–811.

(65) Mitchell, M. J.; Billingsley, M. M.; Haley, R. M.; Wechsler, M. E.; Peppas, N. A.; Langer, R. Engineering precision nanoparticles for drug delivery. *Nat. Rev. Drug Discov.* **2021**, *20*, 101–124.

(66) Sun, Y.; Davis, E. Nanoplatforms for Targeted Stimuli-Responsive Drug Delivery: A Review of Platform Materials and Stimuli-Responsive Release and Targeting Mechanisms. *Nanomaterials* **2021**, *11*, 746.

(67) Yatvin, M. B.; Kreutz, W.; Horwitz, B. A.; Shinitzky, M. pH-sensitive liposomes: possible clinical implications. *Science* **1980**, *210*, 1253–1255.

(68) Wang, X.; Li, C.; Wang, Y.; Chen, H.; Zhang, X.; Luo, C.; Zhou, W.; Li, L.; Teng, L.; Yu, H.*; et al.* Smart drug delivery systems for precise cancer therapy. *Acta Pharm. Sin. B.* **2022**, *12*, 4098–4121.

(69) Rust, T.; Jung, D.; Langer, K.; Kuckling, D. Stimuli-accelerated polymeric drug delivery systems. *Polym. Int.* **2023**, *72*, 5–19.

(70) Malhotra, S.; Dumoga, S.; Mehta, S.; Rao, E. P.; Mohanty, S.; Singh, N. Engineering Cellular Membrane for Dual Mode Therapy Using NIR Responsive Photosensitizer and Reversible Topoisomerase Inhibition Activity. *ACS Appl. Bio Mater.* **2022**, *5*, 570–582.

(71) Sung, H.; Ferlay, J.; Siegel, R. L.; Laversanne, M.; Soerjomataram, I.; Jemal, A.; Bray, F. Global Cancer Statistics 2020: GLOBOCAN Estimates of Incidence and Mortality Worldwide for 36 Cancers in 185 Countries. *CA: Cancer J. Clin.* **2021**, *71*, 209–249.

(72) Chen, Y.-C.; Gad, S. F.; Chobisa, D.; Li, Y.; Yeo, Y. Local drug delivery systems for inflammatory diseases: Status quo, challenges, and opportunities. *J. Control. Release* **2021**, *330*, 438–460.

(73) Kotla, N. G.; Rana, S.; Sivaraman, G.; Sunnapu, O.; Vemula, P. K.; Pandit, A.; Rochev, Y. Bioresponsive drug delivery systems in intestinal inflammation: State-of-the-art and future perspectives. *Adv. Drug Delivery Rev.* **2019**, *146*, 248–266.

(74) Mamo, T.; Moseman, E. A.; Kolishetti, N.; Salvador-Morales, C.; Shi, J.; Kuritzkes, D. R.; Langer, R.; Andrian, U. von; Farokhzad, O. C. Emerging nanotechnology approaches for HIV/AIDS treatment and prevention. *Nanomedicine* **2010**, *5*, 269–285.

(75) Dou, Y.; Li, C.; Li, L.; Guo, J.; Zhang, J. Bioresponsive drug delivery systems for the treatment of inflammatory diseases. *J. Control. Release* **2020**, *327*, 641–666.

(76) Muhammad, S. A. Are extracellular vesicles new hope in clinical drug delivery for neurological disorders? *Neurochem. Int.* **2021**, *144*, 104955.

(77) Mittal, R.; Jayant, R. D. Recent Advancements in Identification of Novel Drug Targets and Drug Delivery for Cardiovascular and Hematological Disorders. *Cardiovasc. Hematol. Disord. - Drug Targets* **2019**, *19*, 3–4.

(78) Pala, R.; Anju, V. T.; Dyavaiah, M.; Busi, S.; Nauli, S. M. Nanoparticle-Mediated Drug Delivery for the Treatment of Cardiovascular Diseases. *Int. J. Nanomed.* **2020**, *15*, 3741–3769.

(79) Anselmo, A. C.; Mitragotri, S. Nanoparticles in the clinic. *Bioengineering & translational medicine* **2016**, *1*, 10–29.

(80) Anselmo, A. C.; Mitragotri, S. Nanoparticles in the clinic: An update. *Bioengineering & translational medicine* **2019**, *4*, e10143.

(81) Adler-Moore, J.; Proffitt, R. T. AmBisome: liposomal formulation, structure, mechanism of action and pre-clinical experience. *J. Antimicrob. Chemother.* **2002**, *49 Suppl 1*, 21–30.

(82) Phuphanich, S.; Maria, B.; Braeckman, R.; Chamberlain, M. A pharmacokinetic study of intra-CSF administered encapsulated cytarabine (DepoCyt) for the treatment of neoplastic meningitis in patients with leukemia, lymphoma, or solid tumors as part of a phase III study. *Neuro-oncol. adv.* **2007**, *81*, 201–208.

(83) Zhong, H.; Chan, G.; Hu, Y.; Hu, H.; Ouyang, D. A Comprehensive Map of FDA-Approved Pharmaceutical Products. *Pharmaceutics* **2018**, *10*.

(84) Zhang, H. Onivyde for the therapy of multiple solid tumors. *OncoTargets Ther.* **2016**, *9*, 3001–3007.

(85) Chahar, P.; Cummings, K. C. Liposomal bupivacaine: a review of a new bupivacaine formulation. *J. Pain Res.* **2012**, *5*, 257–264.

(86) Sartor, O. Eligard® 6: A New Form of Treatment for Prostate Cancer. *Eur. Urol. Suppl.* **2006**, *5*, 905–910.

(87) Miele, E.; Spinelli, G. P.; Miele, E.; Tomao, F.; Tomao, S. Albumin-bound formulation of paclitaxel (Abraxane ABI-007) in the treatment of breast cancer. *Int. J. Nanomed.* **2009**, *4*, 99–105.

(88) Daghistani, N.; Rey, J. A. Invega Trinza: The First Four-Times-a-Year, Long-Acting Injectable Antipsychotic Agent. *J. Clin. Pharm. Ther.* **2016**, *41*, 222–227.

(89) Chappuy, M.; Trojak, B.; Nubukpo, P.; Bachellier, J.; Bendimerad, P.; Brousse, G.; Rolland, B. Prolonged-release buprenorphine formulations: Perspectives for clinical practice. *Therapie* **2020**, *75*, 397–406.

(90) Parker, K. L.; Baens-Bailon, R. G.; Lee, P. A. Depot leuprolide acetate dosage for sexual precocity. *J. Clin. Endocrinol. Metab.* **1991**, *73*, 50–52.

(91) Fløgstad, A. K.; Halse, J.; Bakke, S.; Lancranjan, I.; Marbach, P.; Bruns, C.; Jervell, J. Sandostatin LAR in acromegalic patients: long-term treatment. *J. Clin. Endocrinol. Metab.* **1997**, *82*, 23–28.

(92) Vargason, A. M.; Anselmo, A. C.; Mitragotri, S. The evolution of commercial drug delivery technologies. *Nat. Biomed. Eng.* **2021**, *5*, 951–967.

(93) Kasenda, B.; König, D.; Manni, M.; Ritschard, R.; Duthaler, U.; Bartoszek, E.; Bärenwaldt, A.; Deuster, S.; Hutter, G.; Cordier, D.*; et al.* Targeting immunoliposomes to EGFR-positive glioblastoma. *ESMO open* **2022**, *7*, 100365.

(94) Siefker-Radtke, A.; Zhang, X.-Q.; Guo, C. C.; Shen, Y.; Pirollo, K. F.; Sabir, S.; Leung, C.; Leong-Wu, C.; Ling, C.-M.; Chang, E. H.*; et al.* A Phase l Study of a Tumor-targeted Systemic Nanodelivery System, SGT-94, in Genitourinary Cancers. *Mol. Ther.* **2016**, *24*, 1484–1491.

(95) Mayo Clinic. *Nab-paclitaxel/Rituximab-coated Nanoparticle AR160 in Treating Patients With Relapsed or Refractory B-Cell Non-Hodgkin Lymphoma, LS1681 Trial*, 2023 (NCT03003546). https://clinicaltrials.gov/study/NCT03003546?cond=NCT03003546&rank=1.

(96) Molinar, C.; Tannous, M.; Meloni, D.; Cavalli, R.; Scomparin, A. Current Status and Trends in Nucleic Acids for Cancer Therapy: A Focus on Polysaccharide-Based Nanomedicines. *Macromol. Biosci.* **2023**, *23*, e2300102.

(97) Shan, X.; Gong, X.; Li, J.; Wen, J.; Li, Y.; Zhang, Z. Current approaches of nanomedicines in the market and various stage of clinical translation. *Acta Pharm. Sin. B.* **2022**, *12*, 3028–3048.

(98) European Federation of Pharmaceutical Industries and Associations. The Pharmaceutical Industry in Figures: Key Data 2018. *efpia* [Online]. https://www.efpia.eu/publications/downloads/efpia/the-pharmaceutical-industry-in-figures-2023/ (accessed October 15, 2023).

(99) Monitor Deloitte. Early Value Assessment: Optimizing the upside value potential of your asset. https://www2.deloitte.com/content/dam/Deloitte/be/Documents/life-sciences-health-care/Deloitte%20Belgium_Early%20Value%20Assessment.pdf (accessed October 15, 2023).

(100) Halwani, A. A. Development of Pharmaceutical Nanomedicines: From the Bench to the Market. *Pharmaceutics* **2022**, *14*.

(101) Mura, S.; Nicolas, J.; Couvreur, P. Stimuli-responsive nanocarriers for drug delivery. *Nat. Mater.* **2013**, *12*, 991–1003.

(102) Liu, D.; Yang, F.; Xiong, F.; Gu, N. The Smart Drug Delivery System and Its Clinical Potential. *Theranostics* **2016**, *6*, 1306–1323.

(103) Bae, Y. H.; Park, K. Advanced drug delivery 2020 and beyond: Perspectives on the future. *Adv. Drug Delivery Rev.* **2020**, *158*, 4–16.

(104) Bush, V. *Science, the Endless Frontier*; Princeton University Press, 2020.

(105) Patra, J. K.; Das, G.; Fraceto, L. F.; Campos, E. V. R.; Rodriguez-Torres, M. d. P.; Acosta-Torres, L. S.; Diaz-Torres, L. A.; Grillo, R.; Swamy, M. K.; Sharma, S.*; et al.* Nano based drug delivery systems: recent developments and future prospects. *J. Nanobiotechnol.* **2018**, *16*, 71.

(106) El-Say, K. M.; El-Sawy, H. S. Polymeric nanoparticles: Promising platform for drug delivery. *Int. J. Pharm.* **2017**, *528*, 675–691.

(107) Uhrich, K. E.; Cannizzaro, S. M.; Langer, R. S.; Shakesheff, K. M. Polymeric systems for controlled drug release. *Chem. Rev.* **1999**, *99*, 3181–3198.

(108) Soppimath, K. S.; Aminabhavi, T. M.; Kulkarni, A. R.; Rudzinski, W. E. Biodegradable polymeric nanoparticles as drug delivery devices. *J. Controlled Release* **2001**, *70*, 1–20.

(109) Sun, J.; Birnbaum, W.; Anderski, J.; Picker, M.-T.; Mulac, D.; Langer, K.; Kuckling, D. Use of Light-Degradable Aliphatic Polycarbonate Nanoparticles As Drug Carrier for Photosensitizer. *Biomacromolecules* **2018**, *19*, 4677–4690.

(110) Fomina, N.; McFearin, C.; Sermsakdi, M.; Edigin, O.; Almutairi, A. UV and near-IR triggered release from polymeric nanoparticles. *J. Am. Chem. Soc.* **2010**, *132*, 9540–9542.

(111) Weinstain, R.; Slanina, T.; Kand, D.; Klán, P. Visible-to-NIR-Light Activated Release: From Small Molecules to Nanomaterials. *Chem. Rev.* **2020**, *120*, 13135–13272.

(112) Awad, N. S.; Paul, V.; AlSawaftah, N. M.; Haar, G. ter; Allen, T. M.; Pitt, W. G.; Husseini, G. A. Ultrasound-Responsive Nanocarriers in Cancer Treatment: A Review. *ACS Pharmacol. Transl. Sci.* **2021**, *4*, 589–612.

(113) Wang, Y.; Xu, H.; Wang, J.; Ge, L.; Zhu, J. Development of a thermally responsive nanogel based on chitosan-poly(N-isopropylacrylamide-co-acrylamide) for paclitaxel delivery. *J. Pharm. Sci.* **2014**, *103*, 2012–2021.

(114) Ta, T.; Porter, T. M. Thermosensitive liposomes for localized delivery and triggered release of chemotherapy. *J. Controlled Release* **2013**, *169*, 112–125.

(115) McGarry, T.; Biniecka, M.; Veale, D. J.; Fearon, U. Hypoxia, oxidative stress and inflammation. *Free Radic. Biol. Med.* **2018**, *125*, 15–24.

(116) Fang, F. C. Antimicrobial reactive oxygen and nitrogen species: concepts and controversies. *Nat. Rev. Microbiol.* **2004**, *2*, 820–832.

(117) Bhattacharyya, S. The Triad, Hypoxia–ROS–Inflammation. In *Handbook of oxidative stress in cancer--Volume 1. Mechanistic aspects*; Chakraborti, S., Ray, B. K., Roychoudhury, S., Eds.; Springer reference; Springer: Singapore, [Berlin], 2021; pp 991–1004.

(118) Hu, Q.; Katti, P. S.; Gu, Z. Enzyme-responsive nanomaterials for controlled drug delivery. *Nanoscale* **2014**, *6*, 12273–12286.

(119) Andresen, T. L.; Thompson, D. H.; Kaasgaard, T. Enzyme-triggered nanomedicine: drug release strategies in cancer therapy. *Mol. Membr. Biol.* **2010**, *27*, 353–363.

(120) McCarley, R. L. Redox-responsive delivery systems. *Annu. Rev. Anal. Chem. (Palo Alto, Calif.)* **2012**, *5*, 391–411.

(121) Liu, J.; Huang, Y.; Kumar, A.; Tan, A.; Jin, S.; Mozhi, A.; Liang, X.-J. pH-sensitive nano-systems for drug delivery in cancer therapy. *Biotechnology advances* **2014**, *32*, 693–710.

(122) Zhu, Y.-J.; Chen, F. pH-responsive drug-delivery systems. *Chemistry, an Asian journal* **2015**, *10*, 284–305.

(123) Wuts, P. G. M. *Greene's protective groups in organic synthesis*, 5th ed.; John Wiley & Sons: Hoboken, New Jersey, op. 2014.

(124) Wan, P.; Yates, K. Photoredox chemistry of nitrobenzyl alcohols in aqueous solution. Acid and base catalysis of reaction. *Can. J. Chem.* **1986**, *64*, 2076–2086.

(125) Il'ichev, Y. V.; Schwörer, M. A.; Wirz, J. Photochemical reaction mechanisms of 2-nitrobenzyl compounds: methyl ethers and caged ATP. *J. Am. Chem. Soc.* **2004**, *126*, 4581–4595.

(126) Heller, J.; Barr, J. Poly(ortho esters)--from concept to reality. *Biomacromolecules* **2004**, *5*, 1625–1632.

(127) Heller, J. Ocular delivery using poly(ortho esters). *Adv. Drug Delivery Rev.* **2005**, *57*, 2053–2062.

(128) Xiao, Y.; Tan, X.; Li, Z.; Zhang, K. Self-immolative polymers in biomedicine. *J. Mater. Chem. B* **2020**, *8*, 6697–6709.

(129) Sirianni, Q. E.; Gillies, E. R. The architectural evolution of self-immolative polymers. *Polymer* **2020**, *202*, 122638.

(130) Sagi, A.; Weinstain, R.; Karton, N.; Shabat, D. Self-immolative polymers. *J. Am. Chem. Soc.* **2008**, *130*, 5434–5435.

(131) Joo, W.; Wang, W.; Mesch, R.; Matsuzawa, K.; Di Liu; Willson, C. G. Synthesis of Unzipping Polyester and a Study of its Photochemistry. *J. Am. Chem. Soc.* **2019**, *141*, 14736–14741.

(132) Pal, S.; Sommerfeldt, A.; Davidsen, M. B.; Hinge, M.; Pedersen, S. U.; Daasbjerg, K. Synthesis and Closed-Loop Recycling of Self-Immolative Poly(dithiothreitol). *Macromolecules* **2020**, *53*, 4685–4691.

(133) Fan, B.; Trant, J. F.; Wong, A. D.; Gillies, E. R. Polyglyoxylates: a versatile class of triggerable self-immolative polymers from readily accessible monomers. *J. Am. Chem. Soc.* **2014**, *136*, 10116–10123.

(134) Baker, M. S.; Kim, H.; Olah, M. G.; Lewis, G. G.; Phillips, S. T. Depolymerizable poly(benzyl ether)-based materials for selective room temperature recycling. *Green Chem.* **2015**, *17*, 4541–4545.

(135) Sirianni, Q. E. A.; Rabiee Kenaree, A.; Gillies, E. R. Polyglyoxylamides: Tuning Structure and Properties of Self-Immolative Polymers. *Macromolecules* **2019**, *52*, 262–270.

(136) Miller, K. A.; Morado, E. G.; Samanta, S. R.; Walker, B. A.; Nelson, A. Z.; Sen, S.; Tran, D. T.; Whitaker, D. J.; Ewoldt, R. H.; Braun, P. V.*; et al.* Acid-Triggered, Acid-Generating, and Self-Amplifying Degradable Polymers. *J. Am. Chem. Soc.* **2019**, *141*, 2838–2842.

(137) Sun, J.; Rust, T.; Kuckling, D. Light-Responsive Serinol-Based Polyurethane Nanocarrier for Controlled Drug Release. *Macromol. Rapid Commun.* **2019**, *40*, e1900348.

(138) Müller, A.-K.; Jung, D.; Sun, J.; Kuckling, D. Synthesis and characterization of light-degradable bromocoumarin functionalized polycarbonates. *Polym. Chem.* **2020**, *11*, 721–733.

(139) Rust, T.; Jung, D.; Hoppe, A.; Schoppa, T.; Langer, K.; Kuckling, D. Backbone-Degradable (Co-)Polymers for Light-Triggered Drug Delivery. *ACS Appl. Polym. Mater.* **2021**, *3*, 3831–3842.

(140) Jung, D.; Rust, T.; Völlmecke, K.; Schoppa, T.; Langer, K.; Kuckling, D. Backbone vs. side-chain: two light-degradable polyurethanes based on 6-nitropiperonal. *Polym. Chem.* **2021**, *12*, 4565–4575.

(141) Koltai, T. Cancer: fundamentals behind pH targeting and the double-edged approach. *OncoTargets Ther.* **2016**, *9*, 6343–6360.

(142) WARBURG, O. On the origin of cancer cells. *Science* **1956**, *123*, 309–314.

(143) Altenberg, B.; Greulich, K. O. Genes of glycolysis are ubiquitously overexpressed in 24 cancer classes. *Genomics* **2004**, *84*, 1014–1020.

(144) Helmlinger, G.; Yuan, F.; Dellian, M.; Jain, R. K. Interstitial pH and pO2 gradients in solid tumors in vivo: high-resolution measurements reveal a lack of correlation. *Nat. Med.* **1997**, *3*, 177–182.

(145) Gillies, R. J.; Liu, Z.; Bhujwalla, Z. 31P-MRS measurements of extracellular pH of tumors using 3-aminopropylphosphonate. *Am. J. Physiol. Cell Physiol.* **1994**, *267*, C195-203.

(146) Stubbs, M.; McSheehy, P. M.; Griffiths, J. R.; Bashford, C. L. Causes and consequences of tumour acidity and implications for treatment. *Mol. Med.* **2000**, *6*, 15–19.

(147) Maxfield, F. R.; Yamashiro, D. J. Endosome acidification and the pathways of receptor-mediated endocytosis. *Adv. Exp. Med. Biol.* **1987**, *225*, 189–198.

(148) Hu, J.; He, J.; Zhang, M.; Ni, P. Precise modular synthesis and a structure–property study of acid-cleavable star-block copolymers for pH-triggered drug delivery. *Polym. Chem.* **2015**, *6*, 1553–1566.

(149) Paramonov, S. E.; Bachelder, E. M.; Beaudette, T. T.; Standley, S. M.; Lee, C. C.; Dashe, J.; Fréchet, J. M. J. Fully acid-degradable biocompatible polyacetal microparticles for drug delivery. *Bioconjugate Chem.* **2008**, *19*, 911–919.

(150) Liu, B.; Thayumanavan, S. Substituent Effects on the pH Sensitivity of Acetals and Ketals and Their Correlation with Encapsulation Stability in Polymeric Nanogels. *J. Am. Chem. Soc.* **2017**, *139*, 2306–2317.

(151) Burkersroda, F. von; Schedl, L.; Göpferich, A. Why degradable polymers undergo surface erosion or bulk erosion. *Biomaterials* **2002**, *23*, 4221–4231.

(152) Park, H.; Park, K.; Shalaby, W. S. W. *Biodegradable Hydrogels for Drug Delivery*; CRC Press LLC: Boca Raton, 1993.

(153) Langer, R. S.; Peppas, N. A., Eds. *Biopolymers I*; Advances in Polymer Science 107; Springer: Berlin, Heidelberg, 1993.

(154) Heller, J. Poly (ortho esters). In *Biopolymers I*; Langer, R. S., Peppas, N. A., Eds.; Advances in Polymer Science 107; Springer: Berlin, Heidelberg, 1993; pp 41–92.

(155) Sintzel, M. B.; Heller, J.; Ng, S. Y.; Taylor, M. S.; Tabatabay, C.; Gurny, R. Synthesis and characterization of self-catalyzed poly(ortho ester). *Biomaterials* **1998**, *19*, 791–800.

(156) Ng, S. Y.; Vandamme, T.; Taylor, M. S.; Heller, J. Synthesis and Erosion Studies of Self-Catalyzed Poly(ortho ester)s. *Macromolecules* **1997**, *30*, 770–772.

(157) Schwach-Abdellaoui, K.; Heller, J.; Gurny, R. Hydrolysis and Erosion Studies of Autocatalyzed Poly(ortho esters) Containing Lactoyl–Lactyl Acid Dimers. *Macromolecules* **1999**, *32*, 301–307.

(158) Dailey, L. A.; Jekel, N.; Fink, L.; Gessler, T.; Schmehl, T.; Wittmar, M.; Kissel, T.; Seeger, W. Investigation of the proinflammatory potential of biodegradable nanoparticle drug delivery systems in the lung. *Toxicol. Appl. Pharmacol.* **2006**, *215*, 100–108.

(159) Heffernan, M. J.; Murthy, N. Polyketal nanoparticles: a new pH-sensitive biodegradable drug delivery vehicle. *Bioconjugate Chem.* **2005**, *16*, 1340–1342.

(160) Shenoi, R. A.; Narayanannair, J. K.; Hamilton, J. L.; Lai, B. F. L.; Horte, S.; Kainthan, R. K.; Varghese, J. P.; Rajeev, K. G.; Manoharan, M.; Kizhakkedathu, J. N. Branched multifunctional polyether polyketals: variation of ketal group structure enables unprecedented control over polymer degradation in solution and within cells. *J. Am. Chem. Soc.* **2012**, *134*, 14945–14957.

(161) ECHA. Summary of Classification and Labelling: Cyclohex-1,4-ylenedimethanol: CAS 105-08-8. https://echa.europa.eu/information-on-chemicals/cl-inventory-database/-/discli/details/13721 (accessed November 7, 2023).

(162) ECHA. Summary of Classification and Labelling: p-phenylenedimethanol: CAS Number 589-29-7. https://echa.europa.eu/information-on-chemicals/cl-inventory-database/-/discli/details/93842 (accessed November 7, 2023).

(163) Lee, S.; Yang, S. C.; Heffernan, M. J.; Taylor, W. R.; Murthy, N. Polyketal microparticles: a new delivery vehicle for superoxide dismutase. *Bioconjugate Chem.* **2007**, *18*, 4–7.

(164) Sy, J. C.; Seshadri, G.; Yang, S. C.; Brown, M.; Oh, T.; Dikalov, S.; Murthy, N.; Davis, M. E. Sustained release of a p38 inhibitor from non-inflammatory microspheres inhibits cardiac dysfunction. *Nat. Mat.* **2008**, *7*, 863–868.

(165) Seshadri, G.; Sy, J. C.; Brown, M.; Dikalov, S.; Yang, S. C.; Murthy, N.; Davis, M. E. The delivery of superoxide dismutase encapsulated in polyketal microparticles to rat myocardium and protection from myocardial ischemia-reperfusion injury. *Biomaterials* **2010**, *31*, 1372–1379.

(166) Rajagopal, P.; Jayandharan, G. R.; Krishnan, U. M. Evaluation of the Anticancer Activity of pH-Sensitive Polyketal Nanoparticles for Acute Myeloid Leukemia. *Mol. Pharmaceutics* **2021**, *18*, 2015–2031.

(167) Zhao, M.; Yao, J.; Meng, X.; Cui, Y.; Zhu, T.; Sun, F.; Li, Y.; Teng, L. Polyketal Nanoparticles Co-Loaded With miR-124 and Ketoprofen for Treatment of Rheumatoid Arthritis. *J. Pharm. Sci.* **2021**, *110*, 2233–2240.

(168) Yu, C.; Li, X.; Hou, Y.; Meng, X.; Wang, D.; Liu, J.; Sun, F.; Li, Y. Hyaluronic Acid Coated Acid-Sensitive Nanoparticles for Targeted Therapy of Adjuvant-Induced Arthritis in Rats. *Molecules* **2019**, *24*.

(169) Zhao, J.; Zhao, M.; Yu, C.; Zhang, X.; Liu, J.; Cheng, X.; Lee, R. J.; Sun, F.; Teng, L.; Li, Y. Multifunctional folate receptor-targeting and pH-responsive nanocarriers loaded with methotrexate for treatment of rheumatoid arthritis. *Int. J. Nanomed.* **2017**, *12*, 6735–6746.

(170) Liu, J.; Li, S.; Li, G.; Li, X.; Yu, C.; Fu, Z.; Li, X.; Teng, L.; Li, Y.; Sun, F. Highly bioactive, bevacizumab-loaded, sustained-release PLGA/PCADK microspheres for intravitreal therapy in ocular diseases. *Int. J. Pharm.* **2019**, *563*, 228–236.

(171) Fiore, V. F.; Lofton, M. C.; Roser-Page, S.; Yang, S. C.; Roman, J.; Murthy, N.; Barker, T. H. Polyketal microparticles for therapeutic delivery to the lung. *Biomaterials* **2010**, *31*, 810–817.

(172) Tsai, T.; Kao, C.-Y.; Chou, C.-L.; Liu, L.-C.; Chou, T.-C. Protective effect of magnolol-loaded polyketal microparticles on lipopolysaccharide-induced acute lung injury in rats. *J. Microencapsulation* **2016**, *33*, 401–411.

(173) Zhao, J.; Zhang, X.; Sun, X.; Zhao, M.; Yu, C.; Lee, R. J.; Sun, F.; Zhou, Y.; Li, Y.; Teng, L. Dual-functional lipid polymeric hybrid pH-responsive nanoparticles decorated with cell penetrating peptide and folate for therapy against rheumatoid arthritis. *Eur. J. Pharm. Biopharm.* **2018**, *130*, 39–47.

(174) Li, X.; Yu, C.; Meng, X.; Hou, Y.; Cui, Y.; Zhu, T.; Li, Y.; Teng, L.; Sun, F.; Li, Y. Study of double-targeting nanoparticles loaded with MCL-1 siRNA and dexamethasone for adjuvant-induced arthritis therapy. *Eur. J. Pharm. Biopharm.* **2020**, *154*, 136–143.

(175) Looi, Y. H.; Grieve, D. J.; Siva, A.; Walker, S. J.; Anilkumar, N.; Cave, A. C.; Marber, M.; Monaghan, M. J.; Shah, A. M. Involvement of Nox2 NADPH oxidase in adverse cardiac remodeling after myocardial infarction. *Hypertension (Dallas, Tex. : 1979)* **2008**, *51*, 319–325.

(176) Somasuntharam, I.; Boopathy, A. V.; Khan, R. S.; Martinez, M. D.; Brown, M. E.; Murthy, N.; Davis, M. E. Delivery of Nox2-NADPH oxidase siRNA with polyketal nanoparticles for improving cardiac function following myocardial infarction. *Biomaterials* **2013**, *34*, 7790–7798.

(177) Yang, J.; Brown, M. E.; Zhang, H.; Martinez, M.; Zhao, Z.; Bhutani, S.; Yin, S.; Trac, D.; Xi, J. J.; Davis, M. E. High-throughput screening identifies microRNAs that target Nox2 and improve function after acute myocardial infarction. *Am. J. Physiol.* **2017**, *312*, H1002-H1012.

(178) Lee, I.; Park, M.; Kim, Y.; Hwang, O.; Khang, G.; Lee, D. Ketal containing amphiphilic block copolymer micelles as pH-sensitive drug carriers. *Int. J. Pharm.* **2013**, *448*, 259–266.

(179) Sun, X.; Yu, K.; Zhou, Y.; Dong, S.; Hu, W.; Sun, Y.; Li, Y.; Xie, J.; Lee, R. J.; Sun, F.*; et al.* Self-Assembled pH-Sensitive Polymeric Nanoparticles for the Inflammation-Targeted Delivery of Cu/Zn-Superoxide Dismutase. *ACS applied materials & interfaces* **2021**, *13*, 18152–18164.

(180) Mitra, K.; Hira, S. K.; Singh, S.; Vishwakarma, N. K.; Vishwakarma, S.; Gupta, U.; Manna, P. P.; Ray, B. In Vitro Anticancer Drug Delivery Using Amphiphilic Poly(N -vinylpyrrolidone)- b -Polyketal- b -Poly(N -vinylpyrrolidone) Block Copolymer as Micellar Nanocarrier. *ChemistrySelect* **2018**, *3*, 8833–8843.

(181) Hira, S. K.; Mitra, K.; Srivastava, P.; Singh, S.; Vishwakarma, S.; Singh, R.; Ray, B.; Manna, P. P. Doxorubicin loaded pH responsive biodegradable ABA-type Amphiphilic PEG-b-aliphatic Polyketal-b-PEG block copolymer for therapy against aggressive murine lymphoma. *Nanomedicine : nanotechnology, biology, and medicine* **2020**, *24*, 102128.

(182) Guo, S.; Nakagawa, Y.; Barhoumi, A.; Wang, W.; Zhan, C.; Tong, R.; Santamaria, C.; Kohane, D. S. Extended Release of Native Drug Conjugated in Polyketal Microparticles. *J. Am. Chem. Soc.* **2016**, *138*, 6127–6130.

(183) Bachelder, E. M.; Beaudette, T. T.; Broaders, K. E.; Paramonov, S. E.; Dashe, J.; Fréchet, J. M. J. Acid-degradable polyurethane particles for protein-based vaccines: biological evaluation and in vitro analysis of particle degradation products. *Mol. Pharmaceutics* **2008**, *5*, 876–884.

(184) Lim, H.; Noh, J.; Kim, Y.; Kim, H.; Kim, J.; Khang, G.; Lee, D. Acid-degradable cationic poly(ketal amidoamine) for enhanced RNA interference in vitro and in vivo. *Biomacromolecules* **2013**, *14*, 240–247.

(185) Pohlit, H.; Leibig, D.; Frey, H. Poly(Ethylene Glycol) Dimethacrylates with Cleavable Ketal Sites: Precursors for Cleavable PEG-Hydrogels. *Macromol. Biosci.* **2017**, *17*.

(186) Zhong, H.; Mu, J.; Du, Y.; Xu, Z.; Xu, Y.; Yu, N.; Zhang, S.; Guo, S. Acid-Triggered Release of Native Gemcitabine Conjugated in Polyketal Nanoparticles for Enhanced Anticancer Therapy. *Biomacromolecules* **2020**, *21*, 803–814.

(187) Maity, S.; Choudhary, P.; Manjunath, M.; Kulkarni, A.; Murthy, N. A biodegradable adamantane polymer with ketal linkages in its backbone for gene therapy. *Chem. Commun.* **2015**, *51*, 15956–15959.

(188) Rajagopal, P.; Jayandharan, G. R.; Maheswari Krishnan, U. Polyketal-based nanocarriers: A new class of stimuli-responsive delivery systems for therapeutic applications. *Eur. Polym. J.* **2022**, *173*, 111290.

(189) Langer, R. S.; Peppas, N. A. Present and future applications of biomaterials in controlled drug delivery systems. *Biomaterials* **1981**, *2*, 201–214.

(190) Ulery, B. D.; Nair, L. S.; Laurencin, C. T. Biomedical Applications of Biodegradable Polymers. *J. Polym. Sci., Part B:Polym. Phys.* **2011**, *49*, 832–864.

(191) Arndt, K.-F.; Müller, G. *Polymercharakterisierung*; Hanser: München, 1996.

(192) Liu, G.; McEnnis, K. Glass Transition Temperature of PLGA Particles and the Influence on Drug Delivery Applications. *Polymers* **2022**, *14*.

(193) Qian, J.; Berkland, C. Drug Release Kinetics from Nondegradable Hydrophobic Polymers Can Be Modulated and Predicted by the Glass Transition Temperature. *Adv. Healthcare Mater.* **2021**, *10*, e2100015.

(194) Liechty, W. B.; Kryscio, D. R.; Slaughter, B. V.; Peppas, N. A. Polymers for drug delivery systems. *Annu. Rev. Chem. Biomol. Eng.* **2010**, *1*, 149–173.

(195) Zhang, J.; Chen, X. G.; Sun, G. Z.; Huang, L.; Cheng, X. J. Effect of molecular weight on the oleoyl-chitosan nanoparticles as carriers for doxorubicin. *Colloids Surf. B Biointerfaces* **2010**, *77*, 125–130.

(196) Yang, D.; Liu, X.; Jiang, X.; Liu, Y.; Ying, W.; Wang, H.; Bai, H.; Taylor, W. D.; Wang, Y.; Clamme, J.-P.*; et al.* Effect of molecular weight of PGG-paclitaxel conjugates on in vitro and in vivo efficacy. *J. Controlled Release* **2012**, *161*, 124–131.

(197) Asano, M.; Yoshida, M.; Omichi, H.; Mashimo, T.; Okabe, K.; Yuasa, H.; Yamanaka, H.; Morimoto, S.; Sakakibara, H. Biodegradable poly(DL-lactic acid) formulations in a calcitonin delivery system. *Biomaterials* **1993**, *14*, 797–799.

(198) Ramkissoon-Ganorkar, C.; Liu, F.; Baudys, M.; Kim, S. W. Effect of molecular weight and polydispersity on kinetics of dissolution and release from ph/temperature-sensitive polymers. *J. Biomater. Sci., Polym. Ed.* **1999**, *10*, 1149–1161.

(199) Makadia, H. K.; Siegel, S. J. Poly Lactic-co-Glycolic Acid (PLGA) as Biodegradable Controlled Drug Delivery Carrier. *Polymers* **2011**, *3*, 1377–1397.

(200) Swider, E.; Koshkina, O.; Tel, J.; Cruz, L. J.; Vries, I. J. M. de; Srinivas, M. Customizing poly(lactic-co-glycolic acid) particles for biomedical applications. *Acta biomater.* **2018**, *73*, 38–51.

(201) Huang, Y.; Dong, R.; Zhu, X.; Yan, D. Photo-responsive polymeric micelles. *Soft matter* **2014**, *10*, 6121–6138.

(202) Gohy, J.-F.; Zhao, Y. Photo-responsive block copolymer micelles: design and behavior. *Chem. Soc. Rev.* **2013**, *42*, 7117–7129.

(203) Bertrand, O.; Gohy, J.-F. Photo-responsive polymers: synthesis and applications. *Polym. Chem.* **2017**, *8*, 52–73.

(204) Barltrop, J. A.; Schofield, P. Photosensitive Protecting Groups. *Tetrahedron Lett.* **1962**, *3*, 697–699.

(205) Klán, P.; Šolomek, T.; Bochet, C. G.; Blanc, A.; Givens, R.; Rubina, M.; Popik, V.; Kostikov, A.; Wirz, J. Photoremovable protecting groups in chemistry and biology: reaction mechanisms and efficacy. *Chem. Rev.* **2013**, *113*, 119–191.

(206) Yu, H.; Li, J.; Wu, D.; Qiu, Z.; Zhang, Y. Chemistry and biological applications of photo-labile organic molecules. *Chem. Soc. Rev.* **2010**, *39*, 464–473.

(207) Zhao, H.; Sterner, E. S.; Coughlin, E. B.; Theato, P. o -Nitrobenzyl Alcohol Derivatives: Opportunities in Polymer and Materials Science. *Macromolecules* **2012**, *45*, 1723–1736.

(208) Beauté, L.; McClenaghan, N.; Lecommandoux, S. Photo-triggered polymer nanomedicines: From molecular mechanisms to therapeutic applications. *Adv. Drug Delivery Rev.* **2019**, *138*, 148–166.

(209) Kaplan, J. H.; Forbush, B.; Hoffman, J. F. Rapid photolytic release of adenosine 5'-triphosphate from a protected analogue: utilization by the Na:K pump of human red blood cell ghosts. *Biochemistry* **1978**, *17*, 1929–1935.

(210) Zhang, Z.; Hatta, H.; Ito, T.; Nishimoto, S. Synthesis and photochemical properties of photoactivated antitumor prodrugs releasing 5-fluorouracil. *Org. Biomol. Chem.* **2005**, *3*, 592–596.

(211) Jiang, J.; Tong, X.; Morris, D.; Zhao, Y. Toward Photocontrolled Release Using Light-Dissociable Block Copolymer Micelles. *Macromolecules* **2006**, *39*, 4633–4640.

(212) Jiang, X.; Lavender, C. A.; Woodcock, J. W.; Zhao, B. Multiple Micellization and Dissociation Transitions of Thermo- and Light-Sensitive Poly(ethylene oxide)- b - poly(ethoxytri(ethylene glycol) acrylate- co - o -nitrobenzyl acrylate) in Water. *Macromolecules* **2008**, *41*, 2632–2643.

(213) Gracia Lux, C. de; McFearin, C. L.; Joshi-Barr, S.; Sankaranarayanan, J.; Fomina, N.; Almutairi, A. A Single UV or Near IR Triggering Event Leads to Polymer Degradation into Small Molecules. *ACS Macro Lett.* **2012**, *1*, 922–926.

(214) Klinger, D. *Light-Sensitive Polymeric Nanoparticles Based on Photo-Cleavable Chromophores*; Springer Theses, Recognizing Outstanding Ph.D. Research; Springer International Publishing: Cham, s.l., 2013.

(215) Liu, G.; Wang, X.; Hu, J.; Zhang, G.; Liu, S. Self-immolative polymersomes for high-efficiency triggered release and programmed enzymatic reactions. *J. Am. Chem. Soc.* **2014**, *136*, 7492–7497.

(216) Ciamician, G.; Silber, P. Chemische Lichtwirkungen. *Ber. Dtsch. Chem. Ges.* **1901**, *34*, 2040–2046.

(217) Schmierer, T.; Laimgruber, S.; Haiser, K.; Kiewisch, K.; Neugebauer, J.; Gilch, P. Femtosecond spectroscopy on the photochemistry of ortho-nitrotoluene. *Phys. Chem. Chem. Phys.* **2010**, *12*, 15653–15664.

(218) Bamford, C. H.; Norrish, R. G. W. 359. Primary photochemical reactions. Part VII. Photochemical decomposition of isovaleraldehyde and di-n-propyl ketone. *J. Chem. Soc.* **1935**, 1504.

(219) Wang, P. Photolabile Protecting Groups: Structure and Reactivity. *Asian J. Org. Chem.* **2013**, *2*, 452–464.

(220) Hussein, M. R. Ultraviolet radiation and skin cancer: molecular mechanisms. *J. Cutan. Pathol.* **2005**, *32*, 191–205.

(221) Meinhardt, M.; Krebs, R.; Anders, A.; Heinrich, U.; Tronnier, H. Wavelength-dependent penetration depths of ultraviolet radiation in human skin. *J. Biomed. Opt.* **2008**, *13*, 44030.

(222) Menzel, J. P.; Noble, B. B.; Lauer, A.; Coote, M. L.; Blinco, J. P.; Barner-Kowollik, C. Wavelength Dependence of Light-Induced Cycloadditions. *J. Am. Chem. Soc.* **2017**, *139*, 15812–15820.

(223) Irshadeen, I. M.; Walden, S. L.; Wegener, M.; Truong, V. X.; Frisch, H.; Blinco, J. P.; Barner-Kowollik, C. Action Plots in Action: In-Depth Insights into Photochemical Reactivity. *J. Am. Chem. Soc.* **2021**, *143*, 21113–21126.

(224) Bachmann, J.; Petit, C.; Michalek, L.; Catel, Y.; Blasco, E.; Blinco, J. P.; Unterreiner, A.-N.; Barner-Kowollik, C. Chain-Length-Dependent Photolysis of ortho-Nitrobenzyl-Centered Polymers. *ACS Macro Lett.* **2021**, *10*, 447–452.

(225) Mahmoodi, M. M.; Abate-Pella, D.; Pundsack, T. J.; Palsuledesai, C. C.; Goff, P. C.; Blank, D. A.; Distefano, M. D. Nitrodibenzofuran: A One- and Two-Photon Sensitive Protecting Group That Is Superior to Brominated Hydroxycoumarin for Thiol Caging in Peptides. *J. Am. Chem. Soc.* **2016**, *138*, 5848–5859.

(226) Kohman, R. E.; Cha, S. S.; Man, H.-Y.; Han, X. Light-Triggered Release of Bioactive Molecules from DNA Nanostructures. *Nano Lett.* **2016**, *16*, 2781–2785.

(227) Mosiewicz, K. A.; Kolb, L.; van der Vlies, A. J.; Martino, M. M.; Lienemann, P. S.; Hubbell, J. A.; Ehrbar, M.; Lutolf, M. P. In situ cell manipulation through enzymatic hydrogel photopatterning. *Nat. Mater.* **2013**, *12*, 1072–1078.

(228) Hansen, M. J.; Velema, W. A.; Lerch, M. M.; Szymanski, W.; Feringa, B. L. Wavelength-selective cleavage of photoprotecting groups: strategies and applications in dynamic systems. *Chem. Soc. Rev.* **2015**, *44*, 3358–3377.

(229) Sun, J.; Anderski, J.; Picker, M.-T.; Langer, K.; Kuckling, D. Preparation of Light-Responsive Aliphatic Polycarbonate via Versatile Polycondensation for Controlled Degradation. *Macromol. Chem. Phys.* **2019**, *220*, 1800539.

(230) Hu, X.; Tian, J.; Liu, T.; Zhang, G.; Liu, S. Photo-Triggered Release of Caged Camptothecin Prodrugs from Dually Responsive Shell Cross-Linked Micelles. *Macromolecules* **2013**, *46*, 6243–6256.

(231) Wang, C.; Zhang, G.; Liu, G.; Hu, J.; Liu, S. Photo- and thermo-responsive multicompartment hydrogels for synergistic delivery of gemcitabine and doxorubicin. *J. Control. Release* **2017**, *259*, 149–159.

(232) Zhang, W.-J.; Hong, C.-Y.; Pan, C.-Y. Efficient Fabrication of Photosensitive Polymeric Nano-objects via an Ingenious Formulation of RAFT Dispersion Polymerization and Their Application for Drug Delivery. *Biomacromolecules* **2017**, *18*, 1210–1217.

(233) Klinger, D.; Landfester, K. Photo-sensitive PMMA microgels: light-triggered swelling and degradation. *Soft matter* **2011**, *7*, 1426–1440.

(234) Yavuz, M. S.; Cheng, Y.; Chen, J.; Cobley, C. M.; Zhang, Q.; Rycenga, M.; Xie, J.; Kim, C.; Song, K. H.; Schwartz, A. G.*; et al.* Gold nanocages covered by smart polymers for controlled release with near-infrared light. *Nat. Mater.* **2009**, *8*, 935–939.

(235) Basuki, J. S.; Qie, F.; Mulet, X.; Suryadinata, R.; Vashi, A. V.; Peng, Y. Y.; Li, L.; Hao, X.; Tan, T.; Hughes, T. C. Photo-Modulated Therapeutic Protein Release from a Hydrogel Depot Using Visible Light. *Angew. Chem.* **2017**, *129*, 986–991.

(236) Yang, Y.; Liu, F.; Liu, X.; Xing, B. NIR light controlled photorelease of siRNA and its targeted intracellular delivery based on upconversion nanoparticles. *Nanoscale* **2013**, *5*, 231–238.

(237) Jalani, G.; Naccache, R.; Rosenzweig, D. H.; Haglund, L.; Vetrone, F.; Cerruti, M. Photocleavable Hydrogel-Coated Upconverting Nanoparticles: A Multifunctional Theranostic Platform for NIR Imaging and On-Demand Macromolecular Delivery. *J. Am. Chem. Soc.* **2016**, *138*, 1078–1083.

(238) Fomina, N.; McFearin, C. L.; Sermsakdi, M.; Morachis, J. M.; Almutairi, A. Low power, biologically benign NIR light triggers polymer disassembly. *Macromolecules* **2011**, *44*, 8590–8597.

(239) Furuta, T.; Wang, S. S.; Dantzker, J. L.; Dore, T. M.; Bybee, W. J.; Callaway, E. M.; Denk, W.; Tsien, R. Y. Brominated 7-hydroxycoumarin-4-ylmethyls: photolabile protecting groups with biologically useful cross-sections for two photon photolysis. *PNAS* **1999**, *96*, 1193–1200.

(240) Schoppa, T.; Jung, D.; Rust, T.; Mulac, D.; Kuckling, D.; Langer, K. Light-responsive polymeric nanoparticles based on a novel nitropiperonal based polyester as drug delivery systems for photosensitizers in PDT. *Int. J. Pharm.* **2021**, *597*, 120326.

(241) Cheng, R.; Meng, F.; Deng, C.; Klok, H.-A.; Zhong, Z. Dual and multi-stimuli responsive polymeric nanoparticles for programmed site-specific drug delivery. *Biomaterials* **2013**, *34*, 3647–3657.

(242) Soppimath, K. S.; Tan, D. C.-W.; Yang, Y.-Y. pH-Triggered Thermally Responsive Polymer Core–Shell Nanoparticles for Drug Delivery. *Adv. Mater.* **2005**, *17*, 318–323.

(243) K C, R. B.; Thapa, B.; Xu, P. pH and redox dual responsive nanoparticle for nuclear targeted drug delivery. *Mol. Pharmaceutics* **2012**, *9*, 2719–2729.

(244) Chen, J.; Qiu, X.; Ouyang, J.; Kong, J.; Zhong, W.; Xing, M. M. Q. pH and reduction dual-sensitive copolymeric micelles for intracellular doxorubicin delivery. *Biomacromolecules* **2011**, *12*, 3601–3611.

(245) Mahmoud, E. A.; Sankaranarayanan, J.; Morachis, J. M.; Kim, G.; Almutairi, A. Inflammation Responsive Logic Gate Nanoparticles for the Delivery of Proteins. *Bioconjugate Chem.* **2011**, *22*, 1416–1421.

(246) Jazani, A. M.; Oh, J. K. Development and disassembly of single and multiple acid-cleavable block copolymer nanoassemblies for drug delivery. *Polym. Chem.* **2020**, *11*, 2934–2954.

(247) Sankaranarayanan, J.; Mahmoud, E. A.; Kim, G.; Morachis, J. M.; Almutairi, A. Multiresponse strategies to modulate burst degradation and release from nanoparticles. *ACS nano* **2010**, *4*, 5930–5936.

(248) Song, C.-C.; Su, C.-C.; Cheng, J.; Du, F.-S.; Liang, D.-H.; Li, Z.-C. Toward Tertiary Amine-Modulated Acid-Triggered Hydrolysis of Copolymers Containing Pendent Ortho Ester Groups. *Macromolecules* **2013**, *46*, 1093–1100.

(249) Olejniczak, J.; Nguyen Huu, V. A.; Lux, J.; Grossman, M.; He, S.; Almutairi, A. Light-triggered chemical amplification to accelerate degradation and release from polymeric particles. *Chem. Commun.* **2015**, *51*, 16980–16983.

(250) Lendlein, A. *Handbook of Biodegradable Polymers: Synthesis, Characterization and Applications*, 1., Auflage, neue Ausg; Wiley-VCH: Weinheim, 2013.

(251) Tarik Rust. Stimuli-Responsive Backbone-Degradable (Co-)Polymers for Drug Delivery. Dissertation, Paderborn University, Paderborn, 2021.

(252) Vinciguerra, D.; Gelb, M. B.; Maynard, H. D. Synthesis and Application of Trehalose Materials. *J. Am. Chem. Soc.* **2022**, *2*, 1561–1587.

(253) McIlvaine, T. C. A BUFFER SOLUTION FOR COLORIMETRIC COMPARISON. *J. Biol. Chem.* **1921**, *49*, 183–186.

(254) Lisa Sophie Hönscheid. *Masterarbeit: Entwickelung und Analyse von pH-responsiven nanopartikulären Arzneistoffträgersystemen*; Münster, 2022.

(255) Wilson, D. S.; Dalmasso, G.; Wang, L.; Sitaraman, S. V.; Merlin, D.; Murthy, N. Orally delivered thioketal nanoparticles loaded with TNF-α-siRNA target inflammation and inhibit gene expression in the intestines. *Nat. Mater.* **2010**, *9*, 923–928.

(256) Zhou, J.; Liu, J.; Cheng, C. J.; Patel, T. R.; Weller, C. E.; Piepmeier, J. M.; Jiang, Z.; Saltzman, W. M. Biodegradable poly(amine-co-ester) terpolymers for targeted gene delivery. *Nat. Mater.* **2011**, *11*, 82–90.

(257) Lv, C.; Wang, Z.; Wang, P.; Tang, X. Photodegradable polyurethane self-assembled nanoparticles for photocontrollable release. *Langmuir* **2012**, *28*, 9387–9394.

(258) Reinhard, R.; Schmidt, B. F. Nitrobenzyl-Based Photosensitive Phosphoramide Mustards: Synthesis and Photochemical Properties of Potential Prodrugs for Cancer Therapy. *J. Org. Chem.* **1998**, *63*, 2434–2441.

(259) Santra, S.; Sk, M. A.; Mondal, A.; Molla, M. R. Self-Immolative Polyurethane-Based Nanoassemblies: Surface Charge Modulation at Tumor-Relevant pH and Redox-Responsive Guest Release. *Langmuir* **2020**, *36*, 8282–8289.

(260) Wei, P.; Cornel, E. J.; Du, J. Breaking the Corona Symmetry of Vesicles. *Macromolecules* **2021**, *54*, 7603–7611.

(261) Li, S.; Chen, G.; Zhou, Z.; Li, Q. Stimuli-induced multiple dissociation and micellization transitions of random copolymers. *RSC Adv.* **2015**, *5*, 65847–65855.

(262) Chunhachaichana, C.; Srichana, T. Efficiency of sildenafil encapsulation in poloxamer micelles. *J DISPER SCI TECHNOL* **2019**, *40*, 1461–1468.

(263) Cuong, N.-V.; Hsieh, M.-F.; Chen, Y.-T.; Liau, I. Synthesis and characterization of PEG–PCL–PEG triblock copolymers as carriers of doxorubicin for the treatment of breast cancer. *J. Appl. Polym. Sci.* **2010**, *117*, 3694–3703.

(264) Minò, A.; Cinelli, G.; Lopez, F.; Ambrosone, L. Optical Behavior of Nile Red in Organic and Aqueous Media Environments. *Appl. Sci.* **2023**, *13*, 638.

(265) Ray, A.; Das, S.; Chattopadhyay, N. Aggregation of Nile Red in Water: Prevention through Encapsulation in β-Cyclodextrin. *ACS omega* **2019**, *4*, 15–24.